Optimal Control Solutions for Islanded AC Microgrids

Faculty of Engineering and Science

Department of Energy Technology

Center for Research on Microgrids

MSc. in Electrical Power Systems and High Voltage

EPSH3-1035

May 28, 2021

Title:	Optimal Control Solutions for Islanded AC Microgrid
Semester:	9th - 10th
Project period:	01.09.2020 to 28.05.2021
ECTS:	50
Supervisor:	Josep M. Guerrero Juan C. Vasquez Najmeh Bazmohammadi Gibran David Agundis Tinajero
Project group:	EPSH3-1035
Group members:	Gowtham Meda Vanaprasad Sarthak Chopra

Total:	121 pages
Appendix:	37 pages
References:	4 pages

Synopsis

A microgrid is a localized, distribution level smart grid with the capability of disconnecting from the main grid and operating independently. Microgrids offer technical, environmental and economical benefits and have emerged as a prominent technology attempting to challenge the norms of the conventional power system. However, controlling the operation of the microgrid and its various components optimally is a challenge. A hierarchical control scheme may be used to address some of the challenges posed by microgrids. Such a scheme contains multiple levels of control operating on different time scales, which manage independent features of the control structure. This is the basis of the Extended Optimal Power Flow algorithm that is proposed and investigated in this thesis. The primary and secondary levels maintain the voltage magnitude and frequency at the buses, along with ensuring power balance in the system. The tertiary level supervises the entire operation and keeps check on the various system constraints, while optimizing a system level objective. Simulation results obtained from a 6-bus test system and a modified CIGRE benchmark microgrid system, approve the effectiveness of the proposed offline algorithm.

Summary

A microgrid is a local energy grid that has the control capability to disconnect from the main grid and operate autonomously. Typically, microgrids were powered by conventional diesel generators, but with recent developments in the field of renewable energy sources, complementary technologies such as energy storage devices, flexible loads, among others are required to effectively utilize the green energy to its maximum potential possible.

Microgrids offer various technical, economical and environmental benefits. However, a microgrid is associated with certain control challenges as system dynamics with different time scales are involved in its control operation which results in the need for a hierarchical control scheme. The various levels of the control operate in conjunction with each other to ensure the reliable operation of a microgrid.

In this thesis, the hierarchical control of an islanded AC microgrid with primary, secondary and tertiary level control is presented. The primary control provides local voltage and frequency support, the secondary control compensates the voltage and frequency deviations from the output of primary control and finally, in the tertiary control an energy management system is implemented for the economic and optimal operation of a microgrid. The primary control and secondary controls are incorporated in power flow formulation using MATLAB to ensure optimal power flow in the microgrid. To accommodate tertiary control level for a microgrid, an extended optimal power flow algorithm is proposed. The control algorithm is evaluated for a small test system and then verified on a modified medium voltage CIGRE benchmark system to optimize various system objectives and to ensure the system operates within its constraints and operating limits.

Preface

This thesis is written by the group EPSH3-1035 which constituted of two Master students at the Department of Energy Technology at Aalborg University (AAU). The research project focuses on exploring hierarchical control as a means of controlling and optimizing the operation of islanded AC microgrids.

The authors would like to thank Josep M. Guerrero and Juan C. Vasquez for providing the opportunity to conduct research in association with the Center for Research on Microgrids (CROM) at the Department of Energy Technology, AAU.

The authors would also like to express their gratitude towards the co-supervisors Najmeh Bazmohammadi and Gibran David Agundis Tinajero for their immense support and guidance throughout the project duration.

In this project MathWorks® MATLAB has been used to model and simulate the proposed algorithm and to plot the graphs. The thesis has been written using LaTeX.

Abbreviations

Abbreviation	Full Form
BESS	Battery Energy Storage System
CG	Conventional Generator
DER	Distributed Energy Resources
DG	Distributed Generation
DR	Demand Response
DSM	Demand Side Management
ED	Economic Dispatch
EMS	Energy Management System
EOPF	Extended Optimal Power Flow
ESS	Energy Storage Systems
EV	Electric Vehicles
HC	Hierarchical Control
HCPQ	Hierarchically Controlled PQ
MV	Medium Voltage
NR	Newton-Raphson
OPF	Optimal Power Flow
PCC	Point of Common Coupling
PLL	Phase-Locked Loop
PI	Proportional-Integral
PSO	Particle Swam Optimization
RES	Renewable Energy Sources
SOC	State of Charge
SPV	Solar Photo-Voltaic
SRF-PLL	Synchronous Reference Frame - Phase Locked loop
VOLL	Value of Loss of Load
WT	Wind Turbine

List of Figures

List of Tables

Table of Contents

1 Introduction

1.1 Background

In September 2020, the European Commission announced a new green agreement with an investment of 1 billion Euros, with the aim of accelerating towards the green and digital transition as a direct response to the on-going climate crisis [1, 2]. One of the focus areas of this comprehensive interdisciplinary policy is related to clean, affordable, and reliable energy. With the increase in Renewable Energy Sources (RES) penetration, complementary technologies such as Energy Storage Systems (ESS), controllable or flexible loads, Power-to-X technologies (P2X) are also essential to the energy sector, to effectively harness the green energy to its maximum potential possible [3].

Distributed Energy Resources (DER) are integrated with the grid in a decentralised manner, unlike conventional fossil fuel powered power plants. While this offers flexibility in integration, it raises some system stability and reliability challenges. These include new voltage and frequency control techniques to accommodate the power electronic interfaces, redesigning of protection schemes to allow bidirectional power flow, development of control strategies that would allow an easy integration of further technologies over time, among others [4]. Research and development of technologies to mitigate these shortcomings require challenging conventional power system norms. Flexibility or variability in the system can also be included from the demand-side through flexible loads and storage systems, and Demand Response (DR) programs [5].

While the concept of microgrids has been around for the past few decades, they were conventionally powered solely by fossil fuel. Microgrids have existed in regions where it was not technically or economically feasible to connect to the main grid [4]. A microgrid can operate in grid-connected mode or islanded mode, in case of faults or planned islanding for maintenance [4, 6]. In either case, there is a need to control the microgrid along with its various DER to maintain the voltage and frequency within their desired limits, regulate the power quality, determine load sharing between the generation units, etc., in order to manage the microgrid operation [6]. Since dynamics with different time scales are involved in microgrid control operation, and an individual control cannot manage multiple operational objectives, a Hierarchical Control (HC) scheme is a suitable approach [6, 7]. The various levels of a HC work in collaboration with each other to ensure acceptable operation of the microgrid [4]. Therefore, there also arises a need to design appropriate control schemes for the optimal control of microgrids.

1.2 Problem Formulation

A microgrid is a local grid at the distribution level with a group of loads and DER within a given electrical boundary that can be controlled as a single unit with respect to the main grid. A microgrid aims to form a flexible, reliable and self-sufficient system that has the control capability to disconnect from the main grid and operate autonomously [6]. A microgrid faces many challenges while operating in islanded mode such as power sharing among the Distributed Generation (DG) units, voltage and frequency stability issues, protection, reliability and performance of the system [8, 9]. The dynamics of these various issues operate with different time constants and therefore, a single control is incapable of managing all of them. A HC scheme comprises of multiple control levels, with each level managing different system dynamics. Hence, a HC scheme is chosen in this project.

The primary and secondary levels of HC restore the bus voltage magnitude and system frequency to their desirable values. The third level or tertiary control is the supervisory level [6]. This level has the function to optimise the microgrid operation, such as maximizing renewable energy utilization or minimizing the operational cost, among others. Hence, this level is also called as Energy Management System (EMS). The EMS has the responsibility of ensuring optimal and reliable operation of a system.

The aim of this thesis is to design a control algorithm for the optimal power flow in an islanded AC microgrid using HC in order to minimize the operations cost of the generation units, minimize RES curtailment, and also incorporating DR techniques in the system.

1.3 Objectives

1. To analyse the hierarchical control based power flow in an islanded AC microgrid.
2. To propose an optimization algorithm for integrating EMS with hierarchical control based power flow in an islanded AC microgrid.
3. To validate the proposed scheme on a modified MV CIGRE benchmark system by simulating different cases to minimize the operational cost from conventional generating units and,
    a) Minimizing RES curtailment.
    b) Inclusion of a DR technique.

1.4 Methodology

To fulfil the objectives of this thesis, the methodology is sequentially ordered as following,

1. Review of state of the art by understanding the importance of DER, DR and microgrid.
2. Development and implementation of a HC scheme for an islanded AC microgrid and formulation of hierarchically controlled power flow.

3. Evaluation of Economic Dispatch (ED) to achieve the objectives such as minimizing Conventional Generator (CG) units operating cost, minimize RES curtailment, and inclusion of DR technique while satisfying the system constraints.
4. Development of a control algorithm for EMS with the inclusion of hierarchical controlled power flow formulation.
5. Performing steady-state analysis on a modified MV CIGRE benchmark system using both conventional and hierarchical power flow formulation.
6. Validation of the proposed algorithm on a modified MV CIGRE benchmark system to minimize the CG units' operating cost in conjunction with different cases i.e.,
    a) Minimizing RES curtailment
    b) Inclusion of a DR technique

1.5 Limitations

The relevant limitations of this study are listed below,

1. An ideal Battery Energy Storage System (BESS) is considered in the proposed EMS algorithm for simplicity. The initial SOC is assumed to be 50%, although, the final SOC is not optimized to any value. The BESS contributes only in active power support.
2. The upper and lower bounds for the droop coefficients in chapter 3 and 5 are assumed for exemplification. In order to determine a realistic range for the coefficients, a stability analysis would be required, which is out of scope of this project.
3. Three Wind Turbines (WTs) of capacity 150 kW connected to bus 7 in modified CIGRE benchmark network have the same control variables for optimization and power generation. They are identical in all aspects.
4. Certain parameters such as power factor, active and reactive power limits, and penalty factors for RES curtailment and load shedding are assumed for exemplification in chapter 3 - 5.

1.6 Thesis Outline

This thesis is structured in the following manner:

Chapter 1: Introduction

In the first chapter, a basic background regarding the emergence of microgrids and motivation behind the research topic is briefly discussed. This chapter also includes the problem formulation, the main objectives of the thesis, the methodology employed and limitations concerning the research project.

Chapter 2: State of the art

This chapter describes the theory behind the main aspects of the study in this project. Initially, the relevance of DER and DR are discussed. Then, the idea behind microgrids is explored and the different levels in a HC schemes for AC microgrid are explained. Following that, power flow formulation for microgrids is presented and economic dispatch is elaborated upon.

Chapter 3: Extended Optimal Power Flow

In this chapter, for tertiary control level, an algorithm for the inclusion of power flow inside the optimization problem is proposed. The algorithm is tested on a 6 bus test system to achieve various optimization objectives.

Chapter 4: CIGRE Microgrid: Power Flow

In this chapter, the basic outline of the modified Medium Voltage (MV) CIGRE benchmark system is discussed. Later, the conventional power flow and hierarchically controlled power flow are implemented on the modified MV CIGRE microgrid.

Chapter 5: CIGRE Microgrid: EOPF

Based on the outcomes of chapter 4, the proposed control algorithm is implemented on the modified MV CIGRE benchmark system. Different cases are explored and the algorithm is validated.

Chapter 6: Conclusion and Future Works

In this final chapter, the findings from the other chapters are summarized. The results are discussed and the future works is stated.

2 | State of the Art

Centralized power generation provides the largest share of electricity in most of the industrialized countries. However, in the past couple of decades due to the increased environmental emissions and reduction in prices of RES installment, the energy sector worldwide has witnessed an increase in green energy. The intermittency of RES power and the use of power electronic interface in connecting DG units to the grid calls for the development of control techniques to maintain a stable and reliable system operation.

This chapter presents the significance of DER and their control in an AC microgrid. It also deliberates upon the concept of DR and lists out the features and challenges of microgrids. The different levels of hierarchical control for AC microgrid are also described. Later, the power flow problem formulation for microgrids is presented. Subsequently, a hierarchical based extended power flow formulation is explored to include primary and secondary microgrid control behaviour in the steady state solution. Lastly, an economic generation dispatch formulation to meet the load demand with minimum cost, satisfying system constraints such as generation limits, battery state-of-charge, etc., is elaborated with illustrative examples. All these concepts lead to a cumulative understanding of the need to employ hierarchical control for the optimal control of islanded AC microgrids.

2.1 Distributed Energy Resources

DER are local energy resources such as DG units, ESS, electric vehicles, heat pumps and electric charging stations, among others. Integration of DER provides an opportunity to meet the required load demand by shifting the electricity sector away from the centralized utility power generation. The inclusion of DER into the grid has several benefits which includes [8],

- Reduction in the overloading of transmission lines
- Control of the price variation due to intermittency in generation and demand
- Providing energy security and stability to the grid, thereby increasing the efficiency

Another important DER component is ESS which complements the integration of RES and also provides power to consumers during adverse conditions. ESS have a fast output response, which is able to give support to the grid and black start during power outages [8]. It also helps in mitigating grid congestions and provides voltage stability.

DER, however, increase the level of uncertainty and variability in the operation of the distribution network. Therefore, there is a need for proper coordination of these resources in real-time. The interconnection of DER imposes certain challenges such as overloading the existing feeders when the DG units and energy storage are not properly managed. Moreover, during the off-peak condition, a high penetration of RES may cause a reversal of power flow. This may also result in malfunctioning of protective equipment and voltage stability issues along the feeders [8, 9].

To perform proper control and coordination of the various DER, the microgrid plays an important role. A microgrid increases the reliability and flexibility in the DGs' operation. One of the main microgrid characteristics is that it can operate either autonomously or grid connected, for the exchange of power and supply of ancillary services [10].

2.2 Demand Response

Demand Side Management (DSM) is a technique that allows the customers to shift their demand during peak hours, by modifying their energy consumption pattern and load shape [5]. It is applicable in various parts of electric loads, preferably industrial loads [5], but also finds applications in commercial and household sectors. DSM is categorized into two main types: Demand Response (DR), and energy efficiency and conservation programs [11, 12]. The energy efficiency programs enables the customers to use less energy by receiving same level of end service. The energy conservation program encourage customers to give up some energy consumption to obtain favourable energy prices. These programs can be implemented by using the equipment through automated control or, replacing the old devices with a more energy efficient one [11, 12].

DR program is a major technology for solving the increase in power demand without further increasing the generation. DR changes the load shape of customers demand from their general consumption pattern in response to the change in electricity prices. It consists of different load shaping techniques such as peak clipping, valley filling, load shifting, strategic load growth and strategic conservation [5]. Peak clipping and valley filling reduce the load difference between peak and off-peak demand levels. Both these techniques involve direct load control to level the load profile. The valley filling allows the end-users to consume more power when electricity prices are cheap. Load shifting moves the load from peak hours to off-peak hours which could be achieved with the help of ESS to maintain the balance between generation and demand. Strategic load conservation decreases the overall demand by utilizing energy more efficiently whereas strategic load growth increases the overall demand to improve consumers productivity and electricity usage.

DR programs are classified as price-based and incentive-based programs [5]. Price-based programs consist of real-time pricing, critical peak demand pricing and time of usage pricing. Incentive-based programs consist of direct load control and energy market participation. DR programs benefit both consumer and utility in terms of reliability and economic aspects. Implementation of DR in microgrid prevents the supply-demand mismatch caused by intermittent nature of RES. It also increases the flexibility and reliability of the system by allowing the customers to make more informed decisions about their energy consumption. Among various DR methods, one commonly used DR technique is load shedding. Load shedding is performed at instances when the total load exceeds the generation limits and the system is not able to supply the demand. It is one of the simplest methods of achieving DR management. Hence, the load shedding method is employed in this study.

2.3 Microgrid

In [4], a microgrid is defined as a collection of generation units, loads and ESS. These operate in collaboration and coordination with each other to ensure a reliable supply of electric power, while being connected to the power system at the distribution level though a Point of Common Coupling (PCC). A schematic representation of a microgrid is illustrated in Figure 2.1.

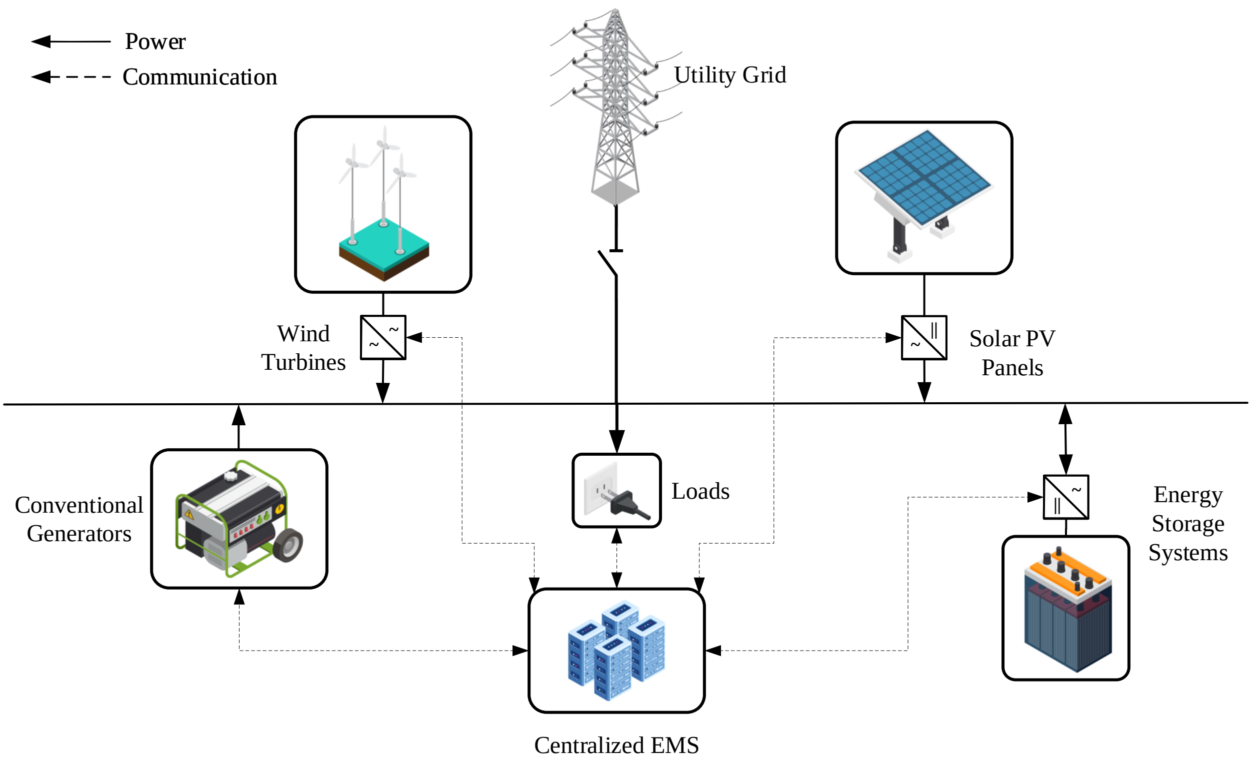

Figure 2.1: A schematic representation of a microgrid and the various systems it interacts with.

A microgrid essentially has four types of physical components, [6]

1. DER, which include RES, DG units and ESS

2. Power electronic interface between the DER and microgrid
3. Grid components such as transformers, protection equipment and lines
4. Loads or consumers

A microgrid should be capable of operating in two modes i.e., being connected to the main grid though the PCC and in isolation from the grid, i.e., islanded mode. The islanding of a microgrid may be intentionally scheduled for reasons such as maintenance or security, or it may be unintended due to faults or other unknown reasons [4].

Microgrids offer environmental, economical and technical advantages [7]. The use of RES results in a lower carbon footprint and other emissions from fossil fuels. The decrease in emissions and losses reduce the various costs involved. On the other hand, the technical benefits include providing power to isolated regions and reducing the possibilities of blackouts.
However, microgrids come with a set of control and protection challenges too, some of which are discussed in the following [4].

- Bidirectional power flow: Distribution feeders and protection equipment have been initially designed for unidirectional power flow.
- Low Inertia: The power electronic interface do not contribute to the system inertia as opposed to conventional synchronous generators.
- Stability: Oscillations and transients may occur in the microgrid, especially in situations such as transitioning between grid-connected and islanded modes.

In order to tackle these challenges and ensure a reliable supply of electricity, microgrids require a comprehensive control scheme. In [7], the IEC/ISO 62264 international standard for Microgrids and Virtual Power Plants is proposed to deal with hierarchical control, ESS and the market participation. Since different system dynamics operate in different time durations, a HC scheme is desirable in the control of microgrids [4].

2.4 Hierarchical Control

Hierarchical control of AC microgrid is essential to maintain voltage and frequency stability in the system. The HC of AC microgrid is divided into three levels: primary, secondary and tertiary control. The operation targets are specified to each control levels at a different time frame [13]. The main objective of primary control is local voltage and frequency support, and power-sharing capabilities. The secondary control restores the voltage and frequency deviations resulted from the action of the primary control. Finally, in the tertiary control, for optimal and economical operation of the microgrid, an EMS is employed. The subsequent sections give a brief description of each level.

2.4.1 Primary control

Primary control gives the first response to any change in the system condition. The main function of this control is to provide the local power by controlling the measured current injected from the DGs and measured voltage from the inverter output [4]. This results in current and voltage controlled schemes.

The grid following inverters are current-controlled sources that control the power output by measuring the grid voltage angle using the Phase-Locked Loop (PLL). They merely follow the grid angle or the grid frequency. So they need to operate in grid connected mode or with a DG unit that regulates the voltage and frequency of the microgrid. On the other hand, grid forming inverters are voltage-controlled sources that control the voltage and frequency output of the microgrid, hence they can be operated in islanded mode. The grid forming sources reduce the dependency of frequency dynamics of mechanical inertia in the system which in turn helps in stabilizing the grid. Droop control is commonly used in a grid forming inverters to obtain the frequency and voltage commands from the measured active and reactive power from the DG unit, to regulate the output voltage and frequency [14].

Grid Forming Droop-Based Control

The grid forming inverters are the controllers that work as ideal voltage source with a reference voltage and frequency. In islanded condition, the droop control method is often employed to adjust the voltage and frequency of the system, such that at least one DG unit is responsible for this adjustment. Frequency is the key indicator of equilibrium in the system. The power injection for each DG units in the microgrid is given by frequency ω in relation with active power P, and voltage V with reactive power Q as shown in (2.1) and (2.1) [15, 16].

$$\omega = \omega^* - K_n^p \; P_n \tag{2.1}$$

$$V_n = V_n^* - K_n^q \; Q_n \tag{2.2}$$

where ω^* is the reference angular frequency of the system, V_n^* is the reference voltage amplitude and K_n^p and K_n^q are droop coefficients. The angular frequency ω of the microgrid and the voltage V_n of each DG unit are given by their droop characteristics shown in Figure 2.2.

The grid forming primary controller for a DG is illustrated in Figure 2.3. The input references to the controller are voltage V^* and the frequency ω^* of the required voltage to be formed by the inverter at the PCC. These references are used to calculate the droop characteristics of the DG. The inner voltage and current loops regulate the control signal sent to the AC voltage source [15].

(a) Active Power- Frequency

(b) Reactive Power-Voltage

Figure 2.2: Droop characteristics.

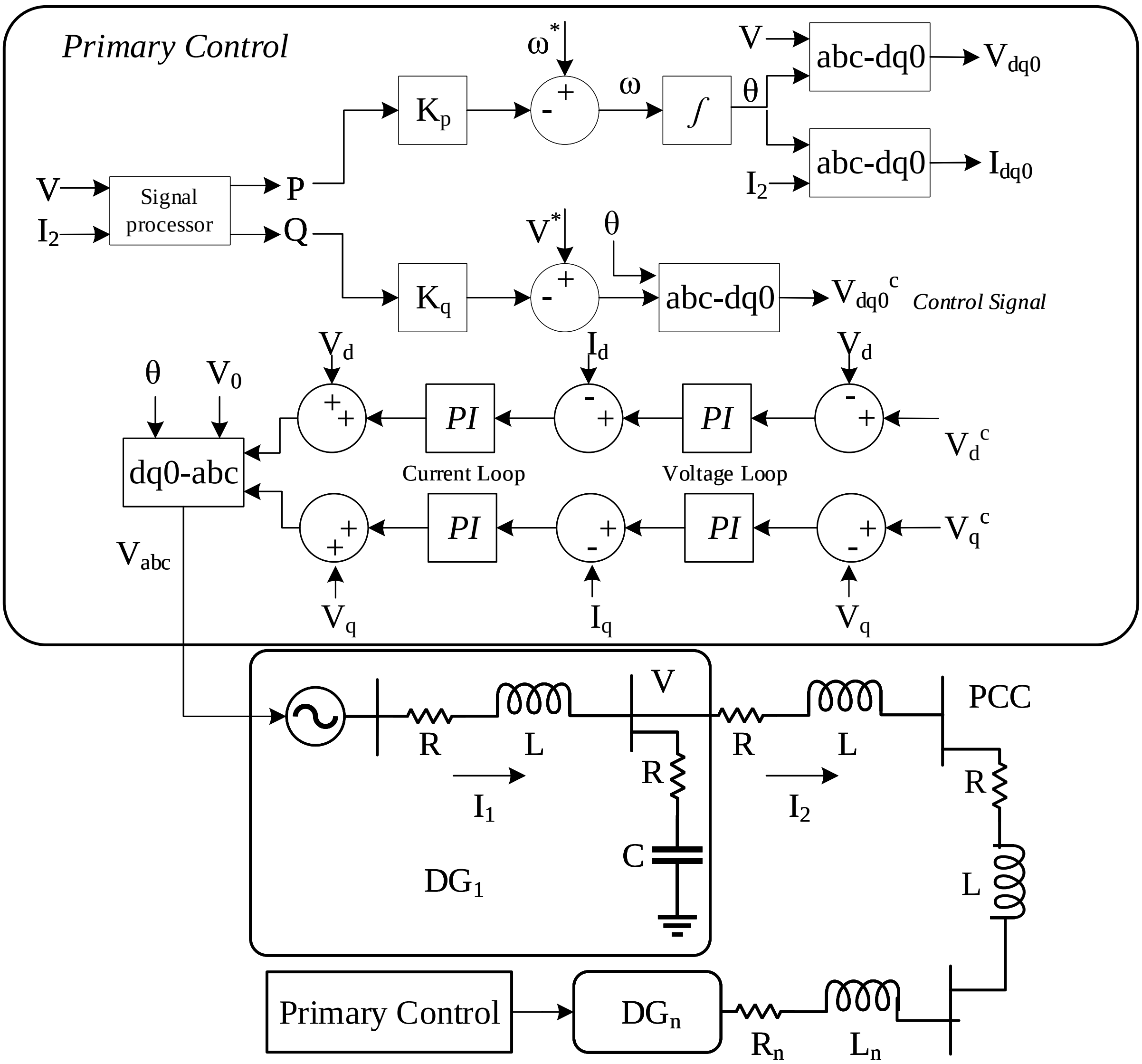

Figure 2.3: Grid forming controller with primary control [15].

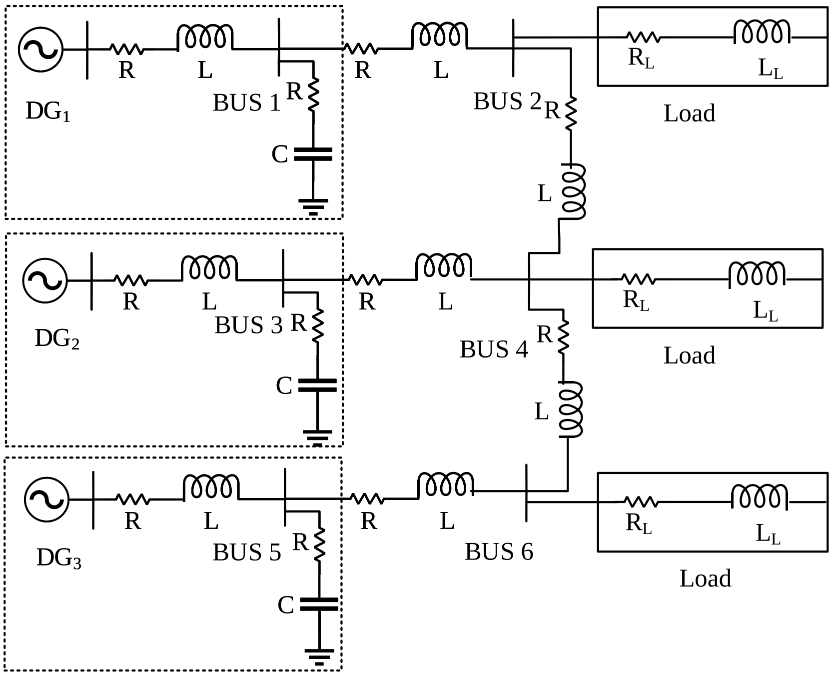

Figure 2.4: Single line diagram of test system.

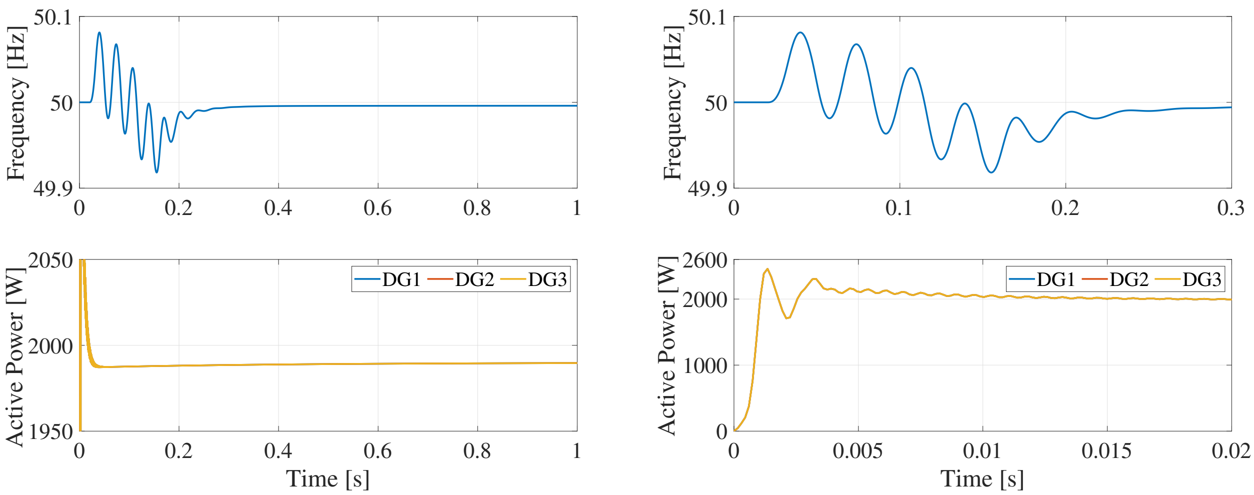

(a) Steady-state **(b)** Transient-state

Figure 2.5: Active power share of DGs and system frequency with primary controller.

The control is implemented on a 6-bus system with three DG units given in Figure 2.4. The various parameters of the system are given in Table 2.1. The active power injected by the DGs and the system frequency are shown in the Figure 2.5. The reactive power share of all DGs and voltage at load buses is shown in Figure 2.6. It is observed that due to the same droop gain coefficients of all the DG units, the active power and reactive power supplied by all the DG units is approx. 1989.5 W and 512 Var. The controlled DG units maintain stable steady-state condition for the given connected load. However, there is a steady-state error in the frequency and voltage. This error can be mitigated with the help

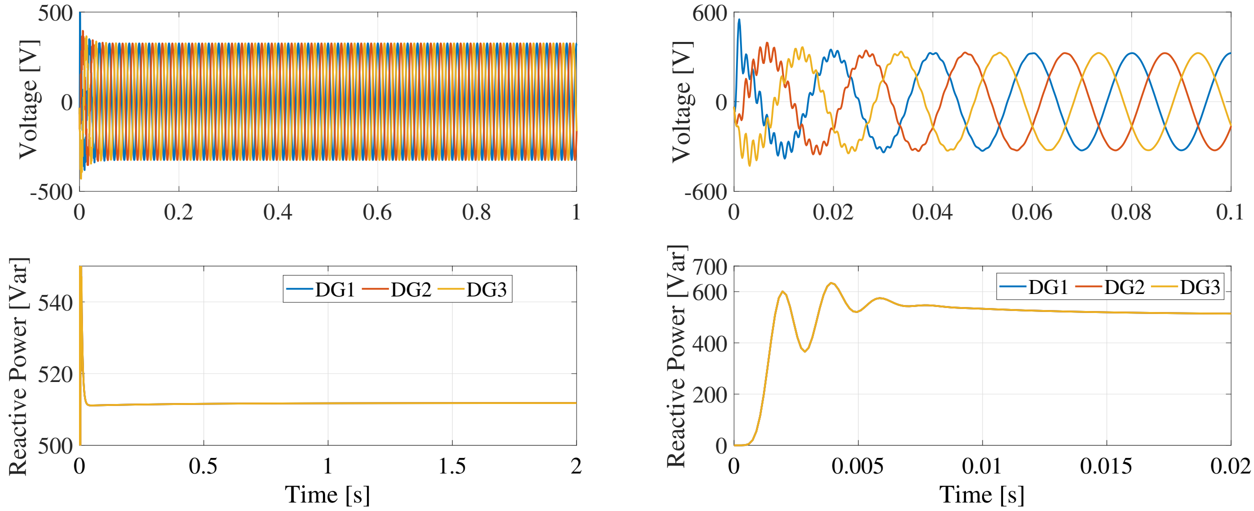

(a) Steady-state **(b)** Transient-state

Figure 2.6: Reactive power share of DGs and voltage at load buses with primary controller.

of secondary control.

Table 2.1: Parameters for hierarchical control of the given test system.

Parameter	**Symbol**	**Value**	**Unit**
Nominal Voltage	V_{l-l}^{rms}	400	V
Nominal frequency	f^*	50	Hz
Filter Resistance	R	0.1	Ohm
Filter Inductance	L	0.0018	H
Filter Capacitance	C	27×10^{-6}	F
Load Resistance	R_L	75.2941	Ohm
Load Inductance	L_L	5.9917×10^{-2}	H
Current loop proportional gain	K_{pc}	20	-
Current loop integral gain	K_{ic}	40	-
Voltage loop proportional gain	K_{pvo}	2.4×10^{-2}	-
Voltage loop integral gain	K_{ivo}	4.5	-
Freq. residual proportional gain	K^{pw}	0.02	-
Freq. residual integral gain	K^{iw}	4	-
Voltage residual proportional gain	K^{pv}	0.2	-
Voltage residual integral gain	K^{iv}	4	-
Droop coefficient	K_n^P	1.25×10^{-5}	-
Droop coefficient	K_n^Q	1×10^{-4}	-

2.4.2 Secondary control

The secondary control involves in restoring voltage amplitude and frequency deviations in the system. It measures the frequency and voltage in the microgrid at PCC bus and compares with the references ω^* and $|V^{**}|$ as shown in Figure 2.7. The error is given to a Proportional-Integral (PI) controller to obtain the output signals U_w^r and U_v^r as shown in (2.3) and (2.4) [17].

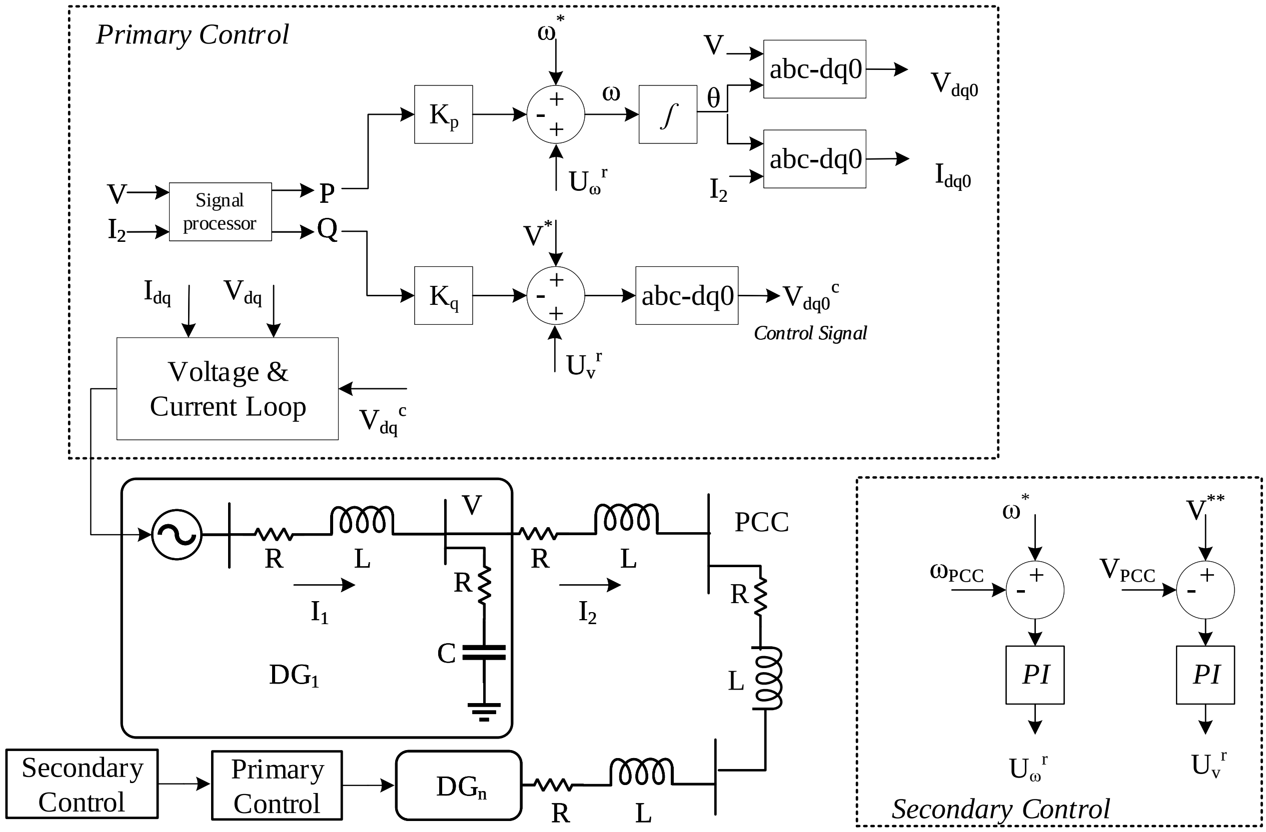

Figure 2.7: Hierarchical control with primary and secondary control.

$$U_w^r = K^{pw}(\omega^* - \omega_m) + K^{iw} \int (\omega^* - \omega_m)\ dt \tag{2.3}$$

$$U_v^r = K^{pv}(|V^{**}| - |V_m|) + K^{iv} \int (|V^{**}| - |V_m|)\ dt \tag{2.4}$$

The gain constants for PI controller are given in the Table 2.1. $|V_m|$ and ω_m are the voltage magnitude and frequency at m^{th} bus (PCC bus). It is noted that Synchronous Reference Frame - Phase Locked loop (SRF-PLL) measurement is used for secondary frequency control to bring back the system frequency to the nominal value. The output signals U_w^r and U_v^r of PI controllers are sent to primary control in order to restore the frequency and voltage magnitude. Incorporating these modifications, the droop equations (2.1) and (2.2) now become,

$$\omega = \omega^* - K_n^p.P_n + U_w^r \tag{2.5}$$

$$V_n = V_n^* - K_n^q.Q_n + U_v^r \tag{2.6}$$

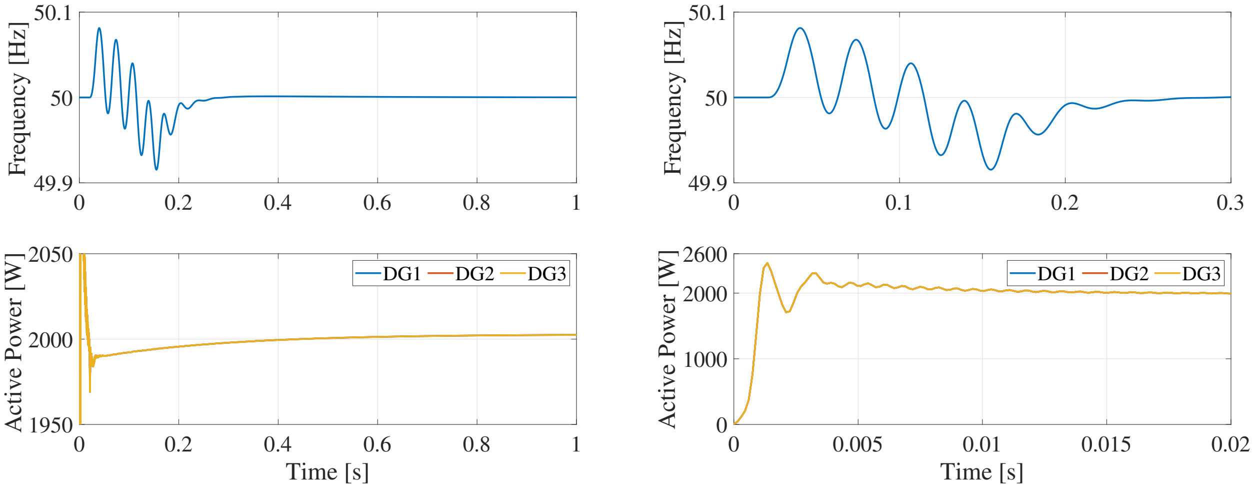

(a) Steady-state **(b)** Transient-state

Figure 2.8: Active power share of DGs and system frequency with primary and secondary controller.

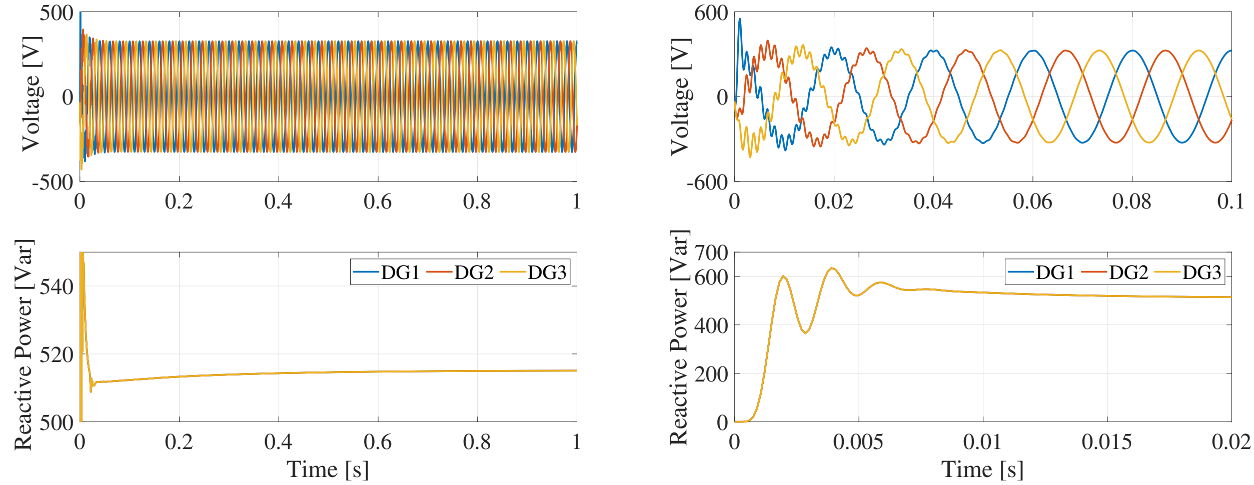

(a) Steady-state **(b)** Transient-state

Figure 2.9: Reactive power share of DGs and voltage at load buses with primary and secondary controller.

This secondary control is implemented in the test system to compare the results with primary control. From Figure 2.8 and Figure 2.9 it is observed that there is a slight increase in active power and reactive power supplied by all the DG units to 2003 W and 515 VAR respectively, as the voltage magnitude and system frequency are restored to their nominal values with the incorporation of secondary control. The entire simulink model is illustrated in Figure A.1-A.7 in Appendix A.

2.4.3 Tertiary control

The tertiary level of control adds intelligence to the system in order to optimize the operations of interest relating to efficiency and economics. It is also known by various other names such as Energy Management System, Supervisory Control And Data Acquisition, Microgrid Central Controller and

Microgrid Supervisory Controller [6]. While some papers place EMS into the secondary level and define tertiary control for multiple microgrid coordination, EMS can also be placed at the tertiary level [6].

EMS can be operated in two control modes: centralized and decentralized [6, 18]. Centralized control can be used to observe the entire system and is easier to implement. It can be used to optimize the exchange of power between the microgrid and the grid, or between microgrids. However, the controller would need to be quite powerful to handle the computational burden and data of the entire system. Moreover, in case of a fault in the central control unit, the entire system is susceptible to failure. Decentralized control addresses these shortcomings, however it has drawbacks of its own. Although it offers more flexibility in operation and avoids a single point of failure, a decentralized control scheme requires high level of coordination and synchronization between the units along with a communication system. Moreover, it may also compromise security of the system. Thus, depending on the size and purpose of the microgrid, a suitable scheme is used [6, 18]. However, irrespective of the type of control, the main duty of an EMS is to ensure reliable system operation.

An EMS involves one or more decision making algorithms, trying to optimize objectives of interest under various constraints [19]. The tertiary control operates in the order of several minutes, hence its output is considered as constant for power flow modelling, which operates in the order of few seconds [4]. An extensive survey of different optimization objectives, algorithms, and constraints have been discussed in [18, 19]. Some of these objectives include minimizing CO_2 emissions, maximize RES share, maximize profits etc. subject to constraints such as ESS storage capacity, generation limits, voltage at buses, system frequency, among others.

2.5 Newton Raphson Power Flow

The Newton-Raphson (NR) method is a well-known iterative algorithm for root-finding. Since power flow is a non-linear algebraic problem, it can be solved using the NR method [20, 21]. The general equation for NR method for a function $F(x)$ with jacobian J and change in variable Δx, and the update equation for the k^{th} iteration are given in (2.7) and (2.8) respectively.

$$F(x)^k = -J^k \Delta x^k \tag{2.7}$$

$$x_{k+1} = x_k + \Delta x^k \tag{2.8}$$

The NR method aims to minimize the power mismatch equations in vector $F(x)$ given in (2.9) in order to estimate the change in the system variables Δx i.e., the bus voltage magnitudes $|V_n|$ and angles δ_n.

$$F(x) = \begin{bmatrix} \Delta P_n = P_n^{(scheduled)} - P_n^{(calculated)} \\ \Delta Q_n = Q_n^{(scheduled)} - Q_n^{(calculated)} \end{bmatrix} \tag{2.9}$$

where the scheduled power is the difference between total generation and total load at that bus, and calculated powers are given by [20, 21],

$$P_n^{(calculated)} = \sum_{i=1}^{N} |V_n||V_i||Y_{ni}|cos(\theta_{ni} + \delta_i - \delta_n) \qquad for\ n = 1,\ \ldots,\ N \tag{2.10}$$

$$Q_n^{(calculated)} = -\sum_{i=1}^{N} |V_n||V_i||Y_{ni}|sin(\theta_{ni} + \delta_i - \delta_n) \qquad for\ i = n,\ \ldots,\ N \tag{2.11}$$

Conventionally, NR power flow is solved by reducing the partial differential equations in the Jacobian J to a set of algebraic equations [20, 21].

2.5.1 Power Flow in Microgrids

The conventional power flow problem is formulated by categorizing each bus into one of the following three types: Generator or PV Bus, Load or PQ Bus, and Slack Bus. However, for islanded microgrids a different approach for categorizing the buses is necessary.

2.5.1.1 Primary Control

The conventional power flow methodology cannot be used for microgrids due to the following reasons [22, 23]:

1. The frequency in an islanded AC microgrid is constantly varying and cannot be assumed to be fixed.
2. A slack bus cannot be defined since the DGs have limited capacities.
3. The sharing of active and reactive power among the DGs, and the local bus voltages, are not pre-specified and hence, the buses cannot be simply categorised as PQ or PV bus. Moreover, power sharing among the DGs depends on their droop characteristics.

Therefore, a new type bus categorisation is introduced, vis-a-vis Droop Bus [23, 24]. The Droop Bus is defined by the droop equations (2.1) and (2.2), which are used to calculate the scheduled active and reactive powers for a droop controlled DG. These scheduled power are as follows,

$$P_n^{(scheduled)} = \frac{\omega^* - \omega}{K_n^p} \tag{2.12}$$

$$Q_n^{(scheduled)} = \frac{V_n^* - V_n}{K_n^q} \tag{2.13}$$

Moreover, since the frequency of the microgrid is not constant, a relation for the system frequency is also required. This is achieved by fixing the voltage angle of one of the DGs as reference and adding its active power droop equation (2.1) to the formulation as separate relation [25]. This frequency relation is used to estimate the per unit frequency of the system. The final formulation of the power mismatch vector with Droop Buses is as follows,

$$\begin{bmatrix} \Delta P_n \\ \Delta Q_n \\ \Delta w \end{bmatrix} = \begin{bmatrix} P_n^{(scheduled)} - P_n^{(calculated)} \\ Q_n^{(scheduled)} - Q_n^{(calculated)} \\ (\omega^* - \omega) - (K_n^p P_n^{(calculated)}) \end{bmatrix} \tag{2.14}$$

The power flow can be solved numerically using the NR method. However, to simulate a more realistic power flow the effect of both primary and secondary controls are required.

2.5.1.2 Secondary Control

Droop controlled buses, i.e., the Droop Bus, does not represent a DG unit with secondary controls for voltage and frequency restoration. Therefore, a different formulation is required for the inclusion of secondary control [24].

Frequency Restoration

The active power P_n of a DG unit with secondary control is given by (2.5). In steady state, the system frequency ω is equal to the reference frequency ω^*. Thus, from (2.3) and (2.5), the scheduled active power for the *n-th* DG can be given by,

$$P_n^{(scheduled)} = \frac{U_w^{int}}{K_n^p} \tag{2.15}$$

where U_w^{int} is the integral part of U_n^r from (2.3) in steady state.
The bus phase angle δ_m where secondary control is required to regulate the voltage and frequency is given as follows,

$$\theta_m = \omega^* t + \delta_m \tag{2.16}$$

where θ_m is the reference frame angle and t is time. On differentiating (2.16),

$$\begin{aligned} \frac{d\theta_m}{dt} &= \omega_m = \omega^* + \frac{d\delta_m}{dt} \\ \text{or} \quad \frac{d\delta_m}{dt} &= \omega_m - \omega^* \end{aligned} \tag{2.17}$$

Substituting (2.17) in (2.3), the relation for U_w^{int} becomes as follows,

$$U_w^{int} = -K^{iw} \int \frac{d\delta_m}{dt}\, dt = -K^{iw}(\delta_m - \delta_m^0) \tag{2.18}$$

where δ_m^0 is the initial condition. Hence, the equation for scheduled active power (2.15) becomes [24],

$$P_n^{(scheduled)} = \frac{-K^{iw}(\delta_m - \delta_m^0)}{K_n^p} \tag{2.19}$$

Here, δ_m is the angle of the bus being controlled by secondary frequency control. The control sets the reference phase angle for all the DG units and thus, there is no need to fix a bus angle as reference, as was the case in primary control [25].

Voltage Restoration

The relation for scheduled reactive power for the *n-th* DG unit, based on (2.4) and (2.6) is as follows,

$$Q_n^{(scheduled)} = \frac{|V_n^*| - |V_n| + U_v^r}{K_n^q} \tag{2.20}$$

Since, in steady state, the voltage magnitude of the bus being controlled by secondary control will be 1 pu, i.e., $|V_n| = |V^{**}|$ therefore, $U_v^r = U_v^{int}$. Moreover, this also implies that the reactive power equation for this bus is not being used in the formulation since the result is already fixed, i.e., voltage is already known. Instead, this equation can be used to estimated U_v^{int}, which cannot be calculated in any other way, as was the case for U_w^{int} [24]. This way the reactive power equation for the bus being controlled is still used in the formulation. Thus, U_v^{int}, becomes one of the variable to estimate by NR iterations, along with the bus voltages and angles.

This new bus type based on (2.19) and (2.20) is called the Hierarchically Controlled PQ (HCPQ) Bus and includes the effects of both primary and secondary controls [24]. The power mismatch vector can hence be formulated as follows,

$$F(x) = \begin{bmatrix} \Delta P_n \\ \Delta Q_n \end{bmatrix} = \begin{bmatrix} P_n^{(scheduled)} - P_n^{(calculated)} \\ Q_n^{(scheduled)} - Q_n^{(calculated)} \end{bmatrix} \tag{2.21}$$

The 6-bus system studied in 2.4 with three DGs is simulated in MATLAB for two cases: i) with primary controlled Droop Bus and ii) with primary and secondary controlled HCPQ Bus. The results are compared in Table 2.2. Since the system is symmetrical and balanced, all DGs will generate the same output and the same voltage will be observed at all three loads.

As it can be seen from Table 2.2, with the inclusion of secondary control, the bus voltage magnitude and the system frequency are restored to their nominal values. Moreover the results from MATLAB simulation match with those from the Simulink simulation in 2.4. However, the NR power flow simulations do not consider operational constraints of the DG units, nor does it factor in any optimization objective.

Table 2.2: Comparison of MATLAB simulation for hierarchical power flow.

Parameter		Case i)	Case ii)
Bus Voltage Magnitude[p.u.]	DG	0.9999	1.0030
	Load	0.9968	1.0000
Bus Voltage Angle [degrees]	DG	0	0.274
	Load	-0.3859	-0.3586
Active Power [W]	DG	1990	2003
Reactive Power [VAR]	DG	512	515
System Frequency [Hz]		49.9960	50.0000

2.6 Economic Dispatch

The ever-varying electric load demand is required to be met by the power generating units in the network in order to maintain power balance in the system. However, CG units vary widely in their operational cost and capacity. Fossil-fired units with a low marginal cost are relatively inflexible and the generators that can follow the load tend to be more expensive. The generators are also subjected to fuel limitations and environmental regulations that restrict their availability. These characteristics of the CG units are undertaken by the economic optimization process called ED [26].

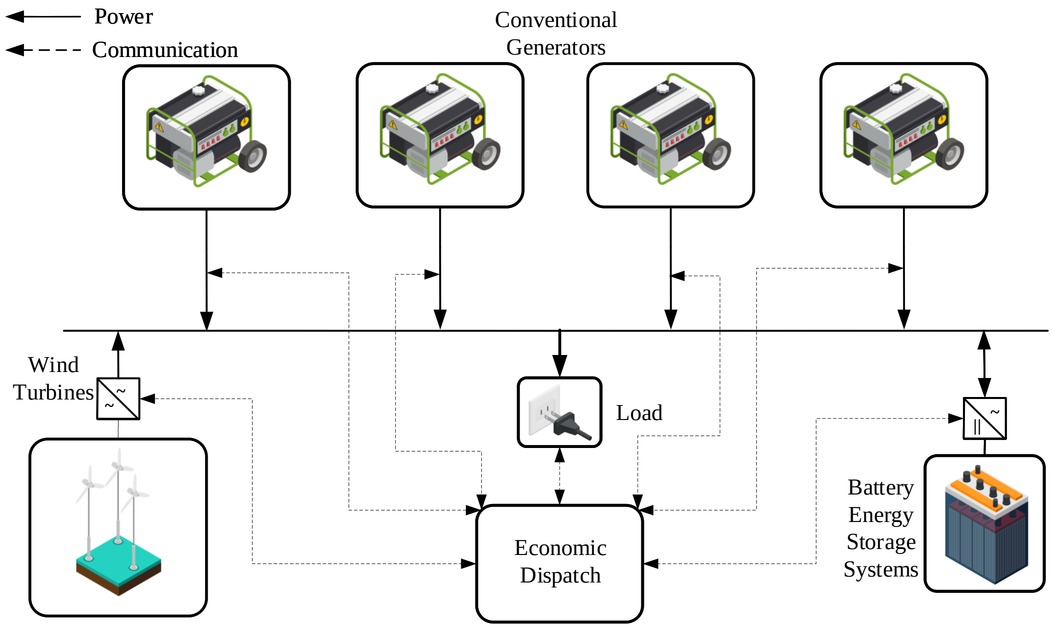

Figure 2.10: Schematic representation of the test system for ED.

ED aims to schedule the power outputs of the available generating units in such a way that operation cost of the generating units is minimized, while satisfying system constraints [26]. The other objectives of ED are as follows,

- Scheduling the committed generation units outputs to meet the required load while satisfying all units and system equality and inequality constraints with minimum operating cost.
- Minimizing the CO_2 emissions of CGs.
- Minimizing the losses in the system.
- Profit maximization by reducing the total cost.
- Maintaining system stability and security constraints.

In this section, the ED of active power generation is considered for a system with four CG units, one WT and a BESS. A schematic representation of the system is illustrated in Figure 2.10.

The cost function for ED is modelled as follows [27],

$$\begin{aligned}
&\min_{P_g} \sum_{t=1}^{T_H} \sum_{g=1}^{N_G} (a_g P_g^2(t) + b_g P_g(t) + c_g) \\
&\textit{subject to,} \sum_{g=1}^{N_G} P_g(t) - P_L(t) = 0 \\
&P_g^{min} - P_g(t) \leq 0 \\
&P_g(t) - P_g^{max} \leq 0
\end{aligned} \tag{2.22}$$

where T_H is the time horizon, N_G is the number of CGs, P_g is the power generated by DGs, P_g^{min} and P_g^{max} are the CG's operating limits, $P_L(t)$ is the load at time instant t, and a_g $[\$/kW^2]$, b_g $[\$/kW]$ and c_g $[\$]$ are the cost coefficients, given in Table 2.3.

However, there may be other objective functions which may need to be satisfied instead of operational cost, such as minimizing environmental impact or minimizing losses in the system. Moreover, in a practical power system multiple objectives may need to be optimized together, with different weights showing the priorities given to each objective function. The emission function for minimizing environmental impact is given as follows [27],

$$\begin{aligned}
&\min_{P_g} \sum_{t=1}^{T_H} \sum_{g=1}^{N_G} (d_g P_g^2(t) + e_g P_g(t) + f_g) \\
&\textit{subject to,} \sum_{g=1}^{N_G} P_g(t) - P_L(t) = 0 \\
&P_g^{min} - P_g(t) \leq 0 \\
&P_g(t) - P_g^{max} \leq 0
\end{aligned} \tag{2.23}$$

where d_g $[kg/kW^2]$, e_g $[kg/kW]$ and f_g $[kg]$ are the emission coefficients, given in Table 2.3. The multiobjective optimization problem for simultaneous minimization of operational cost and emission is given below in (2.24) with weights w_1 and w_2.

$$\begin{aligned}
&\min_{P_g} w_1 \sum_{t=1}^{T_H} \sum_{g=1}^{N_G} (a_g P_g^2(t) + b_g P_g(t) + c_g) \\
&+ w_2 \sum_{t=1}^{T_H} \sum_{g=1}^{N_G} (d_g P_g^2(t) + e_g P_g(t) + f_g) CG_{emission}
\end{aligned} \tag{2.24}$$

$$\textit{for weights, } w_1 \in [0,1] \textit{ and } w_2 = 1 - w_1$$

Table 2.3: List of coefficients and constraints for operational cost and emission functions [27].

g	a_g [$\$/MW^2$]	b_g [$\$/MW$]	c_g [\$]	d_g [kg/MW^2]	e_g [kg/MW]	f_g [kg]	P_g^{min} [MW]	P_g^{max} [MW]	RU_g [MW]	RD_g [MW]
1	0.12	14.8	89	1.2	-5	3	28	200	40	40
2	0.17	16.57	83	2.3	-4.24	6.09	20	290	30	30
3	0.15	15.55	100	1.1	-2.15	5.69	30	190	30	30
4	0.19	16.21	70	1.1	-3.99	6.2	20	260	50	50

The parameter $CG_{emission}$ is the environmental emission cost and is needed to convert the emission function (2.23) to the same units as the operational cost function (2.22). It's value is 0.1 $\$/kg$ [27]. The multiobjective function is solved in MATLAB using the *fmincon* function for one hour for a load value of 510 MW. The results are given in Table 2.4. As expected, the operational cost and emission values vary with the change in weights, with the maximum cost (and minimum emission) incurring at $w_1 = 0$ and the minimum cost (and maximum emission) at $w_1 = 1$.

Table 2.4: Comparison of results for different weights for multiobjective ED with operational cost and emission functions.

$\mathbf{w_1}$	$\mathbf{w_2}$	$\mathbf{P_1}$**[MW]**	$\mathbf{P_2}$**[MW]**	$\mathbf{P_3}$**[MW]**	$\mathbf{P_4}$**[MW]**	**Cost[\$]**	**Emission[kg]**
0	1	138.22	71.95	149.49	150.33	19160.37	82380.23
0.25	0.75	147.79	81.32	146.12	134.77	18732.37	82970.87
0.50	0.50	155.52	91.01	141.57	121.90	18469.25	84532.65
0.75	0.25	161.63	101.20	136.27	110.90	18325.88	86906.99
1	0	166.19	112.11	130.45	101.25	18280.38	90075.55

Ramp Rates

A practical CG unit would also have mechanical limitations and cannot suddenly increase or decrease generation output. Hence, constraints on ramping the generation up and down are necessary. On including the ramp-up rate RU_g and ramp-down rate RD_d, the optimization problem becomes,

$$
\begin{aligned}
&\min_{P_g} \sum_{t=1}^{T_H} \sum_{g=1}^{N_G} (a_g P_g^2(t) + b_g P_g(t) + c_g) \\
&\textit{subject to,} \sum_{g=1}^{N_G} P_g(t) - P_L(t) = 0 \\
&\qquad P_g^{min} - P_g(t) \leq 0 \\
&\qquad P_g(t) - P_g^{max} \leq 0 \\
&\qquad P_g(t+1) - P_g(t) - RU_g \leq 0 \\
&\qquad P_g(t) - P_g(t+1) - RD_g \leq 0
\end{aligned}
\tag{2.25}
$$

The objective function given in (2.25) was solved for a time horizon of 24 hours using the load data given in Table 2.5. The calculated operational cost was found to be \$ 647,964.46 and the corresponding emission at that operational cost was 3,592,886.72 kg.

Table 2.5: Load data [27] for operational cost optimization.

Time (t) **[hr]**	**Load** (P_L) **[MW]**	**Time** (t) **[hr]**	**Load** (P_L) **[MW]**
1	510	13	754
2	530	14	700
3	516	15	686
4	510	16	720
5	515	17	714
6	544	18	761
7	646	19	727
8	686	20	714
9	741	21	618
10	734	22	584
11	748	23	578
12	760	24	544

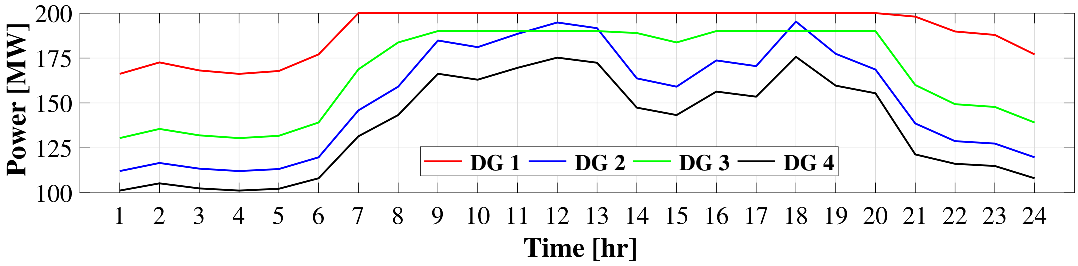

Figure 2.11: Active power generation of CGs for operational cost optimization.

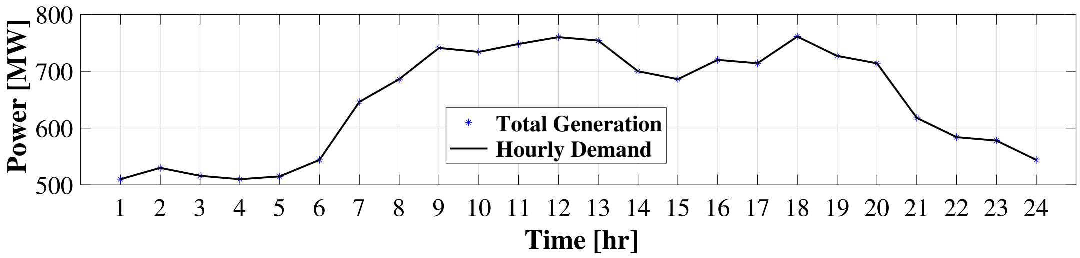

Figure 2.12: Power balance for operational cost optimization.

The active power generation of all four CGs for the optimized operational cost is displayed in Figure 2.11. It is observed that CG_1 contributes more than the other CGs. This is due to the fact that CG_1 is the cheapest to operate due to its cost coefficients. From Figure 2.12 it can be seen that power balance is obtained as the total generation is equal to the total load demand for every hour.

Storage System

A storage system is an essential component in a microgrid, as also briefly discussed in 2.1 and 2.3. In order to include a BESS in the system, the battery constraints are required to be included in the optimization formulation. These constraints are,

- BESS charging (P_c) and discharging (P_d) limits.
- The State of Charge (SOC) limits.
- Calculation of present SOC based on previous SOC and BESS parameters such as battery capacity (E), charging or discharging power and efficiency (η).
- Including the power charged or discharged by the BESS in the power balance equality constraint.
- The BESS should have a set amount of SOC (SOC_0) at the end of the time horizon for the next day.

Table 2.6: Parameters for BESS [27]

Parameter	**Value**	**Unit**
SOC_0	0.25	-
SOC^{min}	0.2	-
SOC^{max}	0.8	-
P_d^{min}	0	MW
P_d^{max}	60	MW
P_c^{min}	0	MW
P_c^{max}	60	MW
η_d	90	%
η_c	95	%
E	400	MWh

On incorporating these constraints, the optimization problem now becomes as follows,

$$
\begin{aligned}
\min_{P_g\ P_d\ P_c\ SOC} & \sum_{t=1}^{T_H}\sum_{g=1}^{N_G}(a_g P_g^2(t) + b_g P_g(t) + c_g) \\
\textit{subject to,} & \sum_{g=1}^{N_G} P_g(t) + P_d(t) - P_L(t) - P_c(t) = 0 \\
& SOC(t) - SOC(t+1) + \frac{1}{E}(\eta_c P_c - \frac{1}{\eta_d P_d})\Delta t = 0 \\
& SOC(T_H) - SOC_0 = 0 \\
& P_g^{min} - P_g(t) \leq 0 \\
& P_g(t) - P_g^{max} \leq 0 \\
& P_g(t+1) - P_g(t) - RU_g \leq 0 \\
& P_g(t) - P_g(t+1) - RD_g \leq 0 \\
& SOC^{min} - SOC(t) \leq 0 \\
& SOC(t) - SOC^{max} \leq 0 \\
& P_d^{min} - P_d(t) \leq 0 \\
& P_d(t) - P_d^{max} \leq 0 \\
& P_c^{min} - P_c(t) \leq 0 \\
& P_c(t) - P_c^{max} \leq 0
\end{aligned}
\tag{2.26}
$$

The BESS parameters are given in Table 2.6. On solving the updated operational cost function with BESS given in (2.26), the total operational cost was reduced to \$ 645497.74 and the total emission at this cost decreased to 3,558,071.32 kg. Figure 2.13, 2.14 and 2.15 illustrate the change in BESS SOC, BESS power, and the active power generation of the CGs respectively. As seen from Figure 2.16, power balance is maintained in the system.

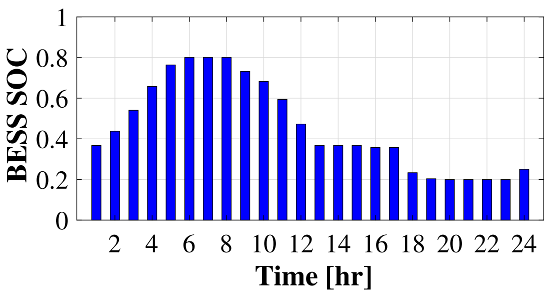

Figure 2.13: Normalized SOC of BESS.

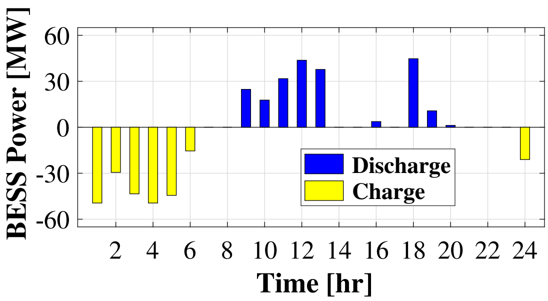

Figure 2.14: BESS power for 24 hours.

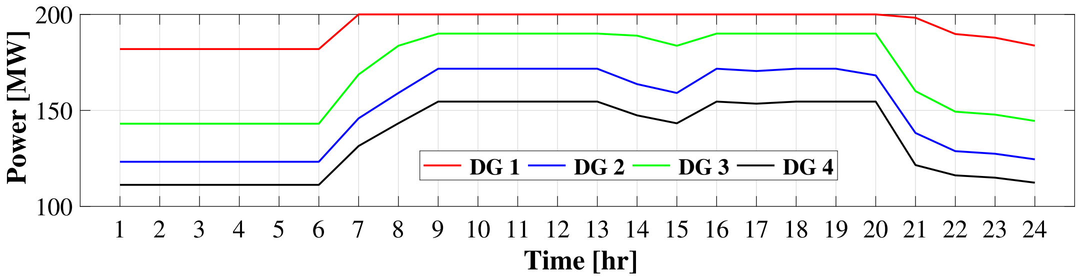

Figure 2.15: Active power generation of DGs for operational cost optimization with BESS.

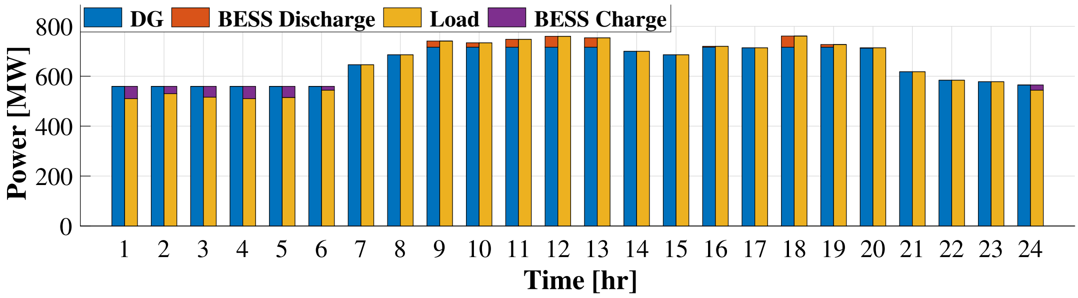

Figure 2.16: Active power balance for operational cost optimization with BESS.

RES generation curtailment

RES integration in microgrid is discussed in 2.3. Needless to say, the RES penetration should be maximized in order to have the least environmental footprint and fuel cost. Therefore, the inclusion of RES such as WT in the optimization problem should intend to minimize its curtailment. This is achieved by introducing a penalty factor CWT for the curtailed wind power P_{WTc}. The available wind power is given in Table 2.7.

Table 2.7: Available wind power data [27].

Time (t) [hr]	Available wind power (P_{WT}) [MW]	Time (t) [hr]	Available wind power (P_{WT}) [MW]
1	44.1	13	487.6
2	48.5	14	521.9
3	65.7	15	541.3
4	144.9	16	560
5	202.3	17	486.8
6	317.3	18	372.6
7	364.4	19	367.4
8	317.3	20	314.3
9	271	21	316.6
10	306.9	22	311.4
11	424.1	23	405.4
12	398	24	470.4

The optimization problem is thus modified as follows,

$$
\begin{aligned}
\min_{P_g \;\; P_d \;\; P_c \;\; SOC \;\; P_{WTc}} \; & \sum_{t=1}^{T_H}\sum_{g=1}^{N_G} (a_g P_g^2(t) + b_g P_g(t) + c_g) + \sum_{t=1}^{T_H}(P_{WTc}\; CWT) \\
\textit{subject to,} \; & \sum_{g=1}^{N_G} P_g(t) + P_d(t) + P_{WT}(t) - P_L(t) - P_c(t) - P_{WTc}(t) = 0 \\
& SOC(t) - SOC(t+1) + \frac{1}{E}(\eta_c P_c - \frac{1}{\eta_d P_d})\Delta t = 0 \\
& SOC(T_H) - SOC_0 = 0 \\
& P_g^{min} - P_g(t) \leq 0 \\
& P_g(t) - P_g^{max} \leq 0 \\
& P_g(t+1) - P_g(t) - RU_g \leq 0 \\
& P_g(t) - P_g(t+1) - RD_g \leq 0 \\
& SOC^{min} - SOC(t) \leq 0 \\
& SOC(t) - SOC^{max} \leq 0 \\
& P_d^{min} - P_d(t) \leq 0 \\
& P_d(t) - P_d^{max} \leq 0 \\
& P_c^{min} - P_c(t) \leq 0 \\
& P_c(t) - P_c^{max} \leq 0 \\
& P_{WTc} - P_{WT} \leq 0 \\
& -P_{WTc} \leq 0
\end{aligned}
\tag{2.27}
$$

where P_{WT} is the available power output of WT at time t, given in Table 2.7 and the penalty factor $CWT = 50$ $\$/MW$ [27]. On solving, the optimized operational cost was found to be \$ 226511.14 and the total emission at this cost was 891353.03 kg. The inclusion of WT reduces operational cost by 64.91 % and emission at those costs by 74.95 %, as compared to the case with only BESS. Clearly, the inclusion of WT complements the optimization objective of minimizing operational cost, along with reducing the environmental impact of the system.

From Figure 2.17 and 2.19 it can be inferred that the BESS and WT complement the optimization objective in minimizing operational cost by reducing the CG generation output. Figure 2.20 illustrates that there is no wind curtailment. As observed from Figure 2.21, power balance is maintained throughout the time horizon with the help of BESS and WT.

At $t = 24$ wind generation is high. Subsequently, the CGs are pushed down to their minimum operational limits in order to minimize cost. After meeting the load demand, the excess power should

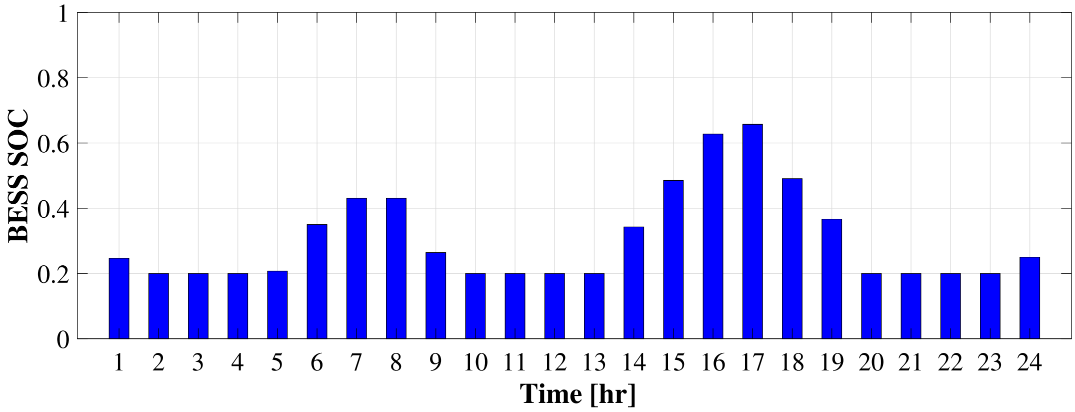

Figure 2.17: Normalized SOC with WT.

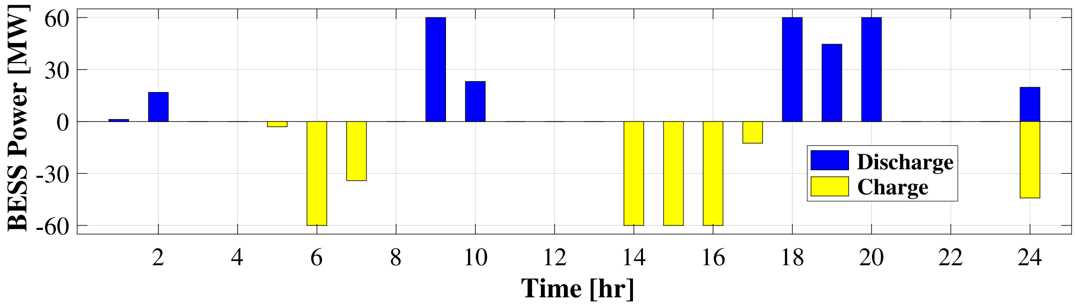

Figure 2.18: BESS power with WT.

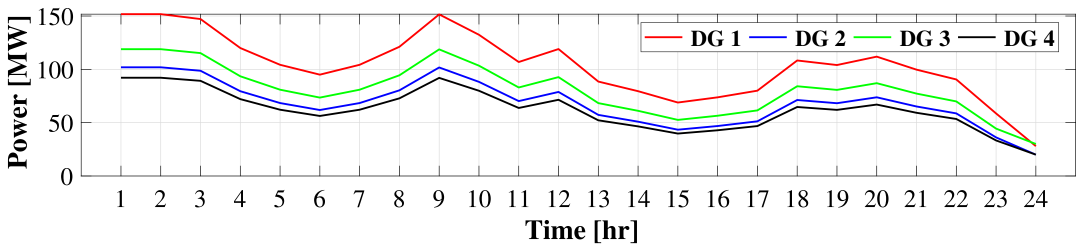

Figure 2.19: Active power generation of CGs for operational cost optimization with BESS and WT.

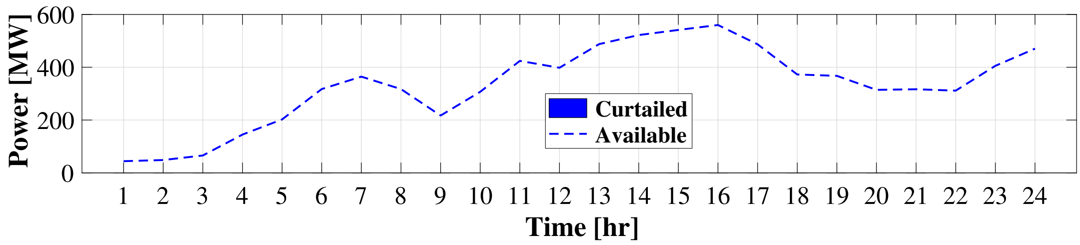

Figure 2.20: Available wind power and curtailment.

be used to charge the BESS. At this hour, the BESS needs to have exactly 25% SOC. However, from the Figure 2.18 it can be seen that both charging and discharging action of BESS take place at this hour. The optimization solver considers this as the mathematically feasible solution, even though this is not a practically feasible solution. A reason for this is that there is no explicit constraint that

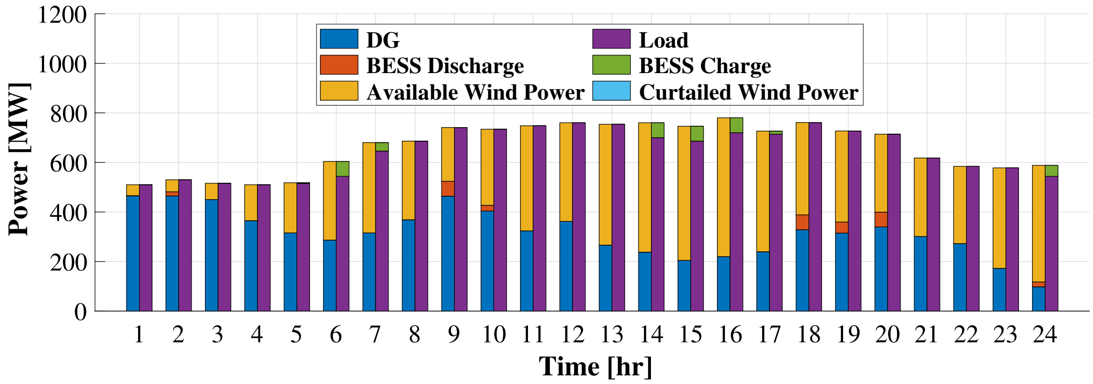

Figure 2.21: Active power balance for operational cost optimization with BESS and WT.

prevents both charging and discharging to occur simultaneously. To overcome this problem, the SOC constraint for $t = 24$ in the equation 2.27 is modified as follows,

$$SOC_0 - SOC(T_H) \leq 0 \tag{2.28}$$

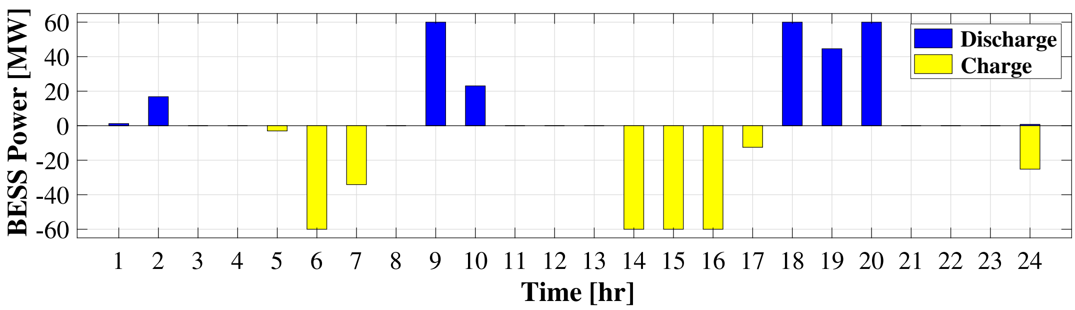

Figure 2.22: BESS power with WT ($SOC(T_H) \geq SOC_0$).

From Figure 2.22 it can be seen that although there is still an existence of the discharging power of BESS, its value is greatly reduced. To further verify this BESS behaviour, the load at $t = 24$ is varied and the results for that hour are shown in Table 2.8,

From Table 2.8 it can be inferred that the BESS has certain amount of discharging power, when there is no wind power curtailment and the power generated by the CGs reach to their minimum value. In order to resolve this anomaly, one of the following things may be done,

- Introduce a binary variable to signify when to charge or discharge. However this would convert the optimization problem into a Mixed Integer type problem. That would require a more advanced solver since the problem would become more complex.
- Both charging and discharging can be represented by a single variable. Moreover, the charging and discharging efficiencies are assumed to be 100%.

- Add a cost for BESS operation. This would prevent simultaneous charging and discharging action since both operations would add to the cost. This might, however, decrease the BESS usage.
- A non-linear constraint could be included which requires the product of the charging and discharging power to be zero at all hours.

Table 2.8: Results at t=24 with different load values.

$\mathbf{P_{g1}}$ [MW]	$\mathbf{P_{g2}}$ [MW]	$\mathbf{P_{g3}}$ [MW]	$\mathbf{P_{g4}}$ [MW]	$\mathbf{P_{d}}$ [MW]	$\mathbf{P_{c}}$ [MW]	**SOC**	$\mathbf{P_{WTc}}$ [MW]	**Load** [MW]
28	20	30	20	0.85	25.25	0.257	0	544
51.65	31.25	38.82	28.91	0	21.05	0.25	0	600
38.31	21.84	30	20.49	0	21.05	0.25	0	560
28	20	30	20	0.64	23.04	0.25	0	546
28	20	30	20	1.62	30.02	0.26	0	540
28	20	30	20	0	60	0.342	8.4	500

By employing the second procedure and assuming ideal behaviour of BESS, the SOC-Power relation given in (2.26) is modified as shown in (2.29), which is implemented in chapter 3. Note, that the BESS charging power is taken as negative and discharging power is taken as positive.

$$SOC(t+1) = SOC(t) + \frac{-P_{BESS}}{E}\Delta t \tag{2.29}$$

Load Shedding

Load shedding is discussed in 2.2. The implementation of load shedding in the optimization problem is performed to minimize the operational cost and emission from CGs, when the RES generation may not be sufficient to meet the required demand. This, however, is done by introducing a penalty factor for the shed load called Value of Loss of Load (VOLL) which is assumed to be 50 $\$/MW$. Thus, there is a trade-off between increasing the cost due to the load shedding penalty and decreasing the operational cost from CGs. The optimization problem is modified as follows,

$$
\begin{aligned}
\min_{P_g \ P_d \ P_c \ SOC \ P_{WTc} \ P_{LS}} \ & \sum_{t=1}^{T_H} \sum_{g=1}^{N_G} (a_g P_g^2(t) + b_g P_g(t) + c_g) + \sum_{t=1}^{T_H} (P_{WTc}\ CWT + P_{LS}\ VOLL) \\
subject\ to,\ & \sum_{g=1}^{N_G} P_g(t) + P_d(t) + P_{LS} + P_{WT}(t) - P_L(t) - P_c(t) - P_{WTc}(t) = 0 \\
& SOC(t) - SOC(t+1) + \frac{1}{E}(\eta_c P_c - \frac{1}{\eta_d P_d})\Delta t = 0 \\
& SOC(T_H) - SOC_0 = 0 \\
& P_g^{min} - P_g(t) \leq 0 \\
& P_g(t) - P_g^{max} \leq 0 \\
& P_g(t+1) - P_g(t) - RU_g \leq 0 \\
& P_g(t) - P_g(t+1) - RD_g \leq 0 \\
& SOC^{min} - SOC(t) \leq 0 \\
& SOC(t) - SOC^{max} \leq 0 \\
& P_d^{min} - P_d(t) \leq 0 \\
& P_d(t) - P_d^{max} \leq 0 \\
& P_c^{min} - P_c(t) \leq 0 \\
& P_c(t) - P_c^{max} \leq 0 \\
& P_{WTc} - P_{WT} \leq 0 \\
& - P_{WTc} \leq 0 \\
& P_{LS} - P_L \leq 0 \\
& - P_{LS} \leq 0
\end{aligned}
\tag{2.30}
$$

where P_{LS} is the total load shed at time t. On solving, the optimized operational cost was found to be \$ 226482.68 and the total emission at this cost was 878233.92 kg. The inclusion of WT and load shedding reduces the operational cost by 64.91 % and emission at those costs by 75.31 %, as compared to the case with only BESS. The addition of load shedding with WT and BESS further complements the optimization objective of minimizing operational cost, along with reducing the environmental impact of the system.

Figure 2.23, 2.24 and 2.25 shows the changes in BESS SOC, BESS power, and the active power generation of the CGs respectively. From the Figure 2.24 it can be seen that both charging and discharging action of BESS take place at t=24. This problem can be resolved by following one of the four possibilities as discussed in the previous section with ED with BESS and WT in 2.6.

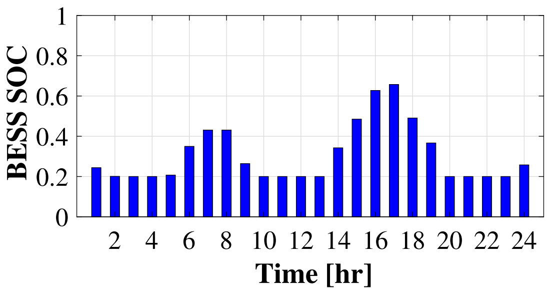

Figure 2.23: Normalized SOC with WT and load shedding.

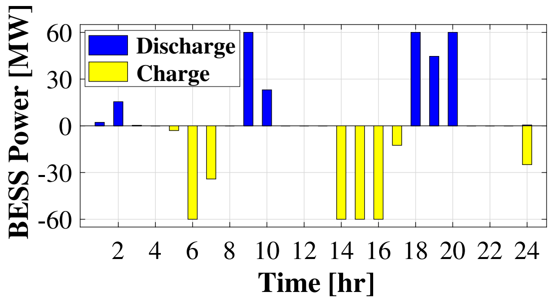

Figure 2.24: BESS power with WT and load shedding.

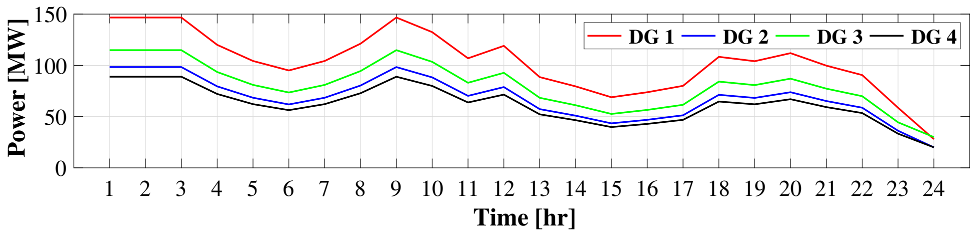

Figure 2.25: Active power of CGs for operational cost optimization with BESS, WT and load shedding.

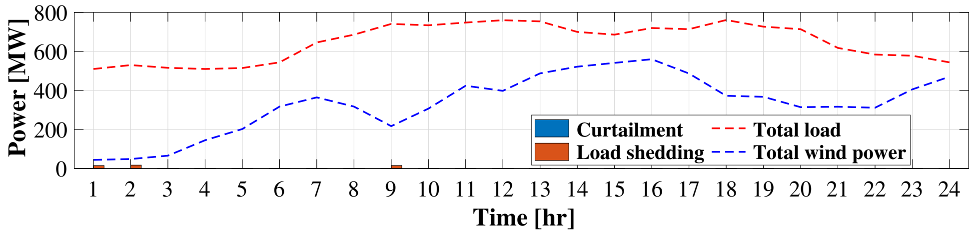

Figure 2.26: Load shedding and wind curtailment.

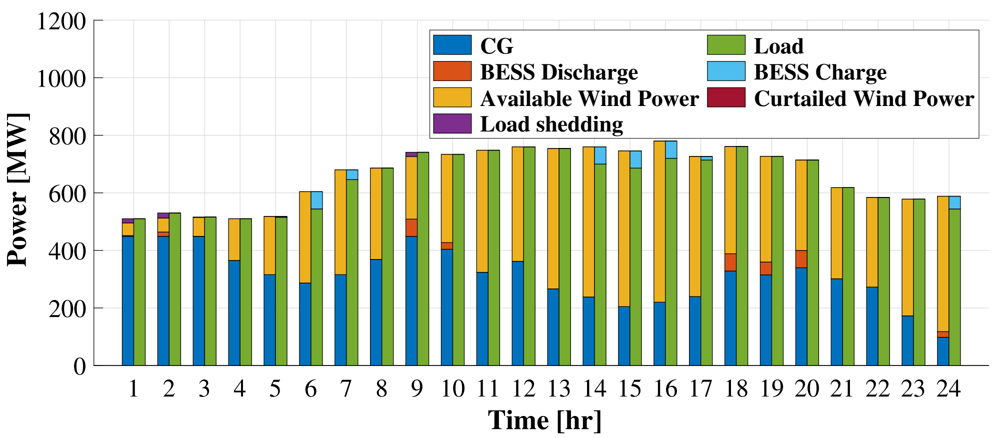

Figure 2.27: Active power balance for operational cost optimization with BESS, WT and load shedding.

From the Figure 2.26 it is observed that the load shedding takes place at the instances where difference in load and available RES power is high, in order to minimize the operating cost of CGs. As seen from Figure 2.27, power balance is maintained in the system with inclusion of load shedding.

2.7 Summary

This chapter describes the basic hierarchical control scheme of islanded AC microgrid that ensures safety, reliability and economic benefits. The primary and secondary controls are explained with schematic diagrams. The control behaviour is analyzed using a 6-bus test system. Additionally, steady-state analysis of islanded AC microgrid is solved numerically using the NR method. Moreover, to simulate a realistic microgrid power flow, the effect of primary and secondary control is considered. Thus, droop-based extended power flow and hierarchical extended power flow are performed. For each method, the power flow formulation is explained and the results for the modelled system are presented. The steady-state solution obtained from the power flow, however, does not consider ED i.e., as cost of operation of different CGs, operating limitations of CGs, losses, etc [20]. In a practical power system, these constraints are required to be included in the problem formulation while optimizing the power flow solution. To achieve this objective, the Extended Optimal Power Flow (EOPF) is introduced in Chapter 3.

3 Extended Optimal Power Flow

3.1 Introduction

A power system optimization problem that contains the power flow equations (2.10) and (2.11) may be classified as an Optimal Power Flow (OPF) problem [28]. The aim of OPF is to optimize a given objective by controlling the power flow, while making sure that the system components operate within their constraints and operating limits.

In islanded AC microgrids, the DGs also need to regulate the voltage and frequency in the system, apart from supplying power to meet the demand [29]. For this purpose, power flow-based hierarchical schemes have been proposed in literature, specifically droop-based methods. The inclusion of power flow inside the optimization automatically ensures power balance, rather than having a power balance constraint. A droop-based method for load sharing and voltage regulation is described in [30]. In [31], a HC power flow optimization is presented for loss minimization and ensuring frequency stability in the islanded microgrid. These hierarchical-based methods regulate the bus voltage and system frequency, and ensure power balance while optimizing a higher level objective.

A real-time centralized Extended Optimal Power Flow (EOPF) control is proposed in [32] which uses the droop bus formulation from 2.5.1.1 to optimize active and reactive power sharing (%) among the DGs in the microgrid, along with maintaining PCC voltage and maximizing the microgrid efficiency. The optimization is activated when a change in load or generation capacity is detected. The control dynamics of each participating DG is taken into account and thus, their droop coefficients are optimized. These optimized droop coefficients (K_n^p and K_n^q) define the dynamic and steady state operation of the DG units.

In droop bus formulation, each generation unit uses frequency instead of phase angle to control the active power flow since the initial phase angle values of other generation units are not known [33]. However, the initial frequency can be easily fixed as ω^* at no-load condition. This results in a trade-off between active power sharing and frequency accuracy in system [33]. Furthermore, the DGs are connected to the system through long feeders and are located far from the load. This may lead to voltage quality issues, reactive power flow, and power losses [32]. These problems can be resolved by HCPQ bus formulation. This technique represents DG units with secondary control for voltage and frequency restoration. Therefore, frequency and voltage restoration objectives need not be included in the EOPF formulation. It can be assumed that the microgrid frequency and reference bus voltages are regulated to 1 p.u. The inclusion of both primary and secondary controls inside the optimization would make the dynamics of the microgrid more realistic. This algorithm is explained in the subsequent section.

3.2 EOPF Algorithm with HCPQ Bus

An EMS is a tertiary level control that supervises the operation of a microgrid, as explained in 2.4.3. The controlling algorithm in the EMS has the function of optimizing the objectives of interest while maintaining optimal operating conditions in the system.

The primary level dynamics of a DG depend on its droop characteristics. Hence, in order to control the steady state performance of a DG , the droop characteristics of a DG need to be controlled [32], i.e., the droop coefficients need to be optimized. Furthermore, as elaborated in 2.5.1.2, the HCPQ bus formulation is able to restore the system frequency and bus voltages to well within the operational limits. Thus, if the HCPQ bus formulation regulates the system frequency and bus voltages, the droop characteristic can be controlled in order to achieve a higher level objective. In this way, an EOPF algorithm with HCPQ bus is proposed in Figure 3.1, which is inspired by the work in [32].

The algorithm works as follows,

1. A set of variables are initialized, which are to be optimized. These include the droop coefficients, along with other parameters depending upon the optimization objective and components in the system.
2. A steady state solution is found using the initialized variables by using HCPQ bus formulation.
3. The optimization problem is solved, subject to 0.
4. If an optimal solution is not reached, a new set of optimization variable are taken and the process is repeated from step 2.
5. If an optimal solution is achieved, the optimization process ends.

This algorithm is used in the following sections for different optimization objectives, using the 6-bus microgrid from Figure 2.4.

1. Equal power sharing (%) among the DGs.
2. Cost Minimization
3. Cost minimization, with the inclusion of an ideal BESS.
4. Cost minimization, with the inclusion of load shedding constraints.

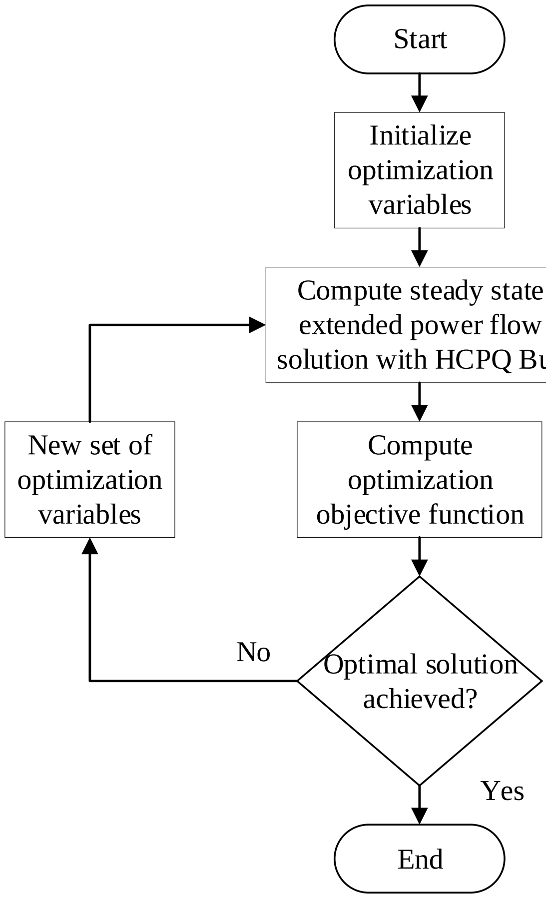

Figure 3.1: Proposed EOPF algorithm with HCPQ bus.

The simulations are performed on a computer with processor Intel (R) Core (TM) i5 - 8250U CPU @ 1.60 GHz, 1800 MHz with 8 GB RAM.

3.2.1 Power Sharing

In equal power sharing, each DG unit operates at the same percentage of its maximum capacity. Power sharing among DGs in a microgrid is important so as to share the load burden equally. In order to compute the optimal droop characteristics of each DG unit, the power sharing optimization problem is modelled as follows,

$$
\begin{aligned}
\min_{K_n^p\ K_n^q} \sum_{t=1}^{T_H}\sum_{g=1}^{N_G}\sum_{k=1}^{N_G} & \left(\frac{P_g(t)}{S_g^{max}(t)} - \frac{P_k(t)}{S_k^{max}(t)}\right)^2 + \left(\frac{Q_g(t)}{S_g^{max}(t)} - \frac{Q_k(t)}{S_k^{max}(t)}\right)^2 \\
\textit{subject to, } & K_n^{q\ min} - K_n^q \leq 0 \\
& K_n^q - K_n^{q\ max} \leq 0 \\
& K_n^{p\ min} - K_n^p \leq 0 \\
& K_n^p - K_n^{p\ max} \leq 0
\end{aligned}
\tag{3.1}
$$

The power sharing objective function is modelled as the sum of least squared errors between the active and reactive power share (%) of the different DG units. The active (P_g and P_k) and reactive (Q_g and Q_k) powers are calculated by the power flow equations of HCPQ bus described in 2.5.1.2. S_g^{max} is maximum apparent power capacity of the respective DG unit.

The optimization problem in (3.1) was simulated in MATLAB using *fmincon* function for t= 1 for the 6 bus test system in Figure 2.4 and the results are tabulated below in Table 3.1. As it can be seen, the DG units generate an equal share (%) of active and reactive powers, based on their capacities. The bus voltage magnitudes and angles are shown in Table 3.2. The simulation ran for 29 iterations and took 4.96 seconds, and the objective function (least squared error) was minimized to 3.05 $\times 10^{-8}$. The DG capacities are also given in Table 3.1. The limits for droop coefficients were as follows: $0.25 \times 10^{-5} \leq K_n^p \leq 6.25 \times 10^{-5}$ and $2 \times 10^{-7} \leq K_n^q \leq 5 \times 10^{-2}$. It is to be noted that these limits and capacities are arbitrary and do not represent any real system, they are only to test the simulation algorithm.

Table 3.1: Results for EOPF for active and reactive power sharing among DG units.

	$\mathbf{P_g}$ **[W]**	$\mathbf{P_g}$ **Share [%]**	$\mathbf{K_n}^\mathbf{p}$	$\mathbf{Q_g}$ **[VAR]**	$\mathbf{Q_g}$ **Share [%]**	$\mathbf{K_n}^\mathbf{q}$	$\mathbf{S_g}^\mathbf{max}$ **[VA]**
DG_1	2255.94	75.20	2.3939e-5	580.64	19.35	0.0189	3000
DG_2	2255.86	75.20	2.3940e-5	581.08	19.37	0.0109	3000
DG_3	1504.01	75.20	3.5907e-5	387.79	19.39	0.0305	2000

Table 3.2: Bus voltage and angle for EOPF power sharing.

Bus	**Voltage [p.u.]**	**Angle [degrees]**
1	1.0045	-0.1956
2	1.0011	-0.6392
3	1.0042	-0.2433
4	1.0007	-0.6772
5	1.0023	-0.4836
6	1.0000	-0.7736

3.2.2 Cost Minimization

In this, and the subsequent sections, the cost minimization EOPF problem is simulated for a time horizon of 24 hr for the same 6-bus system in Figure 2.4. First, a base case is performed in this section. The next two cases observe an addition of a BESS and load shedding constraints respectively. The optimization problem is modelled as shown in (3.2).

$$
\begin{aligned}
&\min_{K_n^p\ K_n^q} \sum_{t=1}^{T_H} \sum_{g=1}^{N_G} \left(a_g P_g^2(t) + b_g P_g(t) + c_g\right) \\
&\textit{subject to,}\ P_g^{min} - P_g(t) \leq 0 \qquad Q_g^{min} - Q_g(t) \leq 0 \\
&\qquad P_g(t) - P_g^{max} \leq 0 \qquad Q_g(t) - Q_g^{max} \leq 0 \\
&\qquad K_n^{q\ min} - K_n^q \leq 0 \qquad K_n^{p\ min} - K_n^p \leq 0 \\
&\qquad K_n^q - K_n^{q\ max} \leq 0 \qquad K_n^p - K_n^{p\ max} \leq 0
\end{aligned}
\tag{3.2}
$$

The cost coefficients are taken from Table 2.3, from the first three DGs. The active and reactive power limits are given in Table 3.3. The droop limits were taken as 2.5×10^{-6} to 6.25×10^{-5} for K_n^p, and 2×10^{-5} to 5×10^{-4} for K_n^q. It is to be noted that these power and droop limits are representational and for exemplification only. An arbitrary load profile was chosen, which is given in Figure 3.2. In this profile, 1 p.u. corresponds to a RL load of 75.2941 Ω and 5.9917×10^{-2} H, which is taken from Table 2.1. In terms of power, 1 p.u. corresponds to 2003 W and 515 VAR, according to the results in Figure 2.8 and 2.9.

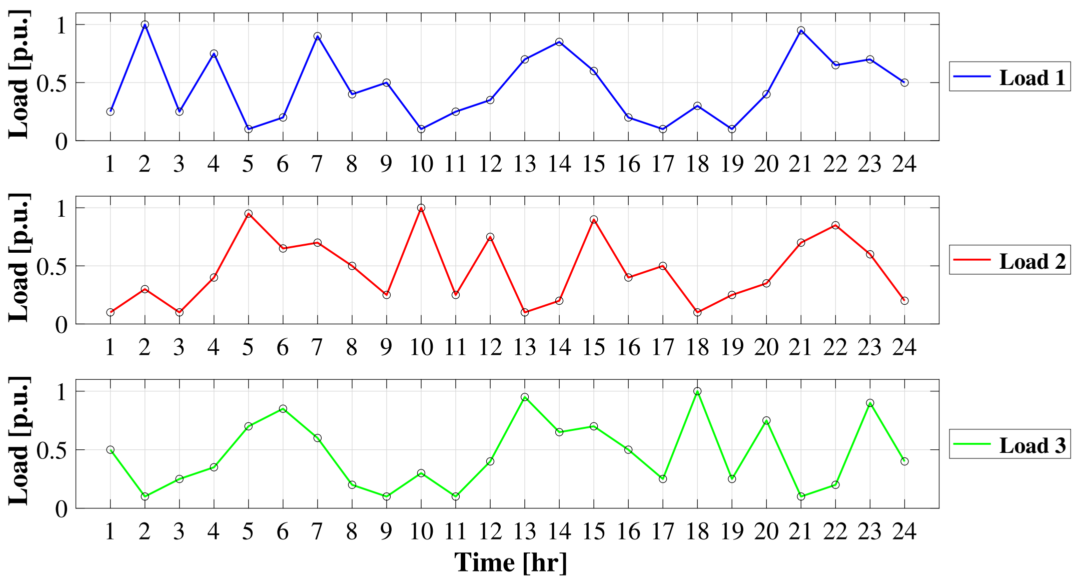

Figure 3.2: Load profile for EOPF.

Table 3.3: Power limits for EOPF cost minimization.

	P_g^{max} [W]	P_g^{min} [W]	Q_g^{max} [VAR]	Q_g^{min} [VAR]
DG_1	2600	300	600	10
DG_2	2600	100	600	10
DG_3	1500	200	600	10

On simulating in MATLAB using *fmincon* function with the default algorithm, the optimization converged to a cost of \$ 6629.38 in 5.95 min with 16 iterations. The optimized droop coefficients are given in Table 3.4. The various results of the simulation are plotted in Figure 3.3 - 3.6.

Table 3.4: Optimized droop coefficients for EOPF cost minimization.

	$\mathbf{K_n}^{\mathbf{p}}$	$\mathbf{K_n}^{\mathbf{q}}$
DG_1	2.5084e-6	4.9988e-4
DG_2	1.7756e-5	4.9988e-4
DG_3	4.5278e-6	2.0050e-5

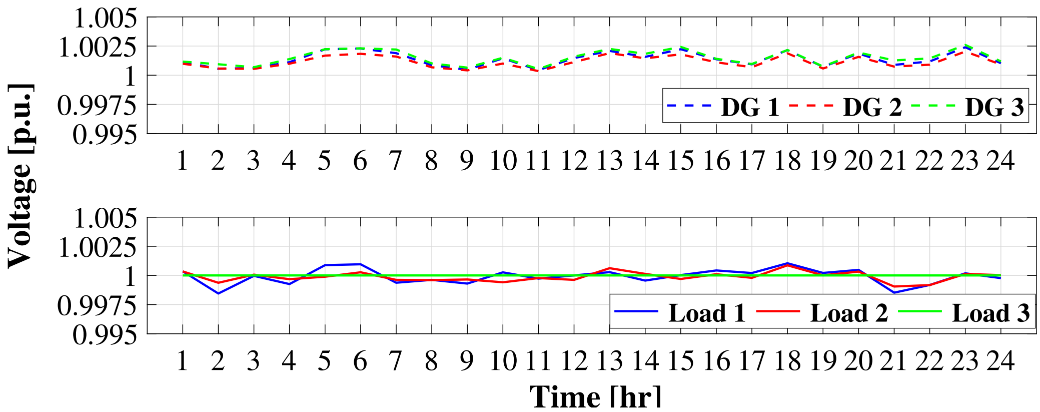

Figure 3.3: DG and load bus voltage for EOPF cost minimization.

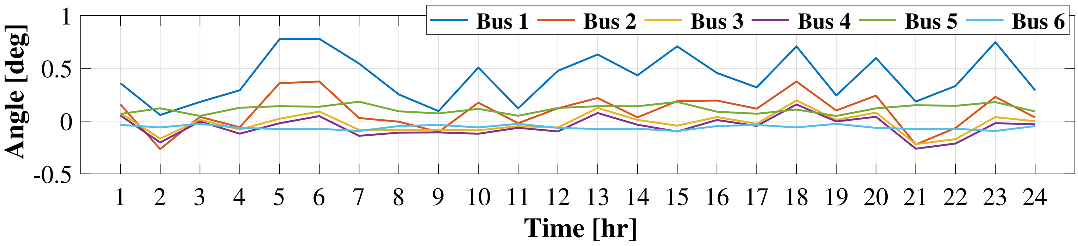

Figure 3.4: Bus angle for EOPF cost minimization.

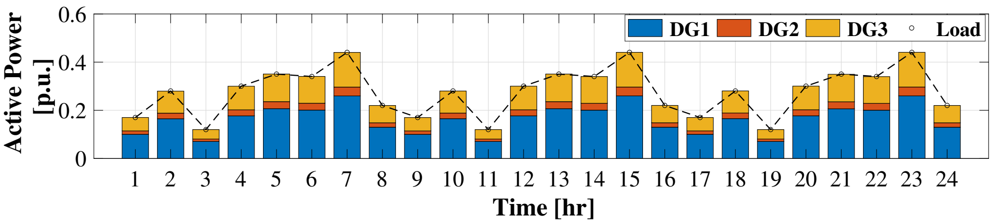

Figure 3.5: DG active power for EOPF cost minimization.

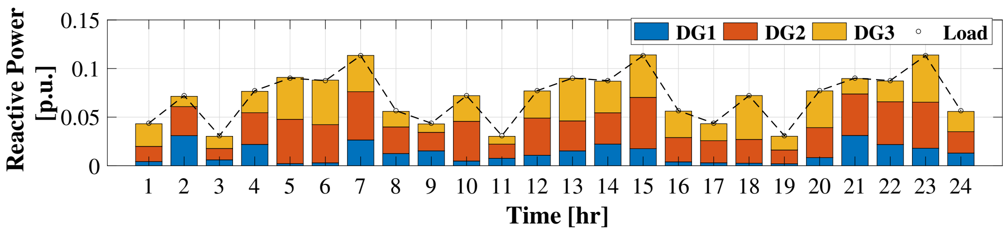

Figure 3.6: DG reactive power for EOPF cost minimization.

As seen from Figure 3.3, the voltages at each bus is very close to 1 p.u. In fact, the voltage at Load

3 (bus 6) is exactly 1 p.u., since this bus is used as the voltage reference in the HCPQ power flow formulation. The bus angle in Figure 3.4 show a minimal phase shift and are close to zero. The active and reactive power contributions from each DG unit is illustrated in Figure 3.5 and 3.6. DG1 has the highest active power contribution, since it has the least cost, and vice-versa for DG2. As clearly seen, the system load is balanced.

3.2.3 Cost Minimization with BESS

The optimization problem in (3.2) is modified by including a storage device. In order to integrate a storage system in the test system, an ideal BESS is modelled as a PQ bus on Bus 4. This is done by introducing a BESS power equation in the power flow formulation's power mismatch vector. The BESS SOC-Power relation given in (2.26) is used to model the ideal BESS.

$$SOC(t) - SOC(t+1) + \frac{1}{E}(\eta_c P_c - \frac{1}{\eta_d P_d})\Delta t = 0 \tag{3.3}$$

The ideal BESS is assumed to have the same the charging and discharging efficiencies (η) which is assumed to be 100%. Furthermore, since the time step is one hour, Δt is also one. In order to include the BESS in the power flow formulation, charging power is taken as negative and discharging power is taken as positive. The final BESS equation becomes the follows,

$$P_{BESS}(t) = -E\ \Delta SOC(t) \tag{3.4}$$

This $\Delta SOC(t)$ variable would be included in the optimization level along with the droop coefficients. It is to be noted that this is a simplified BESS model with only active power support. A real BESS would have also participate in reactive power support [34]. This BESS model is to be included in the power flow formulation along with the HCPQ bus presented in 2.5.1.2. On including the BESS relation in (3.4), the cost minimization problem becomes as follows,

$$\begin{aligned}
&\min_{K_n^p\ K_n^q\ \Delta SOC(t)} \sum_{t=1}^{T_H}\sum_{g=1}^{N_G} \ (a_g P_g^2(t) + b_g P_g(t) + c_g) \\
&\textit{subject to,}\ P_{BESS}(t) + E\ \Delta SOC(t) = 0 \\
&\qquad P_g^{min} - P_g(t) \leq 0 \qquad\qquad P_g(t) - P_g^{max} \leq 0 \\
&\qquad Q_g^{min} - Q_g(t) \leq 0 \qquad\qquad Q_g(t) - Q_g^{max} \leq 0 \\
&\qquad K_n^{q\ min} - K_n^q \leq 0 \qquad\qquad K_n^q - K_n^{q\ max} \leq 0 \\
&\qquad K_n^{p\ min} - K_n^p \leq 0 \qquad\qquad K_n^p - K_n^{p\ max} \leq 0 \\
&\qquad \frac{P_{BESS(d)}}{-E} - \Delta SOC(t) \leq 0 \qquad\qquad \Delta SOC(t) - \frac{P_{BESS(c)}}{-E} \leq 0 \\
&\qquad SOC(t) - SOC^{max} \leq 0 \qquad\qquad SOC^{min} - SOC(t) \leq 0
\end{aligned} \tag{3.5}$$

where E is the BESS capacity, $P_{BESS(c)}$ and $P_{BESS(d)}$ are the charging and discharging limits respectively, SOC^{max} and SOC^{min} are the BESS SOC limits respectively. E was taken as 4000 Wh. $P_{BESS(c)}$ and $P_{BESS(d)}$ were taken as -2400 W and 2400 W respectively. SOC^{max} and SOC^{min} are taken from Table 2.6. It is to be noted that these BESS limits are only for exemplification, and do not represent any real system.

The cost minimization in (3.5) was simulated for 24 hours for the arbitrary load profile given in Figure 3.2. The simulation lasted 34.94 min and took 38 iterations. The cost was minimized to $ 6628.50, which is a decrease of 0.01% as compared to the base case in the previous section. The contribution of the BESS to the cost is minimal since the charging of the BESS by the DG units is cancelled out by the cost saved by discharging the BESS. The optimized droop coefficients are given in Table 3.5.

Table 3.5: Optimized droop coefficients for EOPF cost minimization with BESS.

	$\mathbf{K_n}^\mathbf{p}$	$\mathbf{K_n}^\mathbf{q}$
DG_1	4.8974e-6	2.0019e-5
DG_2	3.8931e-5	5.0e-4
DG_3	1.9465e-5	5.0e-4

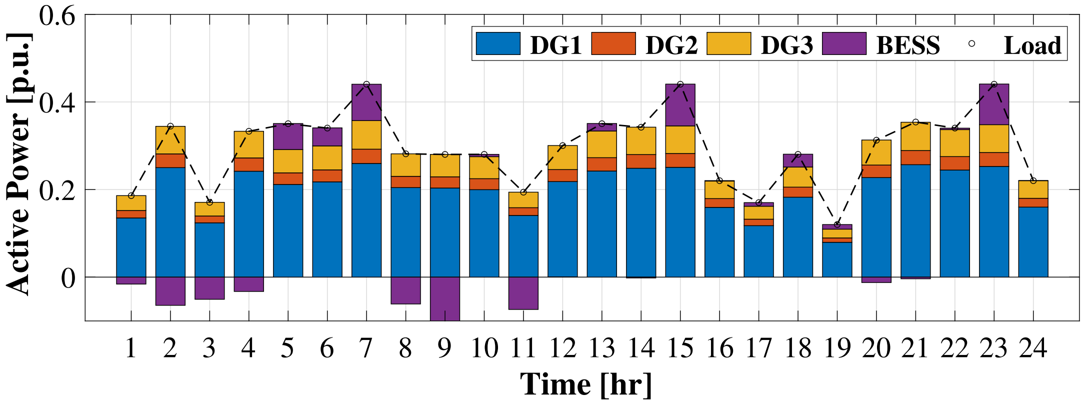

Figure 3.7: DG and BESS active power for EOPF cost minimization with BESS.

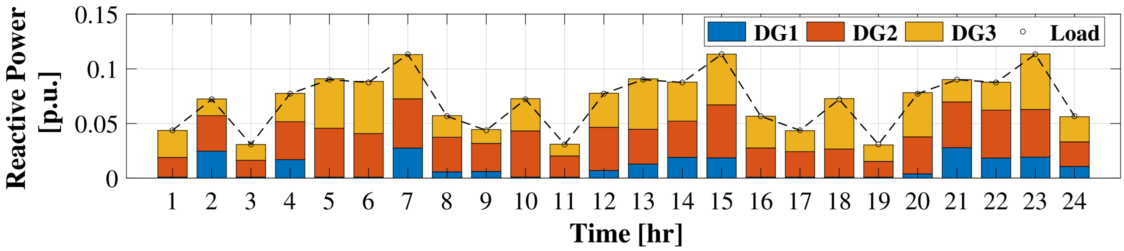

Figure 3.8: DG reactive power for EOPF cost minimization with BESS.

The various results for the EOPF cost minimization are illustrated in Figure 3.7 - 3.12. The active power of the DG units and BESS are given in Figure 3.7, while the reactive power is shown in Figure 3.8.

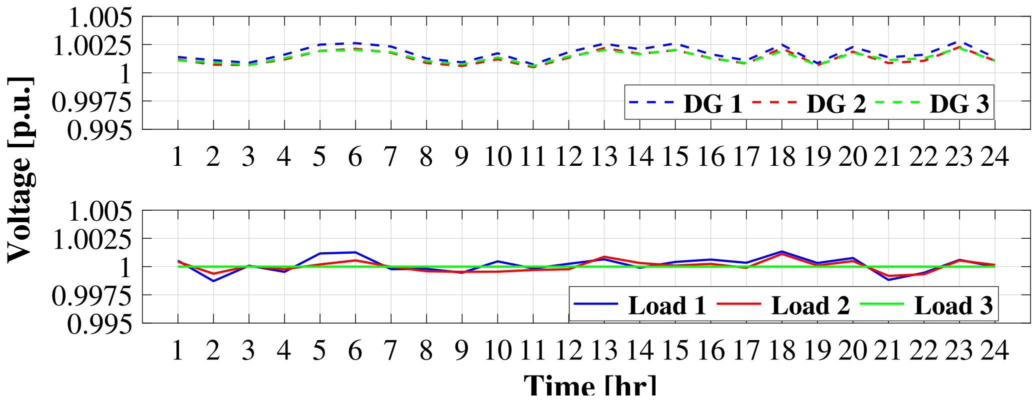

Figure 3.9: Voltage at different buses for EOPF cost minimization with BESS.

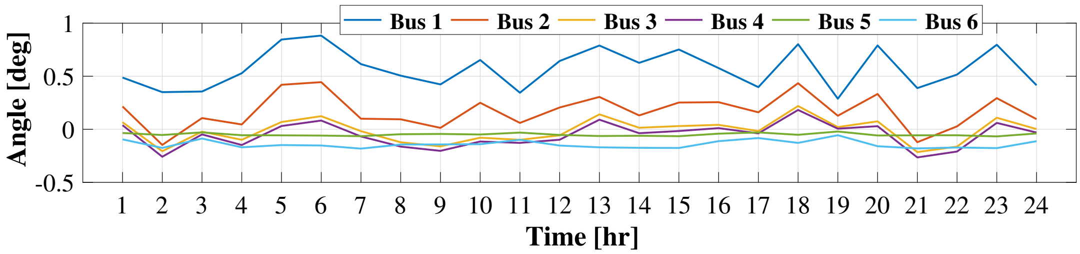

Figure 3.10: Bus angle for EOPF cost minimization with BESS.

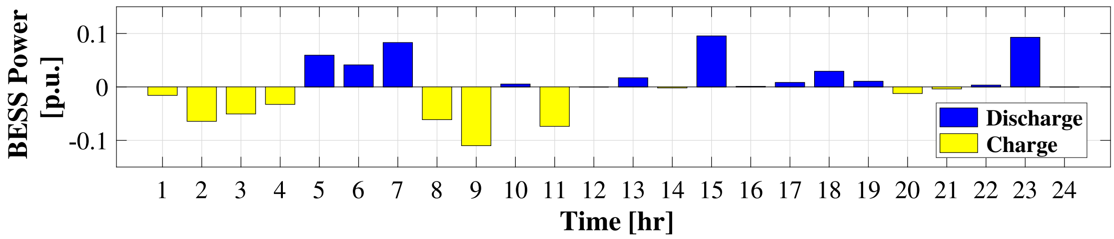

Figure 3.11: BESS charging and discharging power for EOPF cost minimization with BESS.

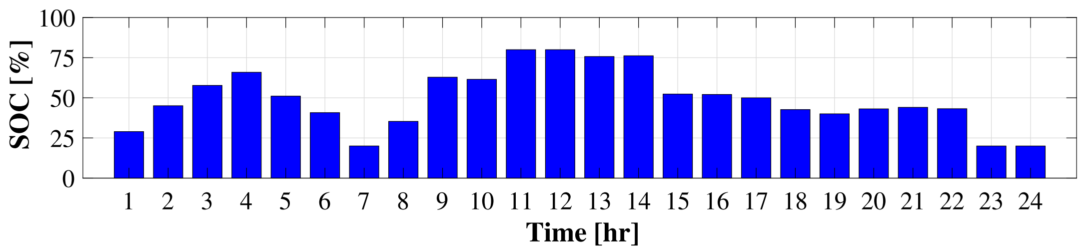

Figure 3.12: BESS SOC for EOPF cost minimization with BESS.

As seen, the system load is balanced by the DGs and the BESS. It is to be noted that the load in Figure 3.7 during the BESS charging hours includes the power used to charge the BESS. The bus voltage magnitudes of the test system are shown in Figure 3.9, and the bus angles are given in Figure 3.10. All the bus voltages are near 1 p.u. for the entire simulation time horizon. Moreover, the voltage of bus 6, i.e., Load 3 is fixed to 1 p.u. because of the secondary voltage control which is included in the formulation. Furthermore, the bus angles show a minimal deviation from zero due to the secondary frequency control included in the HCPQ formulation. The BESS charging-discharging power and SOC are shown in Figure 3.11 and 3.12, respectively and it can be seen that the BESS operates within its limits and the problem of simultaneous charging-discharging observed in 2.6 is also resolved.

3.2.4 Cost Minimization with Load Shedding

The optimization problem in (3.5) is revamped by changing the optimization objective to minimizing cost due to load shedding and DG operation, with the presence of a storage device. This is done by introducing a penalty factor VOLL for all the loads connected in the system, which is assumed to be 10 $\$/W$. Thus, there is a trade-off between increasing the cost due to the load shedding penalty and decreasing the operational cost from DGs. By including load shedding in the equation (3.5) the cost optimization problem becomes as follows,

$$
\begin{aligned}
\min_{K_n^p \ K_n^q \ \Delta SOC(t) \ P_l} \sum_{t=1}^{T_H} \sum_{g=1}^{N_G} \ & (a_g P_g^2(t) + b_g P_g(t) + c_g) + \sum_{t=1}^{T_H} \sum_{l=1}^{N_L} VOLL \cdot P_l(t) \\
\textit{subject to, } & P_{BESS}(t) + E \ \Delta SOC(t) = 0 \\
& P_g^{min} - P_g(t) \leq 0 \\
& P_g(t) - P_g^{max} \leq 0 \\
& Q_g^{min} - Q_g(t) \leq 0 \\
& Q_g(t) - Q_g^{max} \leq 0 \\
& K_n^{q\ min} - K_n^q \leq 0 \\
& K_n^q - K_n^{q\ max} \leq 0 \\
& K_n^{p\ min} - K_n^p \leq 0 \\
& K_n^p - K_n^{p\ max} \leq 0 \\
& \frac{P_{BESS(d)}}{-E} - \Delta SOC(t) \leq 0 \\
& \Delta SOC(t) - \frac{P_{BESS(c)}}{-E} \leq 0 \\
& SOC(t) - SOC^{max} \leq 0 \\
& SOC^{min} - SOC(t) \leq 0 \\
& P_l - P_{LS}^{max} \leq 0 \\
& - P_l \leq 0
\end{aligned}
\tag{3.6}
$$

Where P_{LS}^{max} is the maximum load shedding and it is assumed to be 10% of available load at time t for all the loads connected in the system. The DG power limits and BESS limits are taken from 3.2.3.

The optimization problem was solved for t = 24 with the arbitrary load profiles shown in Figure 3.2. The simulation took 99.68 min and 24 iterations. The cost was minimized to \$ 6625.07. The inclusion of load shedding to the test system reduces the operational cost by 0.06% compared to the base case without BESS and load shedding. The droop coefficients after optimization are given in Table 3.6.

Table 3.6: Optimized droop coefficients for EOPF cost minimization with BESS and load shedding

	$\mathbf{K_n}^{\mathbf{p}}$	$\mathbf{K_n}^{\mathbf{q}}$
DG_1	4.8636e-6	2.2470e-5
DG_2	3.9109e-5	4.9987e-4
DG_3	1.9553e-6	2.9970e-4

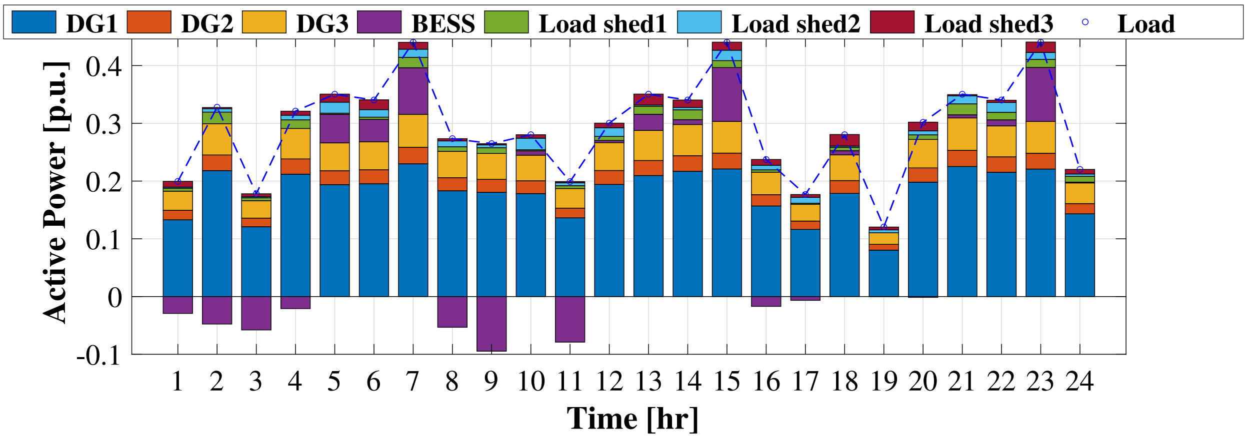

Figure 3.13: DG and BESS active power for EOPF cost minimization with BESS and load shedding.

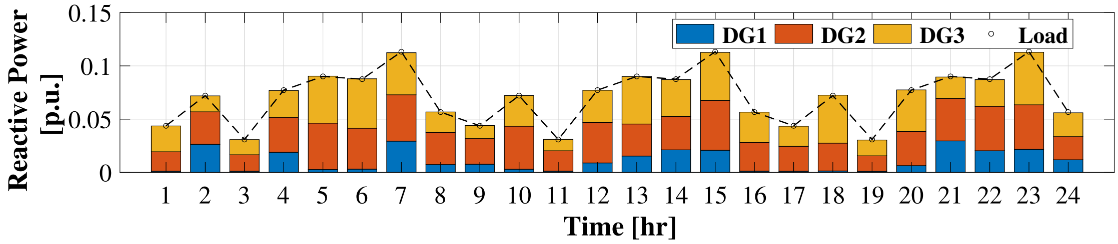

Figure 3.14: DG reactive power for EOPF cost minimization with BESS and load shedding.

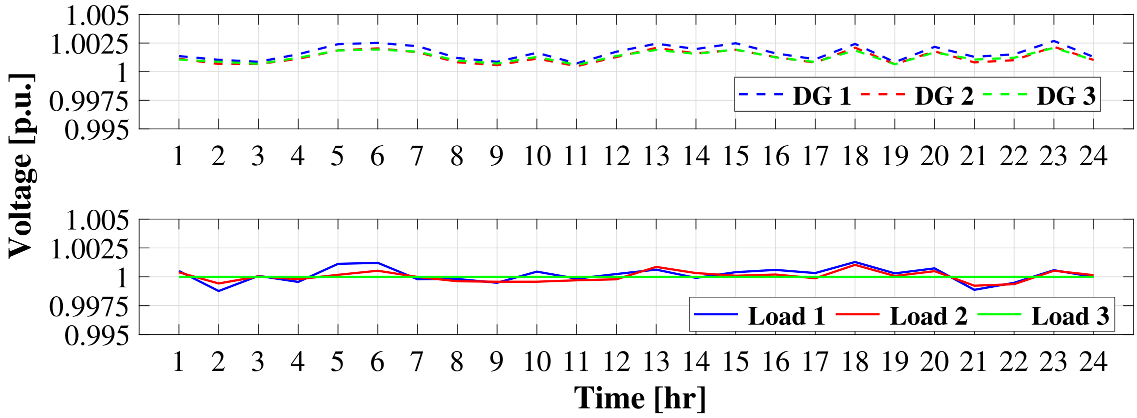

Figure 3.15: Voltage at different buses for EOPF cost minimization with BESS and load shedding.

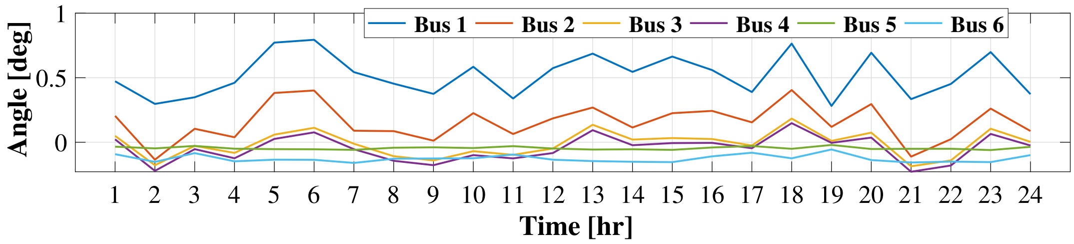

Figure 3.16: Bus angles for EOPF cost minimization with BESS and load shedding.

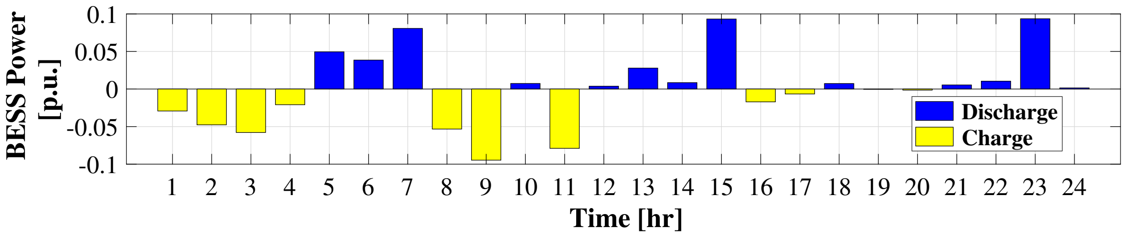

Figure 3.17: BESS charging and discharging power for EOPF cost minimization with BESS and load shedding.

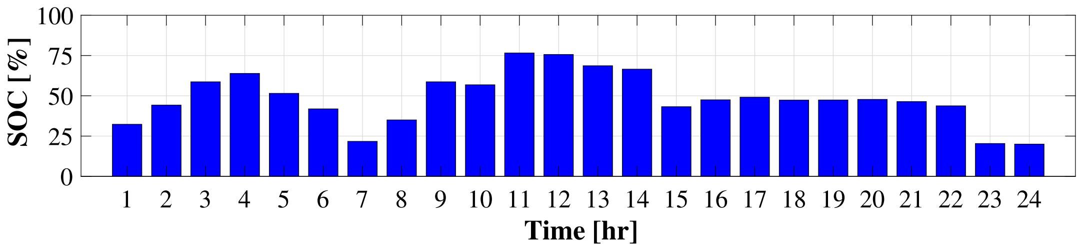

Figure 3.18: BESS SOC for EOPF cost minimization with BESS and load shedding.

The results for EOPF cost minimization with load shedding in the presence of BESS are shown in Figure 3.13-3.18. Figure 3.13 shows the curtailment of load for t=24 to minimize the cost, while the reactive power is shown in Figure 3.14. In Figure 3.13, the sum of the DG power, the load shed and BESS contribution amount to the total available load in the system at that hour. The bus voltage magnitudes are near to 1 p.u. for the given test system as shown in Figure 3.15 and the bus angles are close to zero and illustrated in Figure 3.16. The BESS charging-discharging power and SOC are shown in Figure 3.17 and 3.18 and it can be seen that the BESS operates within its limits.

3.3 Summary

In this chapter, the extended optimal power flow algorithm with HCPQ bus is presented and tested for various cases. The proposed hierarchical scheme includes a tertiary level control to meet various optimization objectives such as equal active power and reactive power sharing, cost minimization with BESS, and cost minimization with load shedding. The results obtained from the case studies indicate that the application of the proposed hierarchically control EOPF scheme contribute to an optimized and reliable operation of the microgrid.

Table 3.7: Summary of results for EOPF cost minimization.

Case	Time [min]	Iterations	Cost [$]
Base	5.95	16	6629.38
With BESS	34.94	38	6628.50
With Load Shedding	99.68	24	6625.07

A Summary of the cost minimization results are given in Table 3.7. The inclusion of a BESS to the EOPF problem increases the complexity of the problem, however, it may help in reducing the cost of the system if at least one of the DG units has a very low or zero operating cost, such as RES. The cost associated with RES is usually for curtailment rather than operation. Hence, the inclusion of a BESS in a system with RES would reduce the system cost by charging from the RES power, reducing RES curtailment, and then discharging to reduce the power contribution from the costly DGs. The inclusion of load shedding further increases the complexity, but the cost can be decreased. For load shedding to be effective, the cost of shedding the load, i.e., $VOLL$ should be comparatively much less than the cost of operating DGs. In general, load shedding is feasible when the load demand is larger than the available power generation.

To further validate the proposed hierarchical scheme, the algorithm will be tested on a CIGRE benchmark system in the following chapters.

4 | CIGRE Microgrid: Power Flow

4.1 Introduction

In this chapter, the steady-state power flow analysis is carried out for a modified CIGRE benchmark microgrid with a 12.47 kV MV distribution network [35, 36, 37]. Initially, the steady-state analysis using the conventional power flow is performed. Later, from the results of this study, selection of buses for the hierarchical extended power flow analysis is done, in order to maintain the bus voltage magnitudes and system frequency at their desirable values.

4.2 CIGRE Microgrid Topology

The single line diagram of the modified CIGRE benchmark network is shown in Figure 4.1. There is no connection to the main grid, hence the microgrid is islanded. It has Solar Photo-Voltaic (SPV) panels, WTs, CG units and BESS as DERs. The line parameters for the system are given in the Table B.1 in Appendix B. The transformer parameters (480 V/12.47 kV) connected between bus 14 and 1 are taken from [35] and are given in Table B.2 in Appendix B.

The loads that are included in the network are aggregated loads and are separated as industrial and household loads as shown in the Table B.3 in Appendix B. Each industrial and household load follows the same load patterns respectively with different load scaling based on the power consumption by the consumers. The hourly industrial and household load profile is shown in Figure B.1 in Appendix B.

The total generation capacity in the modified CIGRE benchmark system in [35, 37] is much higher than the load. Hence, the grid was further modified by removing the 2500 kW and 800 kW units from bus 14. The microgrid now has a total DG capacity of 4290 kW and a BESS of capacity 1000 kWh, with its parameters given in Table B.5 in Appendix B. DER with different capacity connected to each bus are listed in the Table B.4 in Appendix B. The typical hourly normalized wind and solar PV output profiles are taken from [37] and are shown in Figure B.2 in Appendix B. The voltage limits are considered as +5% and -10% of the nominal value as per IEC 60038 [38] and from EN 50160 [39], and the frequency limits of $\pm 1\%$ of nominal frequency are considered for the power flow analysis of the MV modified CIGRE microgrid.

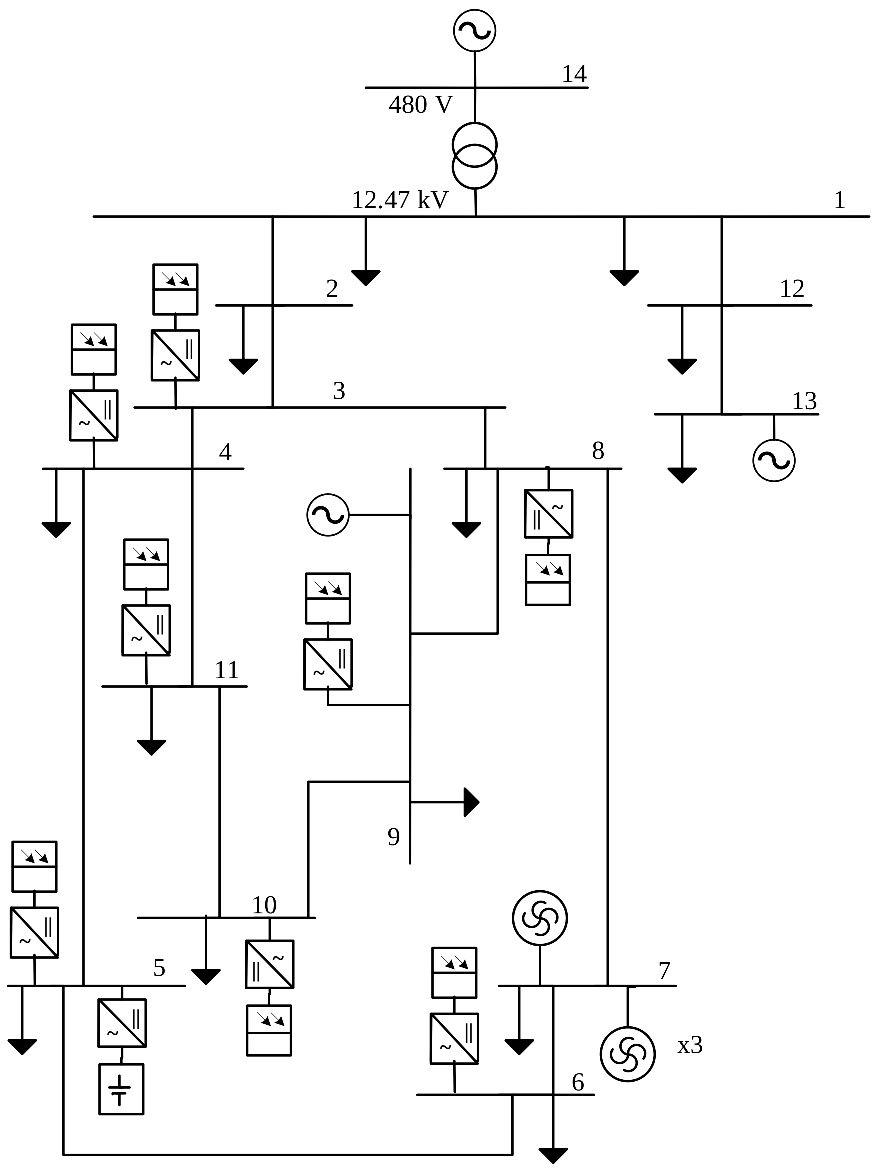

Figure 4.1: Modified CIGRE benchmark network.

4.3 Power Flow Case Study

To improve the steady state behaviour of the modified CIGRE microgrid benchmark, it is imperative to first perform a power flow analysis before deciding which processes to optimize. For this purpose, a power flow based case study is performed in this chapter. The inferences from this study would act as a reference when discussing the results in the EOPF-based case study in chapter 5.

Two power flow based case studies are considered in this chapter, which differ in their methodology. In the first case, a conventional power flow study is performed on the modified CIGRE benchmark microgrid. This is done in order to examine the behaviour of the system assuming it as a conventional power system network. The results of this study are used to determine which buses need to be controlled using the HCPQ bus formulation described in 2.5.1.2. This directly leads to the next case, which is based on HC of microgrid power flow using the HCPQ bus method. The results from this case would be more accurate as they would better represent the dynamics of the microgrid and its components, and also address some of the assumptions made in the conventional power flow case. Finally, the shortcoming of this case would be identified and addressed in the next chapter, which includes an EOPF-based case study. The power flow based cases are described in detail below. The tolerance for NR was set to 10^{-6}.

1. Case 0: Conventional Power Flow
    - Bus 14 is considered as slack bus.
    - Buses 1-13 are considered as PQ buses.
    - BESS is neglected.
    - The RES generate based on their hourly profile. The CGs generate at a fixed capacity. The DGs, RES and CGs, in the system are considered to have the same percentage of maximum capacity. Consequently, two sub-cases are simulated with the following percentage of maximum available capacity:
        - 100%
        - 50%
    - Based on the bus voltage magnitudes observed in this case, the buses which exceed the voltage limit will be controlled in the next case.
2. Case 1: HC Power Flow
    - Bus 14 is considered as PV bus.
    - Buses 1, 2, 12 and 13 are considered as PQ buses.
    - Based on the results from case 0, buses 3-11 are either HCPQ buses or PQ buses.
    - BESS is neglected.
    - The CGs in the system are considered to generate the same percentage of maximum capacity. The share is chosen based on the results of case 0.
    - Droop coefficients are estimated using the droop equations (2.1) and (2.2).
    - Based on the results obtained, the constraints and optimization variables for the optimization level would be decided.

4.4 Simulation Results

The two cases described in 4.3 were simulated in MATLAB and the results are described below. The total system load capacity is 0.4425 p.u. for active load, and 0.0841 p.u. for reactive load, based on the data given in Table B.3 in Appendix B. The system base value was chosen as 1000 kVA. Since the total DG capacity is 4290 kW, the load was increased by a factor of 3. The power factor was taken as 0.8, which is used to calculate the reactive power capacities of the DG units.

4.4.1 Case 0: Conventional Power Flow

The results of the simulation for the model in Figure 4.1 with 100% DG capacity are illustrated in Figure 4.2 - 4.4. From Figure 4.2, it can be seen that the voltage magnitude exceeds the +5% limit for buses 3-11 during $t = 10$ to $t = 21$.

It should be noted that these buses are the the buses with RES. The bus angles deviate by less than a couple degrees from zero, as seen from Figure 4.3.

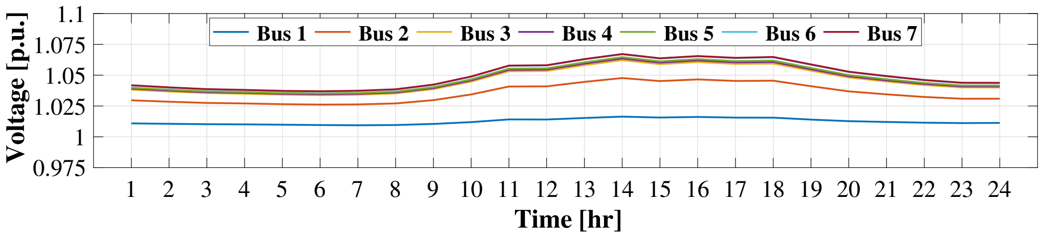

(a) Bus 1-7

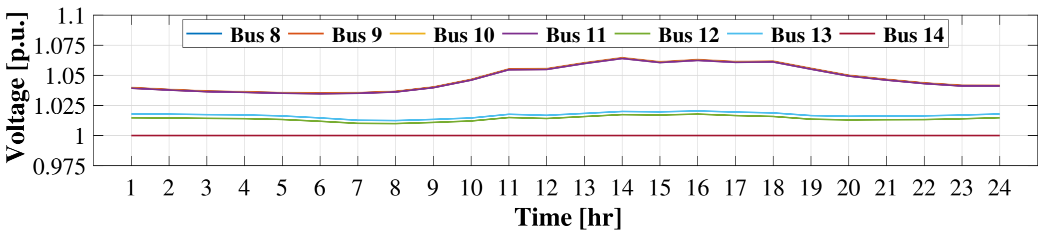

(b) Bus 8-14

Figure 4.2: Bus voltage magnitude for case 0 with 100% DG capacity.

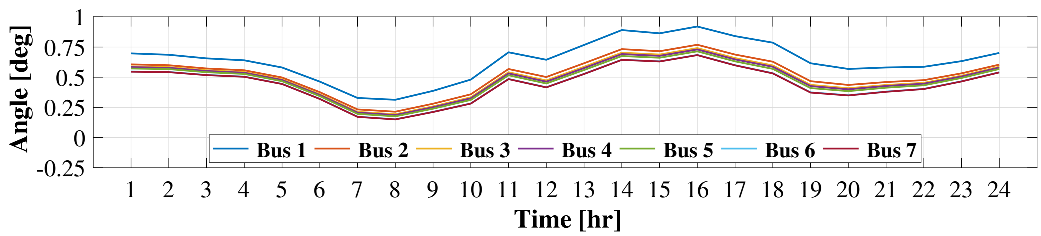

(a) Bus 1-7

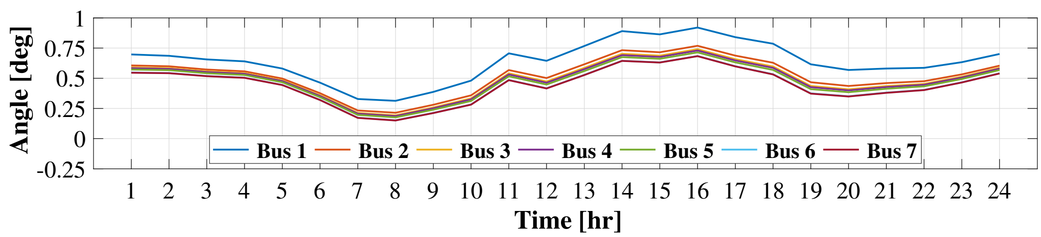

(b) Bus 8-14

Figure 4.3: Bus angles for case 0 with 100% DG capacity.

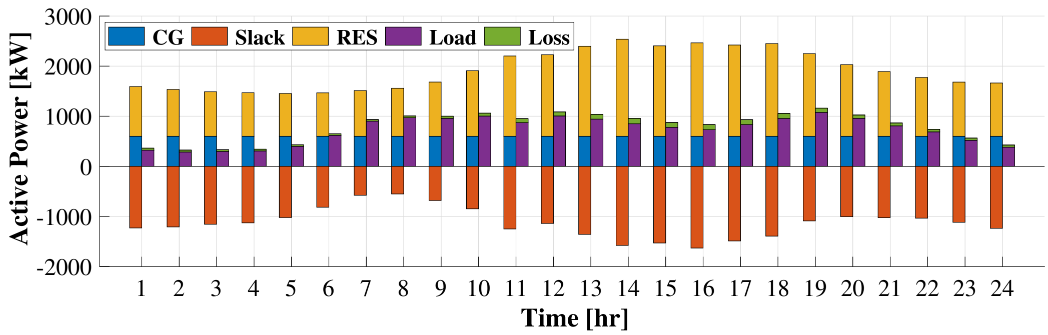

(a) Active Power

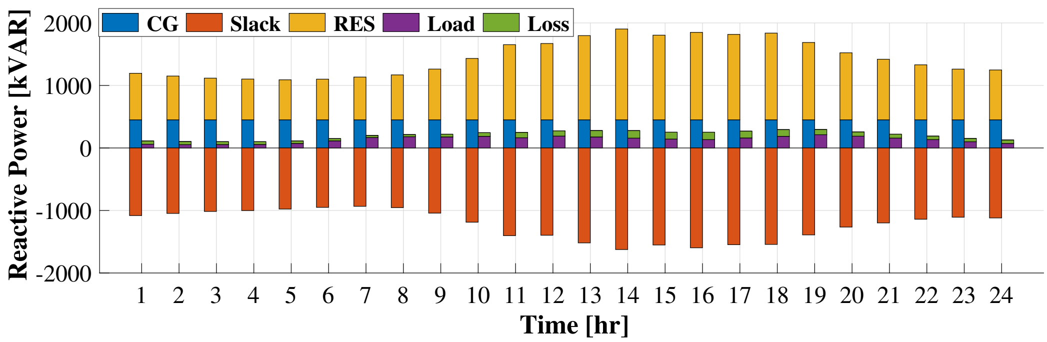

(b) Reactive Power

Figure 4.4: Power balance for case 0 with 100% DG capacity.

In Figure 4.4, it is noticed that since the CGs and RES generate to their maximum capacity, the slack needs to absorb the excess active and reactive power in order to bring the system in balance. To observe the change in this behaviour, the DG capacity needs to be reduced. Hence the other sub-case with 50% capacities becomes relevant to the study. The results for 50% case are given in Figure 4.5, 4.6 and in Figure C.1 in Appendix C. Figure 4.5 indicates that the maximum voltage magnitude for buses 3-11 drops down to +3% on reducing the DG capacities.

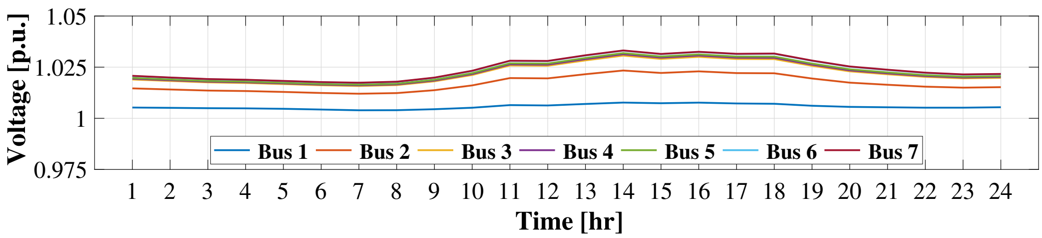

(a) Bus 1-7

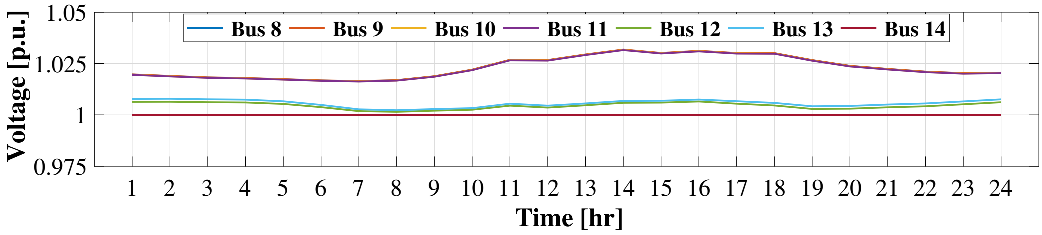

(b) Bus 8-14

Figure 4.5: Bus voltage magnitude for case 0 with 50% DG capacity.

The bus angle in Figure C.1 shows no change that could be of any significance to the study. The decrease in DG capacity shows an improvement in active power balance in Figure 4.6., but only for some hours. Since there is no curtailment of RES power, the slack bus is required to absorb the excess power. The reactive power behaviour, however, does not change.

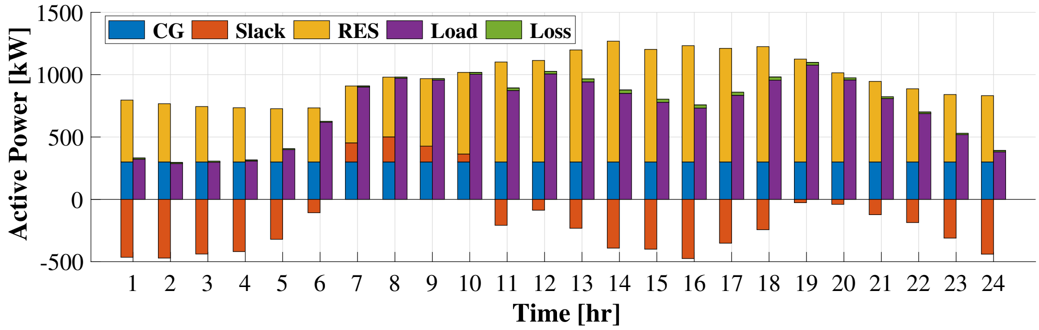

(a) Active Power

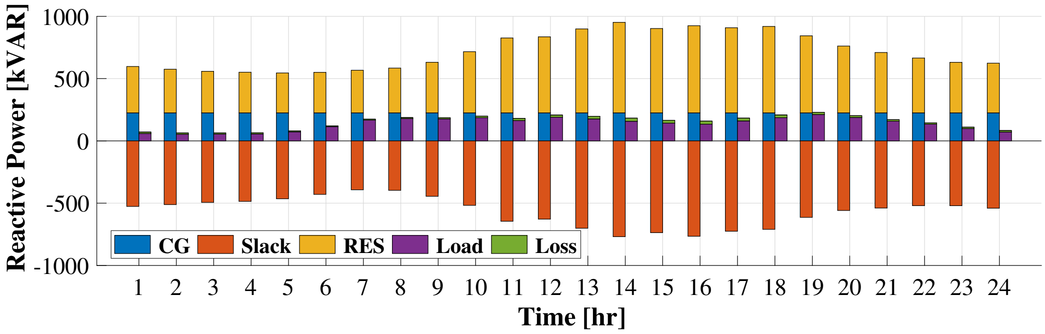

(b) Reactive Power

Figure 4.6: Power balance for case 0 with 50% DG capacity.

Each sub-case took 4-5 iterations for each hour and the total system losses are given in Table 4.1. The convergence error at each hour was in the order of 10^{-7} or smaller. The losses in the system decrease significantly with the decrease in DG capacity, although they are still quite high. This suggests that the system generation needs to be better managed. In the next case, the percentage share of each CGs is taken as 10%. It may be, however, noted that the only CG present in the system in case 0 are on bus 9 and 13 of capacity 300 kW each, since bus 14 is considered as a slack bus. Finally, it may be concluded that buses 3-11 are needed to be controlled as HCPQ buses in order to reduce RES generation output and maintain the bus voltage magnitude within the admissible limits, as close to 1 p.u as possible. Moreover, bus 14 cannot be a slack bus since it has a limited capacity. Furthermore, it can only generate active power and not absorb it, contrary to what the results with active power balance suggest. Hence it should be made a PV bus.

Table 4.1: Active and reactive power system loss for case 0.

DG Capacity	Active Power Loss [kW]	Reactive Power Loss [kVAR]
100%	1490.29	1664.51
50%	376.71	348.70
% change	295.61	377.34

4.4.2 Case 1: Controlled Power Flow

After analyzing the simulation results from case 0, case 1 was simulated in MATLAB. Each hour took 2-3 iterations to converge with a convergence error of 10^{-7} or smaller. Buses 3-11 were taken as references to control the voltage on their respective bus. Bus 1 was taken as the reference bus for secondary frequency control. The secondary frequency control parameter k_{iw} was taken as 4, as given in Table B.1, and the droop coefficients were as given in Table C.1 in Appendix C. These droop coefficients are calculated based on the droop equations by using the reference frequency, reference voltage and RES active and reactive power capacities, to get the droop coefficients k_p and k_q respectively. To estimate an accurate set of droop coefficients, they need to be included to the set of optimization variables.

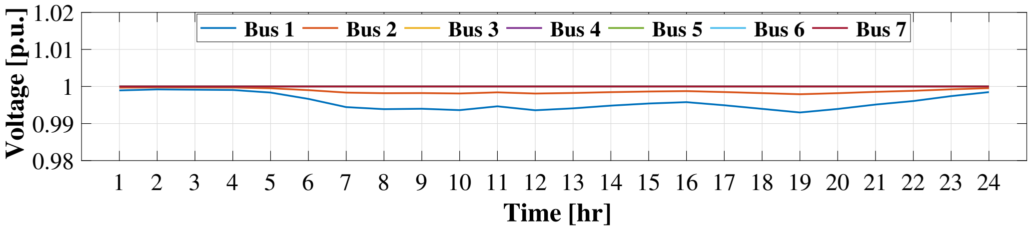

(a) Bus 1-7

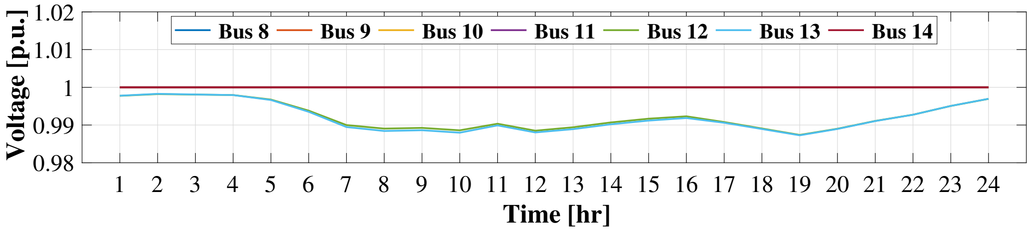

(b) Bus 8-14

Figure 4.7: Bus voltage magnitude for case 1 with 10% CG capacity.

The bus voltage was controlled to stay within the limits. In fact, since the reference voltage for HCPQ buses was taken as 1 p.u., buses 3-11 had 1 p.u. voltage throughout the time horizon. This can be seen from Figure 4.7. Figure 4.8 indicates that the bus angles have a small phase shift, but are close to 0 deg.

Figure 4.9 shows the system hourly power balance with 10% CG capacity. While the active power is properly balanced, the problem of excess reactive power still persists. This is due to the fact that

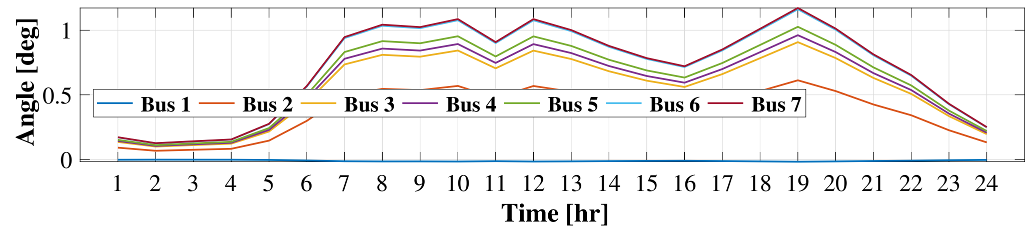

(a) Bus 1-7

(b) Bus 8-14

Figure 4.8: Bus angles for case 1 with 10% CG capacity.

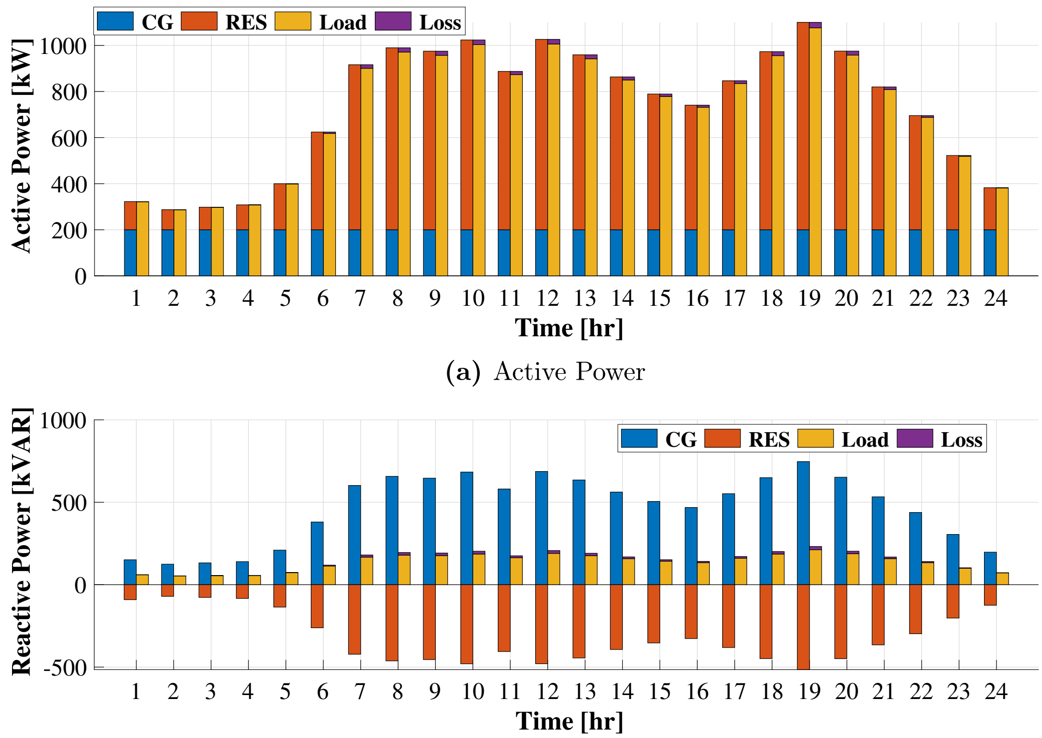

(a) Active Power

(b) Reactive Power

Figure 4.9: Power balance for case 1 with 10% CG capacity.

the PV bus (bus 14) is required to be maintained at 1 p.u. Therefore, the CG on bus 14 generates reactive power to maintain that voltage level and consequently there is an excess of reactive power in the system. This power is absorbed by the HCPQ buses connected to RES, which themselves are also required to maintain 1 p.u. at their buses. In order to reduce the reactive power contribution by the CG at bus 14, the PV bus voltage needs to be reduced. In the following scenario, the PV bus voltage is reduced to 0.995 p.u.

4.4.2.1 Decrease in PV Bus Voltage

On decreasing the PV bus voltage to 0.995 p.u., as shown in Figure 4.10, the reactive power contribution from the CG on bus 14 decreases. This is illustrated in Figure 4.11. The bus angles and active power balance are given in Figure C.2 and C.3 in Appendix C. However, there is still an issue of excess reactive power. It is observed that during the day time, the CG gives excessive reactive power, whereas during the night the RES give excess reactive power. In order to further improve the reactive power balance, the voltage at the HCPQ buses can be increased.

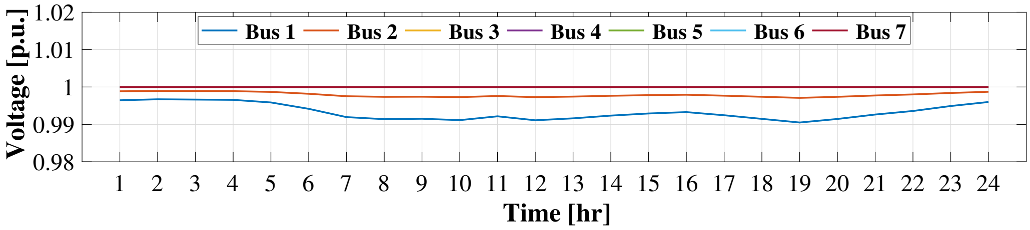

(a) Bus 1-7

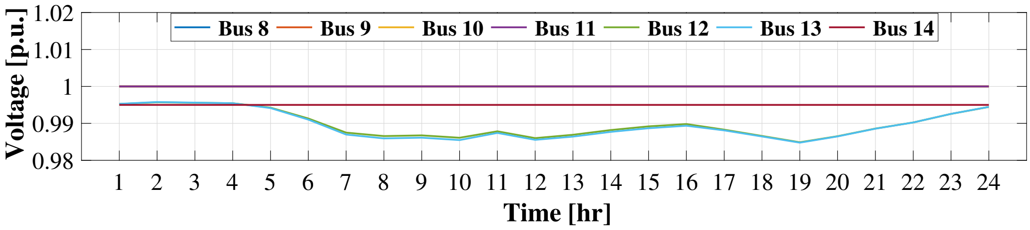

(b) Bus 8-14

Figure 4.10: Bus voltage magnitude for case 1 with PV bus voltage 0.995 p.u.

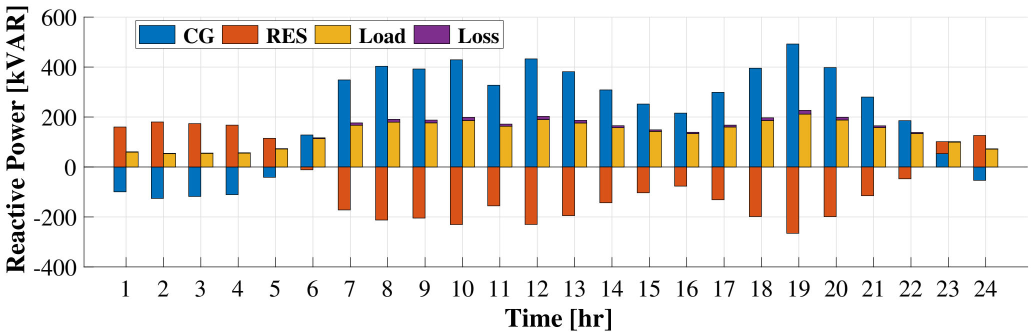

Figure 4.11: Reactive power balance for case 1 with PV bus voltage 0.995 p.u.

4.4.2.2 Increase in HCPQ Bus Voltage

Due to the effect of the droop control dynamics, the voltage-reactive power relation is inverse for HCPQ buses. In order to reduce the reactive power contribution from the HCPQ buses, their reference voltage must be increased. In this scenario, the HCPQ reference voltage is increased to 1.005 p.u, as shown in Figure 4.12. The bus angles and active power balance are given in Figure C.4 and C.5 in Appendix C. The reactive power is balanced for more than half of the time horizon, as given in Figure 4.13. Table 4.2

compares the system loss for the three scenarios discussed in case 1 simulations. A notable change in reactive power loss is observed on changing the reference voltages. Finally, it may be concluded that the varying voltage references are needed for the PV and HCPQ buses throughout the time horizon in order to observe proper reactive balance.

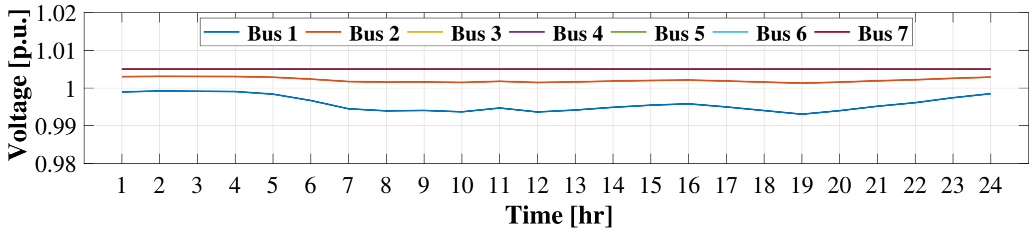

(a) Bus 1-7

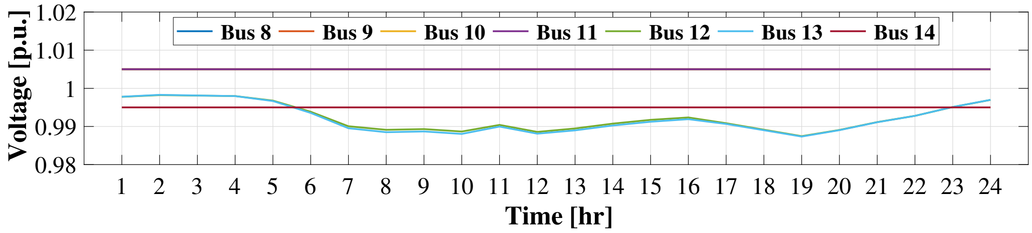

(b) Bus 8-14

Figure 4.12: Bus voltage magnitude for case 1 with PV bus voltage 0.995 p.u. and HCPQ bus voltage 1.005 p.u.

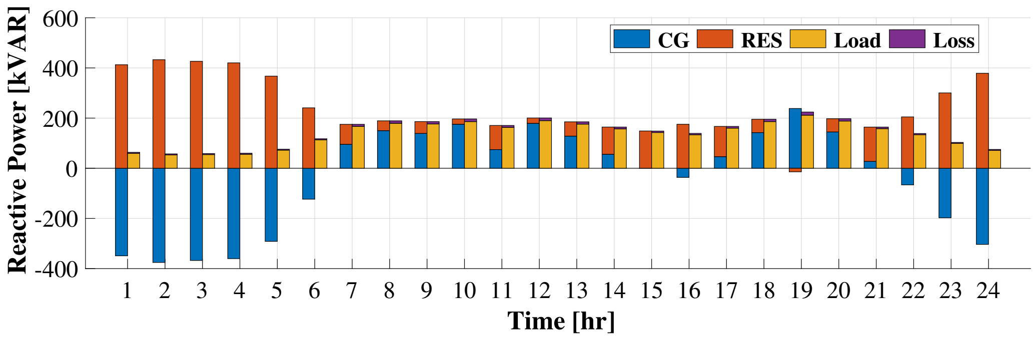

Figure 4.13: Reactive power balance for case 1 with PV bus voltage 0.995 p.u. and HCPQ bus voltage 1.005 p.u.

Table 4.2: Active and reactive power system loss for case 1.

PV Bus Voltage [p.u.]	HCPQ Bus Voltage [p.u.]	Active Power Loss [kW]	Reactive Power Loss [kVAR]
1	1	260.40	233.80
0.995	1	233.38	163.73
0.995	1.005	230.64	163.03

In order to effectively utilize the RES generation, a BESS is needed in the system. Secondly, the generation capacities of the CGs need to be taken into account, along with the maximum and minimum generation limits of all DGs. Furthermore, it may also be asserted to put soft voltage limits on the

HCPQ bus and PV bus. This would allow more flexibility in the system by not burdening the DGs to provide the required amount of reactive power in order to maintain 1 p.u. bus voltage. Finally, an appropriate selection of droop coefficients is also required. These constraints can be included in the tertiary level of control, i.e., the optimization level.

4.5 Summary

This chapter discussed the topology of a modified MV CIGRE benchmark microgrid that is used in this study. The system is examined by initially performing a conventional power flow analysis. However, that requires certain assumptions such as the need of a slack bus, a fixed system frequency, and pre-defined active and reactive powers of the DGs. Based on the outcomes, a controlled microgrid power flow study is performed which also addresses the aforementioned assumptions of the conventional study. Nevertheless, the controlled power flow is also not completely robust and requires a higher level of optimization so as to take certain system and component constraints into account. For this purpose, this study is extended in the next chapter to investigate EOPF in the CIGRE network.

5 | CIGRE Microgrid: EOPF

5.1 Introduction

Based on the results and conclusions drawn from 4.4.2, there is a need for a tertiary control level to optimize system operation while ensuring the system components operate within their operational limits. The study of the MV CIGRE benchmark microgrid illustrated in Figure 4.1 is, therefore, extended to include optimization, along with the hierarchically-controlled power flow. Hence, in this chapter, the EOPF analysis is implemented for the modified CIGRE benchmark network. To facilitate this, the control algorithm for EOPF described in Figure 3.1 in 3.2 is explored for different optimization objectives which are stated below,

1. Case 2: Minimizing the operational cost of CGs and RES curtailment.
2. Case 3: Minimizing the operational cost of CGs with the inclusion of load shedding constraints.

5.2 Case 2: Renewable Power Curtailment

The increased penetration of RES into the distribution network minimizes the contribution of CGs to supply the required demand and reduces environmental emissions. However, when RES penetration is more than the actual demand in the system it causes many problems such as excessive line losses, overloading of transformers and feeders, protection failure, over-voltage issues, etc [40]. Hence, there is a need for RES curtailment. This is achieved by introducing a penalty factor for RES curtailed power, which is assumed as $50\$/MW$ throughout this study. The cost coefficients for the CGs were taken from [35, 37] and are also given in Table B.6 in Appendix B. The inclusion of RES curtailment in the optimization objective is expected to complement the minimization of CG operational cost, and increase the RES utilization. Moreover, the presence of BESS in the system would further aid the objective by managing the excess, or deficit, RES power and in turn, reduce the overall operating cost in the system.

Based on the inferences from the power flow analysis in chapter 4, the following changes are made to the optimization formulation, in order to incorporate the EOPF algorithm. Firstly, voltage soft limits are included for PV and HCPQ buses. The reason for this is to allow for flexibility in the system, so that the DGs are not required to maintain exactly 1 p.u. on their respective buses. The reference power for all the CGs is calculated in the optimization, and then given to the controlled power flow layer.

The minimum reactive power that can be generated by a given DG for reactive power compensation is decided by the unit operator and is assumed to be zero for simplicity in this study. The boundaries for the droop coefficients are assumed as follows,

$$2 \times 10^{-7} \leq K_n^p \leq 5 \times 10^{-4} \qquad (5.1) \qquad\qquad 2 \times 10^{-6} \leq K_n^p \leq 5 \times 10^{-3} \qquad (5.2)$$

The most prominent change is in the functioning of the HCPQ buses with SPV, i.e., all HCPQ buses except bus 7, during different durations of the time horizon. The time horizon can be broadly broken down into two categories described below, which can also be seen in Figure B.2 in Appendix B

- Night phase: t=1 to t=6, and t=22 to t=24
- Day phase: t=7 to t=21

The optimization requires the HCPQ buses to generate within the upper and lower bounds. The lower bound is fixed to zero, as mentioned earlier, and the upper bound is based on the DG capacity and power profile. During the night phase there is zero solar power. Hence, the optimization would require the solar HCPQ buses to generate exactly zero active and reactive power. However, as per the HCPQ bus active power equation (2.19) , which is also given below, for power to be zero, either $\delta_m = \delta_m^0$ or K_n^p should be extremely large. Similarly as per the reactive power equation from (2.20), either $|V_n^*| - |V_n| + U_v^{int} = 0$ or K_n^q should be extremely large.

$$P_n^{(scheduled)} = \frac{-K^{iw}(\delta_m - \delta_m^0)}{K_n^p} \qquad\qquad Q_n^{(scheduled)} = \frac{|V_n^*| - |V_n| + U_v^{int}}{K_n^q}$$

Either of these are not feasible. The droop coefficients have an upper limit, and the bus angle cannot be made exactly equal to its reference value, given the presence of loads also on those buses. If the bus voltage is fixed to its reference value, only the secondary voltage integral parameter U_v^{int} and droop coefficient K_n^q affect the scheduled reactive power of the bus. Dividing these two parameters cannot give a value which would satisfy the optimization constraint tolerance. Hence, to solve this issue, the solar HCPQ buses were made as PQ buses during the night phase with P and Q set to zero.

To investigate the system behaviour, different scenarios for RES curtailment are considered in this section, as given below,

1. Change in voltage soft limits for PV and HCPQ buses.
2. Change in DG power factor.
3. Presence of non-linear load.

In all scenarios, the optimization variables are

- the droop coefficients,
- hourly change in BESS SOC (The initial SOC is assumed to be 50%.),
- hourly active and reactive power references of CGs on HCPQ bus 9 and PQ bus 13,
- hourly active power references for CG on PV bus 14,
- and voltage soft limits for PV and HCPQ buses.

The optimization problem is thus formulated as follows,

$$
\begin{aligned}
&\min_{x} \sum_{t=1}^{T_H} \sum_{g=1}^{N_G} \left(a_g P_g^2(t) + b_g P_g(t) + c_g\right) + \sum_{t=1}^{T_H} \sum_{N=1}^{N_{RES}} C_{RES} \cdot P_{RES}(t) \\
&\quad \textit{where, } x = \{K_n^p,\ K_n^q,\ \Delta SOC(t),\ P_{CG},\ Q_{CG},\ V_{PV} \textit{ and } V_{HCPQ}\} \\
&\textit{subject to, } P_{BESS}(t) + E \cdot \Delta SOC(t) = 0 \\
&\qquad P_{g,\ RES}^{min} - P_{g,\ RES}(t) \leq 0 \\
&\qquad P_{g,\ RES}(t) - P_{g,\ RES}^{max} \leq 0 \\
&\qquad Q_{g,\ RES}^{min} - Q_{g,\ RES}(t) \leq 0 \\
&\qquad Q_{g,\ RES}(t) - Q_{g,\ RES}^{max} \leq 0 \\
&\qquad K_n^{q\ min} - K_n^q \leq 0 \\
&\qquad K_n^q - K_n^{q\ max} \leq 0 \\
&\qquad K_n^{p\ min} - K_n^p \leq 0 \\
&\qquad K_n^p - K_n^{p\ max} \leq 0 \\
&\qquad \frac{P_{BESS(d)}}{-E} - \Delta SOC(t) \leq 0 \\
&\qquad \Delta SOC(t) - \frac{P_{BESS(c)}}{-E} \leq 0 \\
&\qquad SOC(t) - SOC^{max} \leq 0 \\
&\qquad SOC^{min} - SOC(t) \leq 0 \\
&\qquad V_{PV,\ HCPQ} - V_{PV,\ HCPQ}^{max} \leq 0 \\
&\qquad V_{PV,\ HCPQ}^{min} - V_{PV,\ HCPQ} \leq 0
\end{aligned}
\tag{5.3}
$$

The simulations were performed in MATLAB using *fmincon* function with *SQP* algorithm. As per MATLAB documentation, the *SQP* algorithm, is much faster than the default *interior-point* algorithm and takes a lesser number of iterations, comparatively. The MATLAB code for this case is given in Appendix F. Comments in the code have also been provided for the reader's understanding. The same code can also be used for the different scenarios or the Load Shedding case with minor modifications.

5.2.1 Voltage Soft Limit

In this section, cost minimization with RES curtailment is performed with two different voltage soft limits for both PV and HCPQ buses, namely, ±1% and ±2% p.u. soft limits. These voltage variables are included in the optimization level. These voltage variables are then used as references for the respective buses in the hierarchically controlled power flow level. The simulations took 16.08 and 7.63 hours with 36 and 14 iterations respectively, for the two scenarios. The cost obtained in two scenarios was equal to $ 682575.29 and $ 682150.38, respectively. The various results for the two scenarios are illustrated in Figure 5.1-5.6.

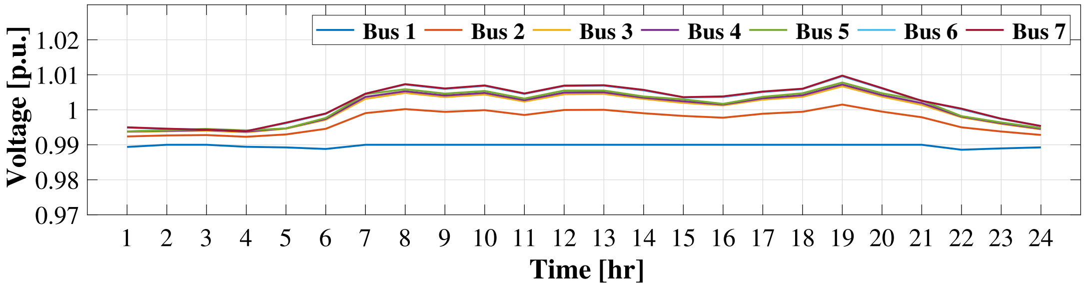

(a) Bus 1-7

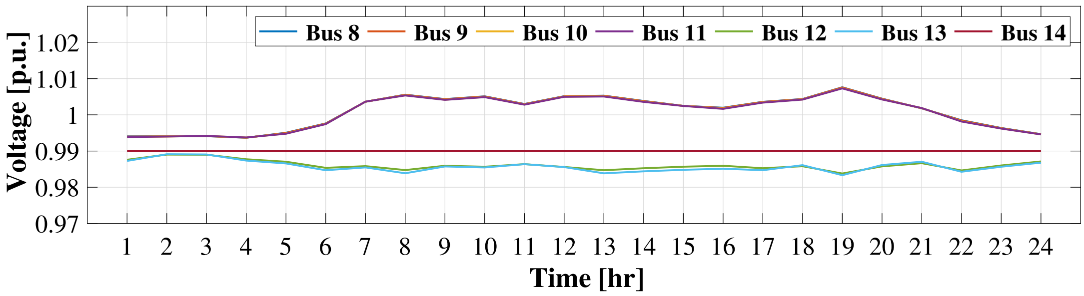

(b) Bus 8-14

Figure 5.1: Bus voltage magnitude for case 2 with 1% voltage soft limits.

As observed from Figure 5.1, the ±1% soft voltage limit facilitates the voltage for HCPQ buses 3-11 to be above 1 p.u. during the day hours, thereby effecting the reactive power contribution of the HCPQ buses. Only buses 1, 12 and 13 fall slightly below the 1% voltage limit but that is because those are PQ buses. In comparison for ±2% soft limits in Figure 5.2, the HCPQ bus voltage drops below 1 p.u. during the day hours causing the RES reactive power contribution to be more in contrast to the ±1% soft limit scenario. This is also evident from Figure 5.3 and 5.4 which show the active and reactive power balance for the two scenarios.

In both scenarios, there is no contribution from the CGs towards the active power balance, which is in order with the optimization objectives of minimization of CG operational cost and RES curtailment. The utilized and available hourly RES active power for both scenarios is displayed in Figure 5.5 and

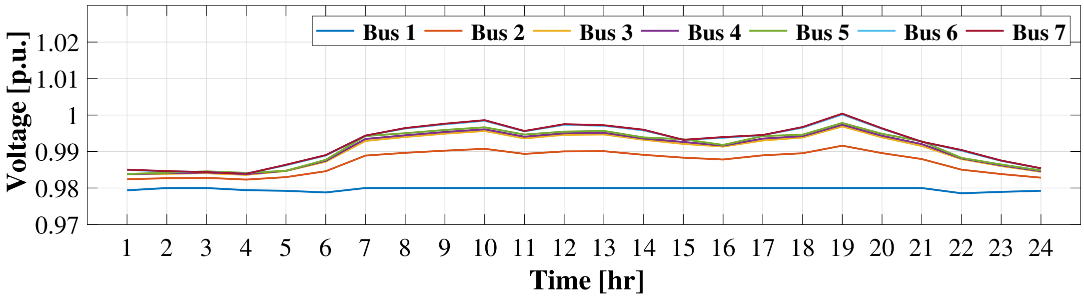

(a) Bus 1-7

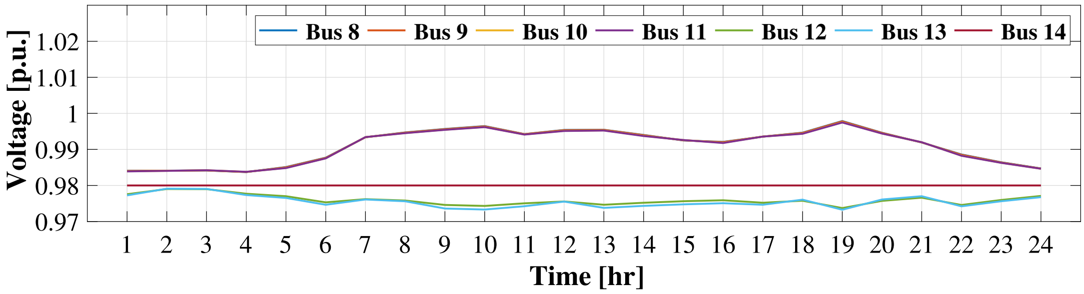

(b) Bus 8-14

Figure 5.2: Bus voltage magnitude for case 2 with 2% voltage soft limits.

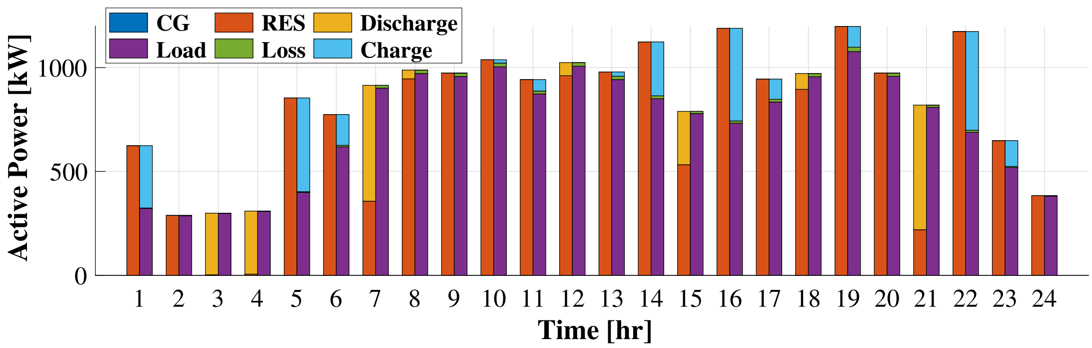

(a) Active Power

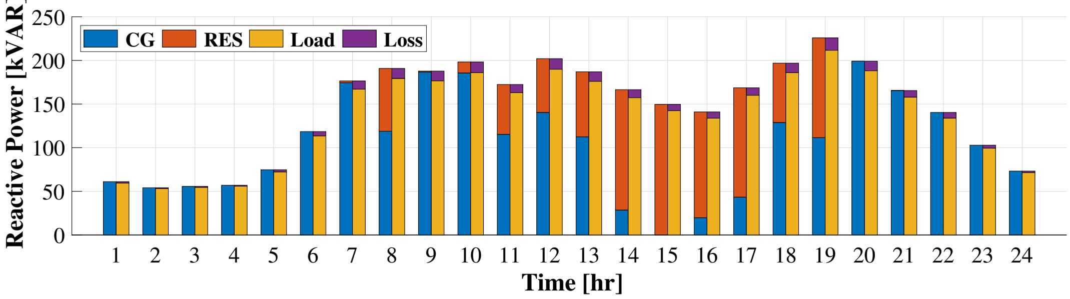

(b) Reactive Power

Figure 5.3: Power balance for case 2 with 1% voltage soft limits.

5.6. In ±1% limit scenario, 55.98% of the RES power is utilized, whereas in the other scenario 56.01% is used. The change in voltage soft limit has a marginal affect on the RES utilization. The BESS, on the other hand, certainly assists in the optimization objective by managing the excess RES active

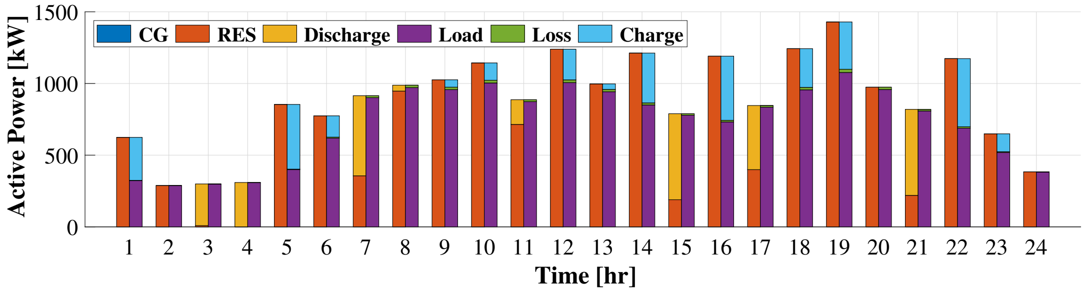

(a) Active Power

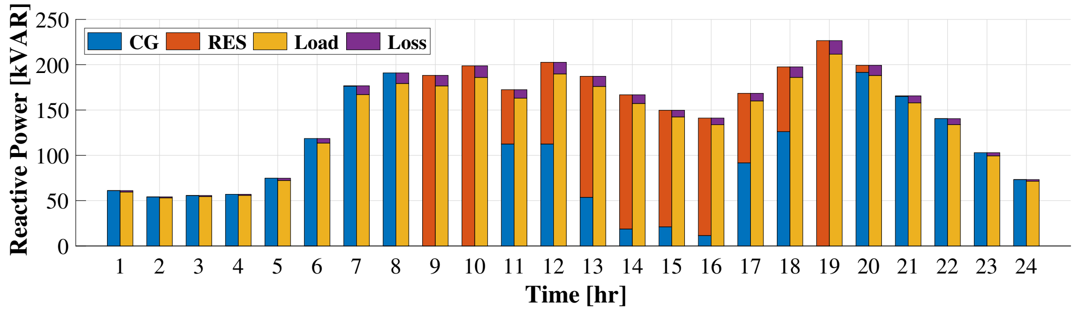

(b) Reactive Power

Figure 5.4: Power balance for case 2 with 2% voltage soft limits.

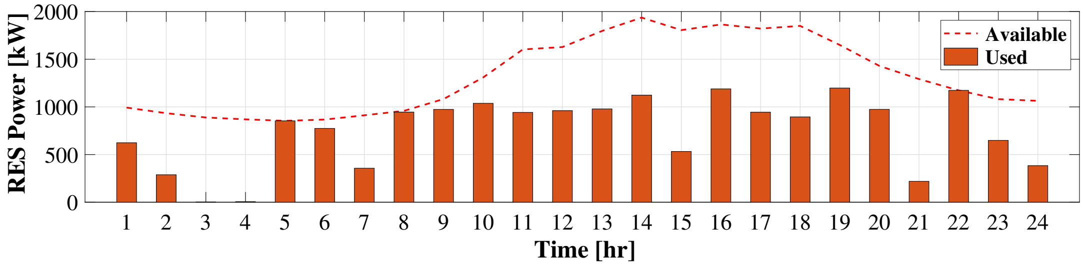

Figure 5.5: RES curtailment for case 2 with 1% voltage soft limits.

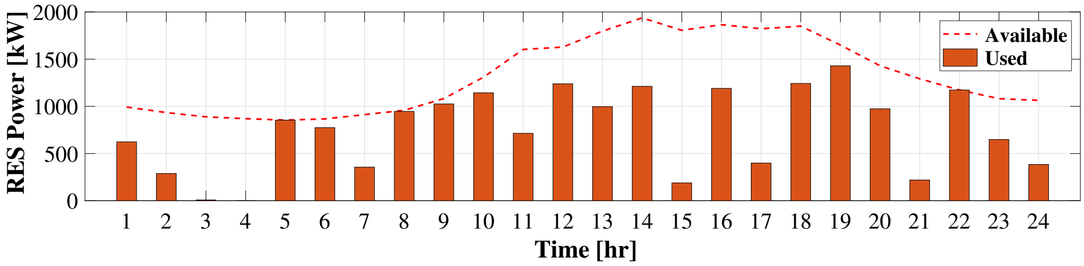

Figure 5.6: RES curtailment for case 2 with 2% voltage soft limits.

power, which is also evident from the power balance results. The BESS charging and discharging power, and SOC are given in Figure 5.7 and 5.8.

Finally, the bus angles are shown in Figure 5.9 and 5.10, and as seen there is very little phase shift in the bus angles.

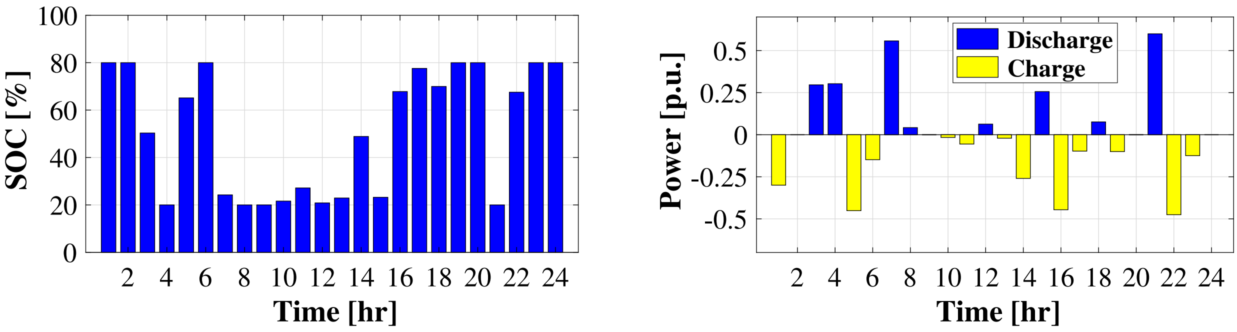

(a) SOC (b) BESS Power

Figure 5.7: BESS usage for case 2 with 1% voltage soft limits.

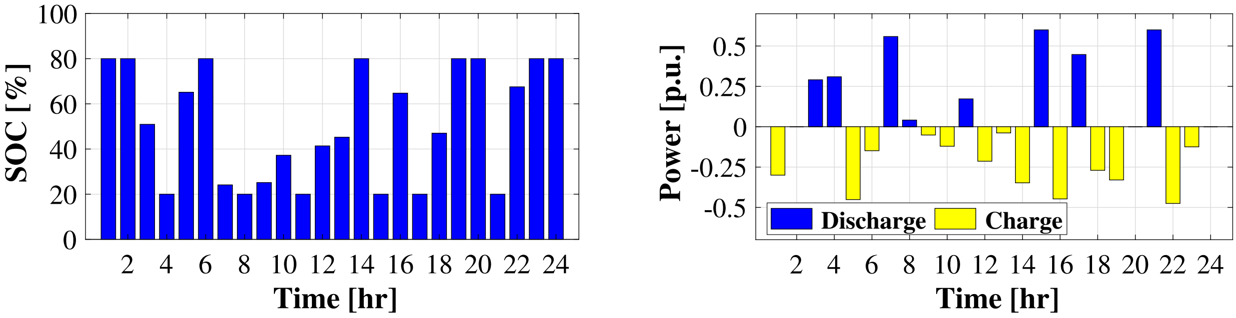

(a) SOC (b) BESS Power

Figure 5.8: BESS usage for case 2 with 2% voltage soft limits.

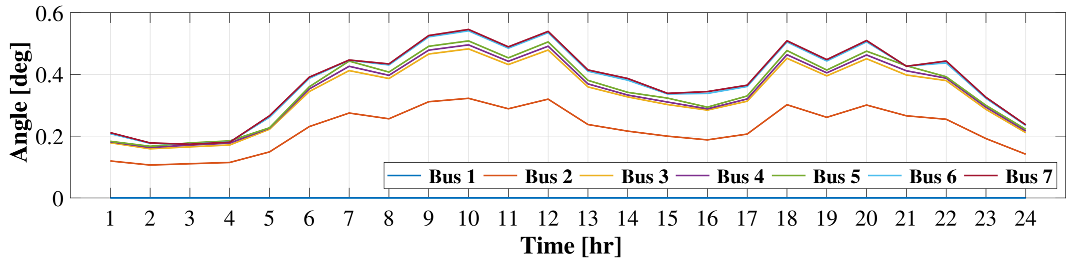

(a) Bus 1-7

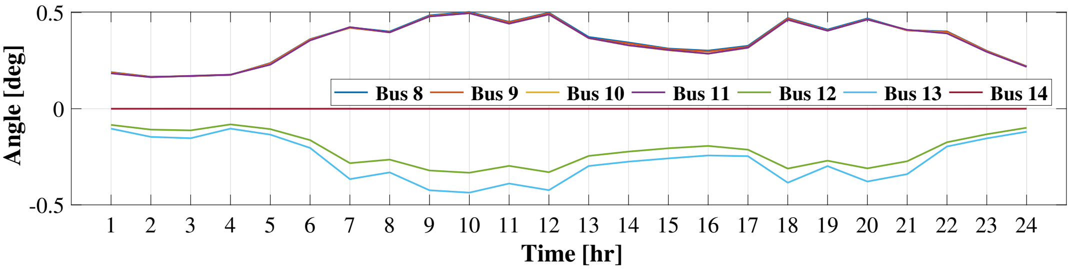

(b) Bus 8-14

Figure 5.9: Bus angle for case 2 with 1% voltage soft limits.

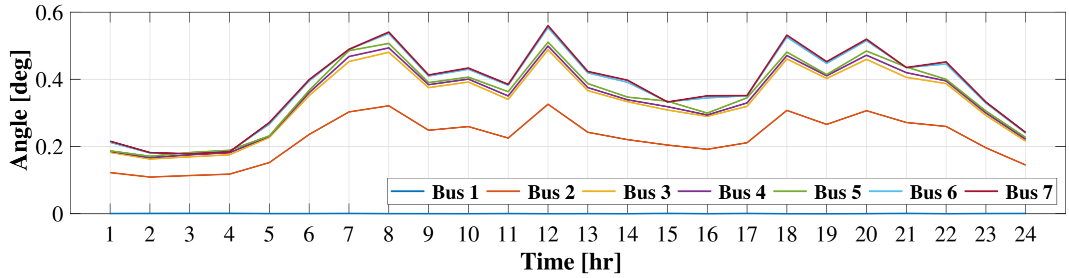

(a) Bus 1-7

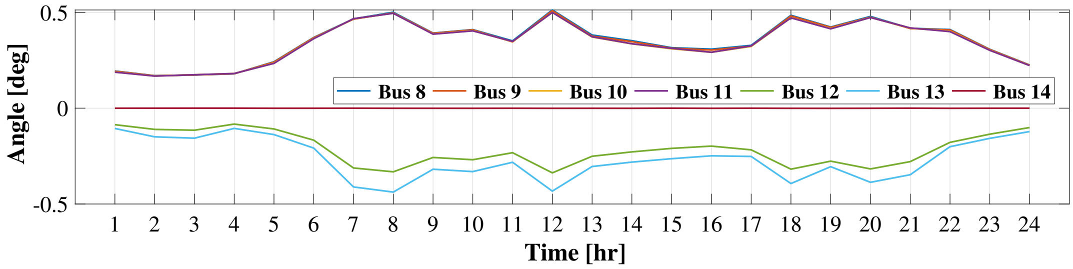

(b) Bus 8-14

Figure 5.10: Bus angle for case 2 with 2% voltage soft limits.

5.2.2 DG Power Factor

In this scenario to investigate the system behaviour for change in power factor is analyzed. The CG cost minimization with RES curtailment is performed by changing the DG power factor from 0.8 to 0.9 and the voltage soft limits of PV and HCPQ buses is ±1%. The simulation optimized to a cost of $ 682324.43 and it took 7.4 hours with 16 iterations.

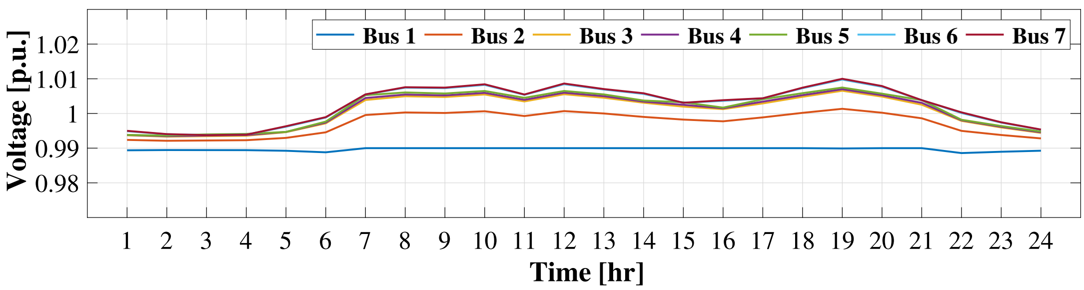

(a) Bus 1-7

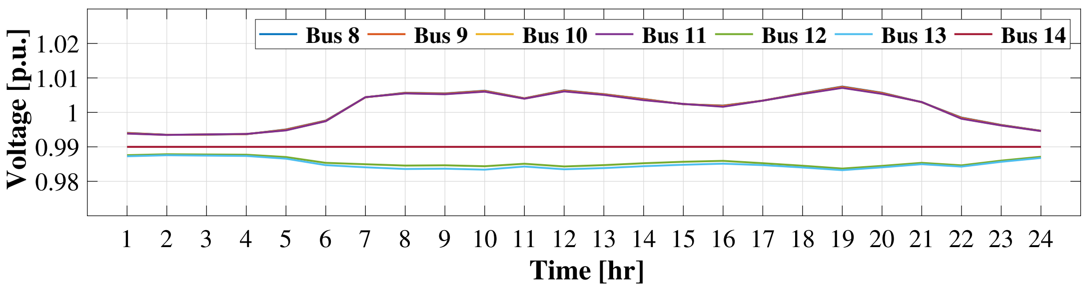

(b) Bus 8-14

Figure 5.11: Bus voltage magnitude for case 2 with 0.9 DG power factor.

The various results of the simulation are shown in Figure 5.11-D.2. As observed from Figure 5.11, the voltage for HCPQ buses 3-11 lies between ±1% limit of nominal voltage and the voltage for PQ buses 1, 12 and 13 falls slightly below the 1% voltage limit.

From Figure 5.12 it is observed that the reactive power contribution from RES increases in comparison with Figure 5.3, to ensure the voltage at HCPQ bus is between ±1% voltage soft limits. Since the DG power factor has increased, the reactive power capacities, and hence reactive generation by the CGs also decreases. Therefore, to compensate this decrease and balance the load, the RES are required to give more reactive power.

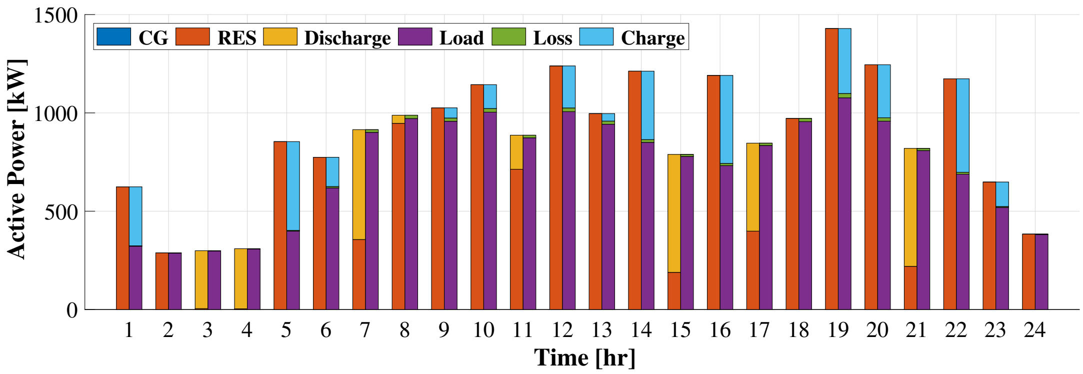

(a) Active Power

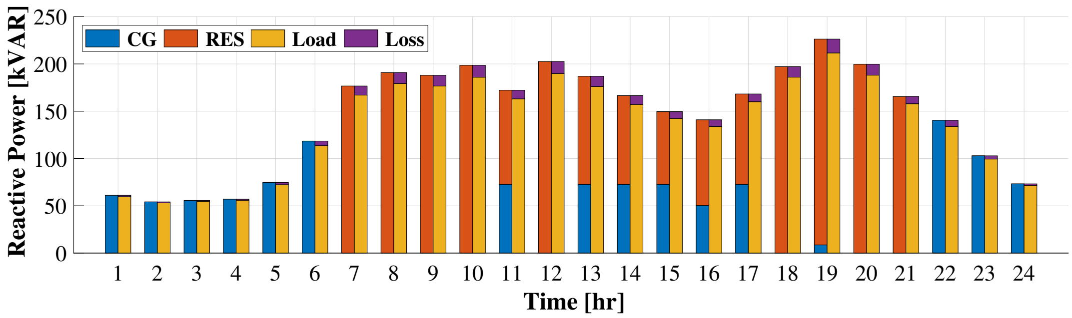

(b) Reactive Power

Figure 5.12: Power balance for case 2 with 0.9 DG power factor.

The active power contribution is only by RES and BESS to minimize CG operational cost and RES curtailment. The utilized and available active power from RES is given in Figure D.1 and there is an increase of 0.02 % of RES power utilized which reduces the cost by 0.036% as compared to the scenario with 0.8 power factor and ±1% voltage soft limits. The SOC and BESS charging and discharging power, given in Figure D.2 in Appendix D, shows that the net BESS contribution is slightly increased in contrast with Figure 5.7 by satisfying the optimization objective of the system. This is based on the fact that the total BESS discharging and charging power for the entire time horizon increased by 37.56% and 33.05% respectively. Finally the bus angles are given in Figure D.3 in Appendix D.

5.2.3 Non-Linear Loads

In this scenario, the optimization is carried out by including voltage-dependent non-linear loads in the MV CIGRE benchmark network. The linear loads connected to bus 3 and 12 are replaced by voltage-dependent non-linear load. The non-linear industrial load at bus 3 and non-linear household load at 12 are expressed as [41],

$$\begin{aligned} P_{L,3}(t) &= P_{L,3}(t)\ V_3(t)^{\alpha} \\ Q_{L,3}(t) &= Q_{L,3}(t)\ V_3(t)^{\beta} \\ P_{L,12}(t) &= P_{L,12}(t)\ V_{12}(t)^{\alpha} \\ Q_{L,12}(t) &= Q_{L,12}(t)\ V_{12}(t)^{\beta} \end{aligned} \tag{5.4}$$

where t= 1 to T_H, P_L and Q_L are the active power and reactive power of load for time t, the α and β values for industrial and household loads are given in Table 5.1.

Table 5.1: Non-linear loads parameters [41].

Bus no.	Load Type	α	β
3	Industrial	0.18	6
12	Household	0.72	2.96

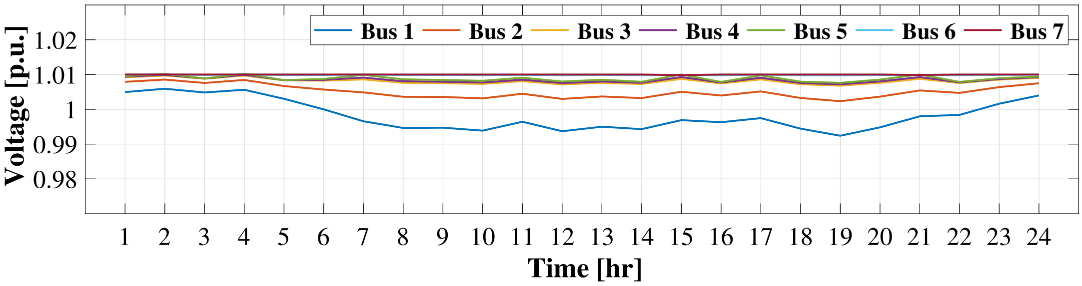

(a) Bus 1-7

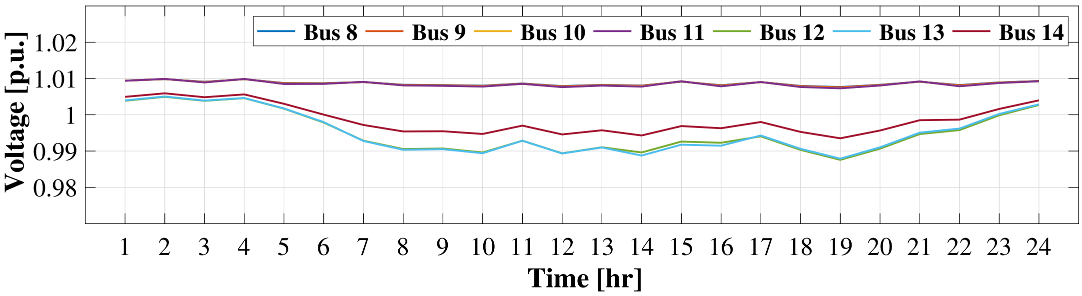

(b) Bus 8-14

Figure 5.13: Bus voltage magnitude for case 2 with non-linear loads.

The simulation resulted to a cost of \$ 684126.74 in 5.94 hours with 13 iterations. The various results for simulation are illustrated in Figure 5.13-D.5. From Figure 5.13 it is seen that the voltage at all buses has slightly increased for the entire time horizon in the presence of non-linear loads compared to Figure 5.3.

The active power and reactive power balance are shown in Figure 5.14. Since bus 3 is HCPQ bus the voltage is optimized to more than 1 p.u. over the time horizon T_H and therefore the load increases by 0.141 kW on this bus than compared to the scenario with 0.8 power factor and ±1% voltage soft limits. Conversely, bus 12 is a PQ bus with one of the highest connected load, and hence the voltage does not reach to its nominal value. This reduces the total system load by 28.368 kW and increases the RES curtailment. In Figure D.4 in Appendix D, the total RES power utilized in the system is reduced by 0.10%, due to decrease in the total system load. Hence, this leads to an overall increase in cost by 0.227% compared to the scenario with 0.8 power factor and ±1% voltage soft limits. The BESS SOC and power graphs are given in Figure D.5 in Appendix D.

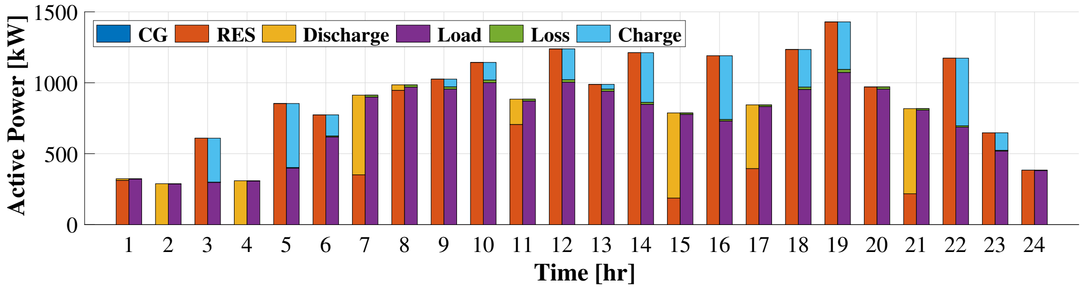

(a) Active Power

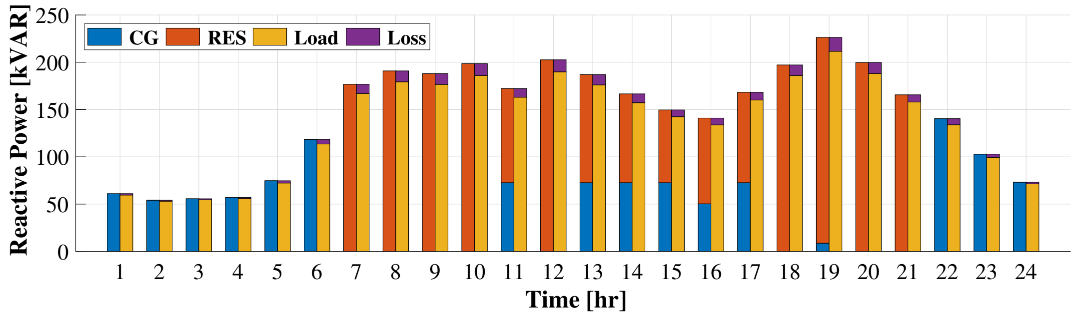

(b) Reactive Power

Figure 5.14: Power balance for case 2 with non-linear loads.

Finally, the bus angles are shown in Figure D.6 in Appendix D that has a small phase shift but are close to 0 deg.

5.2.4 Discussion

In sections 5.2.1-5.2.3, the results of the various scenarios simulated are described in detail. The optimized droop coefficients for all scenarios are given in Table D.1 in Appendix D. A summary of the results is also given in Table 5.2. As shown in the table, the increase in voltage soft limit resulted in a decrease in cost but an increase in RES utilization, despite the load being the same. The plausible reason for this is the difference in BESS charging and discharging pattern, and the remaining excess power is seen as an increase in system loss. A similar outcome is observed while comparing the scenarios in sections 5.2.2 and 5.2.1 with 1% soft limits. The BESS utilization is also compared numerically in section 5.2.2 which supports the above statement.

Table 5.2: Summary of results for case 2: cost minimization with RES curtailment.

Scenario	**Time [hr]**	**Iterations**	**Cost [$]**	**System Loss**		**RES Active Power Used [%]**
				[kW]	**kVAR**	
1% Voltage	16.08	36	682575.29	259.22	176.19	55.98
2% Voltage	7.63	14	682150.38	267.72	181.24	56.01
0.9 Power Factor	7.4	16	682324.43	264.24	178.65	56.00
Non-Linear Load	5.94	13	684126.74	256.56	174.17	55.88

In section 5.2.3, as the system load decreases, both the RES curtailment and cost increases. This load reduction occurs due to the presence of non-linear voltage-dependent loads present in the system. However, due to this decrease in RES power utilization, the system losses also decreases.

5.3 Case 3: Load Shedding

Load shedding is employed when the system load exceeds the available generation. It is particularly useful when the available RES power is not sufficient to balance the load demand. If the penalty associated with shedding the load is smaller than the operating cost of CGs, load shedding is expected to lead to a reduction in CG usage and hence, an overall reduction in cost. In this study, the penalty factor for load shedding, i.e., VOLL, is assumed to be 0.1 $\$/kW$. Moreover, since the load needs to be higher than the generation for load shedding to work, the load was increased by a factor of 7.

The load on bus 12 is used for load shedding, which is a PQ bus and one of the highest loads in the system as also given in Table B.3 in Appendix B. The maximum load that may be shed is assumed to be 20% of the load demand at that particular hour. The optimization variables for this case remain the same as those described in 5.2, with the inclusion of amount of load shed. It may be noted that this case does not include a cost for RES curtailment.

The optimization problem is therefore formulated as follows,

$$
\begin{aligned}
&\min_{x} \sum_{t=1}^{T_H}\sum_{g=1}^{N_G} \left(a_g P_g^2(t) + b_g P_g(t) + c_g\right) + \sum_{t=1}^{T_H}\sum_{l=1}^{N_L} VOLL \cdot P_l(t) \\
&\qquad \textit{where, } x = \{K_n^p,\ K_n^q,\ \Delta SOC(t),\ P_l,\ P_{CG},\ Q_{CG},\ V_{PV} \textit{ and } V_{HCPQ}\} \\
&\textit{subject to, } P_{BESS}(t) + E \cdot \Delta SOC(t) = 0 \\
&\qquad\qquad P_{g,\ RES}^{min} - P_{g,\ RES}(t) \leq 0 \\
&\qquad\qquad P_{g,\ RES}(t) - P_{g,\ RES}^{max} \leq 0 \\
&\qquad\qquad Q_{g,\ RES}^{min} - Q_{g,\ RES}(t) \leq 0 \\
&\qquad\qquad Q_{g,\ RES}(t) - Q_{g,\ RES}^{max} \leq 0 \\
&\qquad\qquad K_n^{q\ min} - K_n^q \leq 0 \\
&\qquad\qquad K_n^q - K_n^{q\ max} \leq 0 \\
&\qquad\qquad K_n^{p\ min} - K_n^p \leq 0 \\
&\qquad\qquad K_n^p - K_n^{p\ max} \leq 0 \\
&\qquad\qquad \frac{P_{BESS(d)}}{-E} - \Delta SOC(t) \leq 0 \\
&\qquad\qquad \Delta SOC(t) - \frac{P_{BESS(c)}}{-E} \leq 0 \\
&\qquad\qquad SOC(t) - SOC^{max} \leq 0 \\
&\qquad\qquad SOC^{min} - SOC(t) \leq 0 \\
&\qquad\qquad V_{PV,\ HCPQ} - V_{PV,\ HCPQ}^{max} \leq 0 \\
&\qquad\qquad V_{PV,\ HCPQ}^{min} - V_{PV,\ HCPQ} \leq 0 \\
&\qquad\qquad P_l - P_{LS}^{max} \leq 0 \\
&\qquad\qquad -P_l \leq 0
\end{aligned} \tag{5.5}
$$

On simulating the cost minimization objective with load shedding constraints (5.5) in MATLAB with $\pm 1\%$ voltage soft limits and 0.1 $\$/kW$ VOLL, the following results were obtained. The simulation lasted 6.13 hours and converged to a cost of \$ 4826.90 in 12 iterations. The various results are shown in Figure 5.15 - 5.20.

Figure 5.15 and 5.16 clearly indicate that the bus voltages and phase angles are maintained well within their acceptable boundaries. In Figure 5.17, it can be seen that all of the allowable load is shed during most of the time horizon. Load shedding helps in minimizing the cost by decreasing the CG contribution. In the hours where there is no load shedding, all the active power comes from RES, which can be seen from Figure 5.18. Hence, cutting down on load during these hours would only increase the cost.

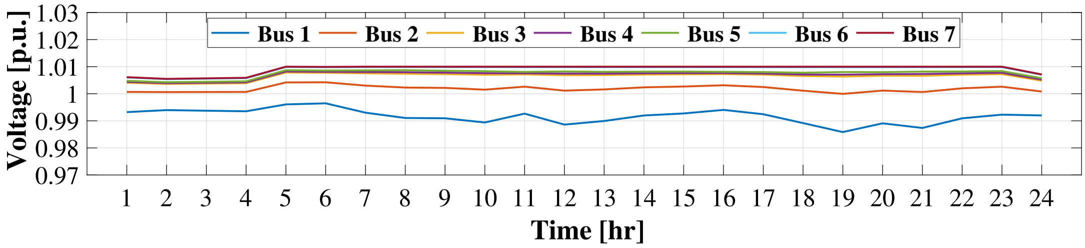

(a) Bus 1-7

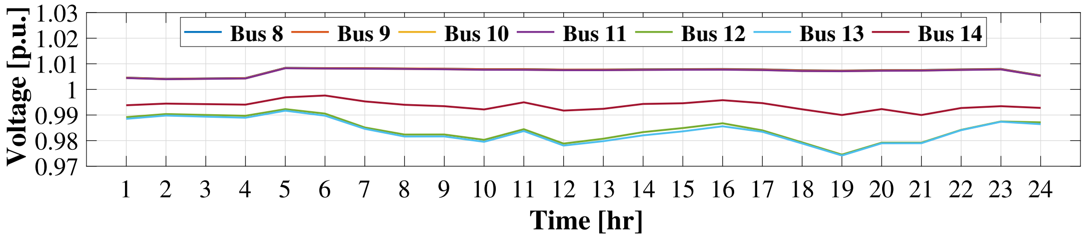

(b) Bus 8-14

Figure 5.15: Bus voltages for case 3.

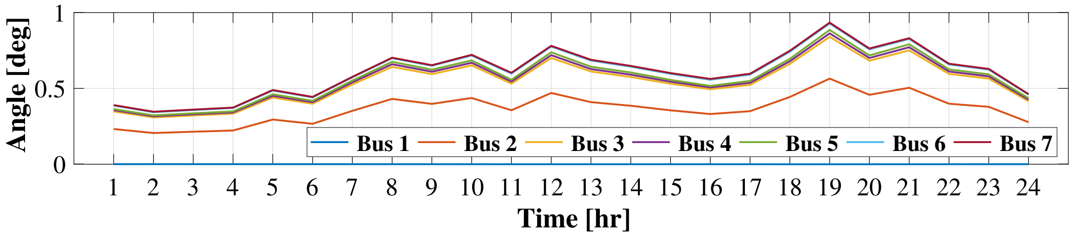

(a) Bus 1-7

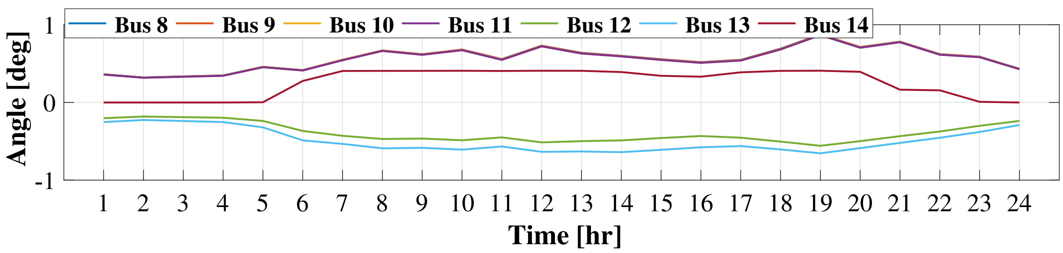

(b) Bus 8-14

Figure 5.16: Bus angles for case 3.

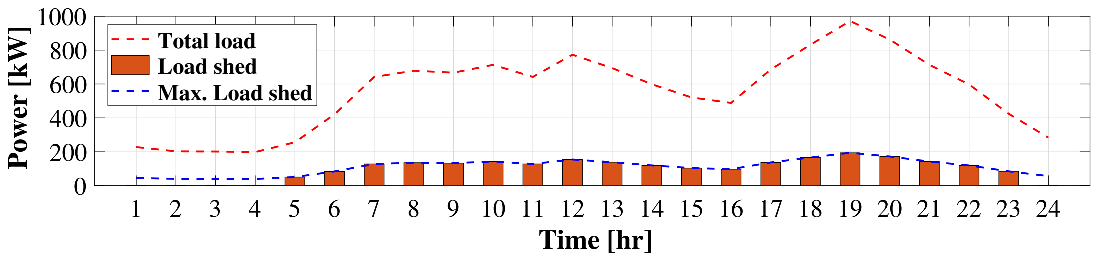

Figure 5.17: Load shedding for case 3.

The active and reactive power balance, and RES usage is given in Figure 5.18 and 5.19 respectively. The RES utilization was 83.76%. While the reactive power balance has no problems, from the active

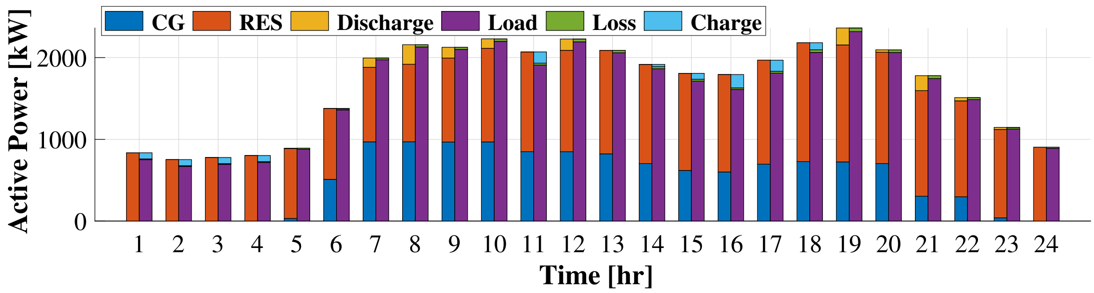

(a) Active Power

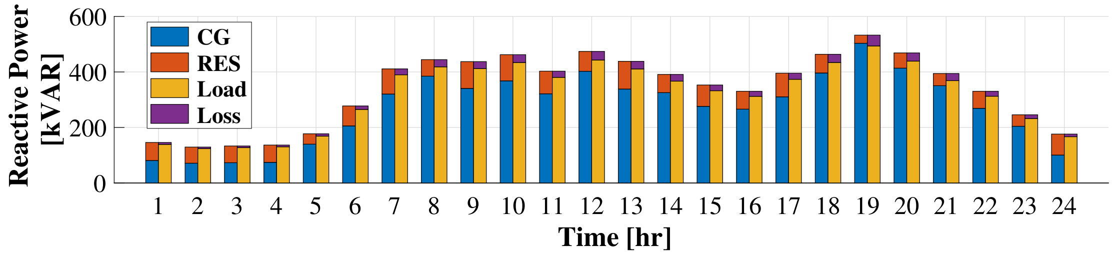

(b) Reactive Power

Figure 5.18: Power balance for case 3.

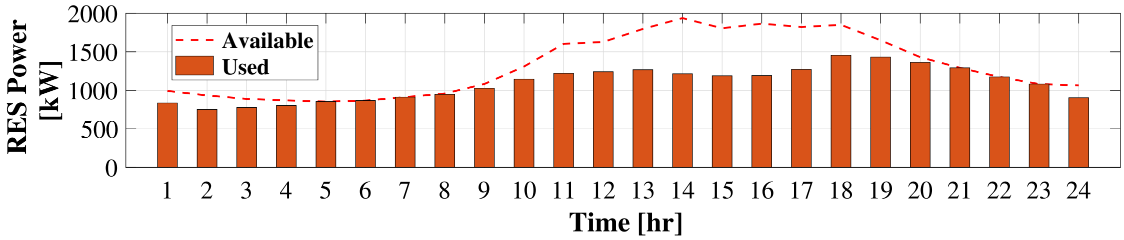

Figure 5.19: RES utilization for case 3.

power and RES utilization results it is evident that the cost could have been reduced by decreasing the CG contribution in many hours during the time horizon. However, this does not happen since the droop coefficients for a particular bus are the same over the entire time horizon. When a certain RES is required to give a large amount of power in one hour, in order to balance load, the active power droop coefficient K_n^p for that bus would need to be smaller, most likely close to the minimum value. This droop coefficient then gets fixed for the entire time horizon and would lead to that particular RES having a higher contribution in the other hours too. This, in turn, forces the other RES to not give large amounts of power and hence their droop coefficient values might be larger. Since the droop coefficient values are being forced in one hour, that affects the power in other hours, and hence causes an under-utilization of RES. This can be further validated from Table 5.3.

As seen from Table 5.3, the active power droop coefficient for the 7b, i.e., the 150 kW WT on bus 7 reaches close to its minimum limit of 2×10^{-7}, as defined in (5.2), causing the other buses to have a larger droop coefficient. It is also to be noted that the network has three identical 150 kW WTs on bus 7. In order to overcome this shortcoming of the algorithm, multiple droop coefficients could be

Table 5.3: Optimized droop coefficients for case 3.

Bus	K_n^p	K_n^q
3	1.1028e-4	1.6894e-3
4	1.1028-4	3.8220e-4
5	7.3555e-5	3.7382e-4
6	7.3555e-5	1.4536e-3
7a	1.6311e-4	4.9603e-6
7b	2.0268e-7	4.5265e-6
8	7.3555e-5	3.3787e-3
9	7.3555e-5	5.0000e-3
10	5.5137e-4	6.1575e-4
11	2.0268e-4	3.0822e-3

defined for a given bus. These different droop coefficients would be defined only for a specific time frame within the time horizon. This way, by dividing the time horizon into small time frames for the droop coefficients, the shortcomings of the algorithm may be overcome. Since the issue arises only in active power, the change can be done only in K_n^p while K_n^q can remain fixed as before. This is explored in the following sections.

Finally, the BESS action is shown in Figure 5.20. During the hour $t = 24$, the BESS SOC does not increase despite there being an excess amount of RES available. This is due to the fact the RES curtailment is not part of the objective and hence, there is no obligation to use the excess RES during that hour.

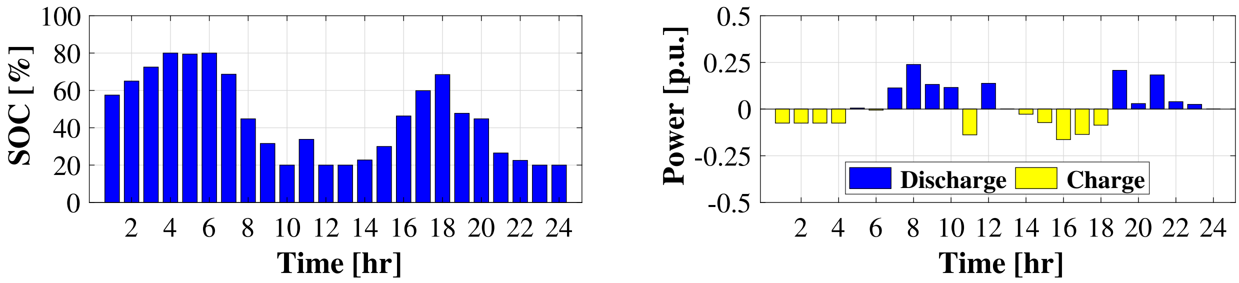

(a) SOC **(b)** BESS Power

Figure 5.20: BESS usage for case 3.

5.3.1 8 hr Droop Time Frame

In order to overcome the aforementioned drawbacks, the 24 hour time horizon is divided into 3 equal time frames of 8 hours each. A different active power droop coefficient K_n^p is defined for each time frame for each DG unit. On simulating with these modifications, the cost was optimized to \$ 4464.99, which is a reduction of 7.50% as compared to the earlier case without any droop time frame. The simulation lasted 22.99 hours with 44 iterations. Clearly, the increase in variables and hence complexity has an affect on the simulation time. However, since this is an offline study, the simulation time is not of as much importance as the cost. It is to be noted that in this simulation, and the simulations henceforth, the droop coefficients and cost were normalized so as to reduce the simulation time. The minimum cost corresponds to the cost incurred from the CG when they are on but not used, i.e. cost from the c coefficient only, and from load shedding when the simulation is performed with only load shedding as an objective. The maximum cost is the corresponding CG cost when the simulation is done with only load shedding as an objective, and when the entire permissible load is shed. The various relevant results are illustrated in Figure 5.21 - 5.22 below and the rest are given in Figure E.1-E.4 in Appendix E.

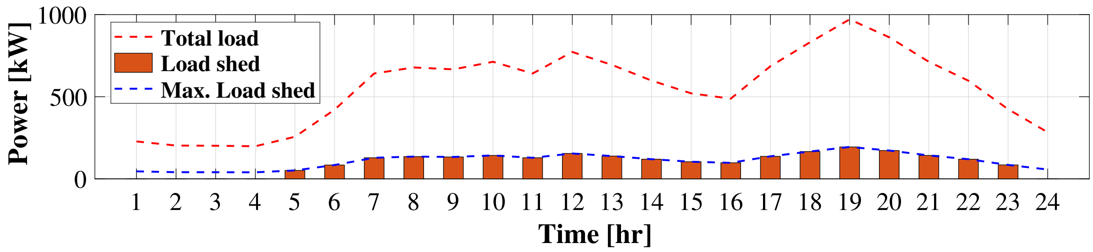

Figure 5.21: Load shedding for case 3 with 8-hour droop time frame.

As seen from Figure 5.21, the load shedding pattern is identical to the one observed in Figure 5.17. Load is not shed during the hours where CGs are not used whereas during the other hours the entire feasible load is shed. Figure 5.22 show the active power balance and RES utilization, which increases to 85.29% with the 8-hour droop time frame.

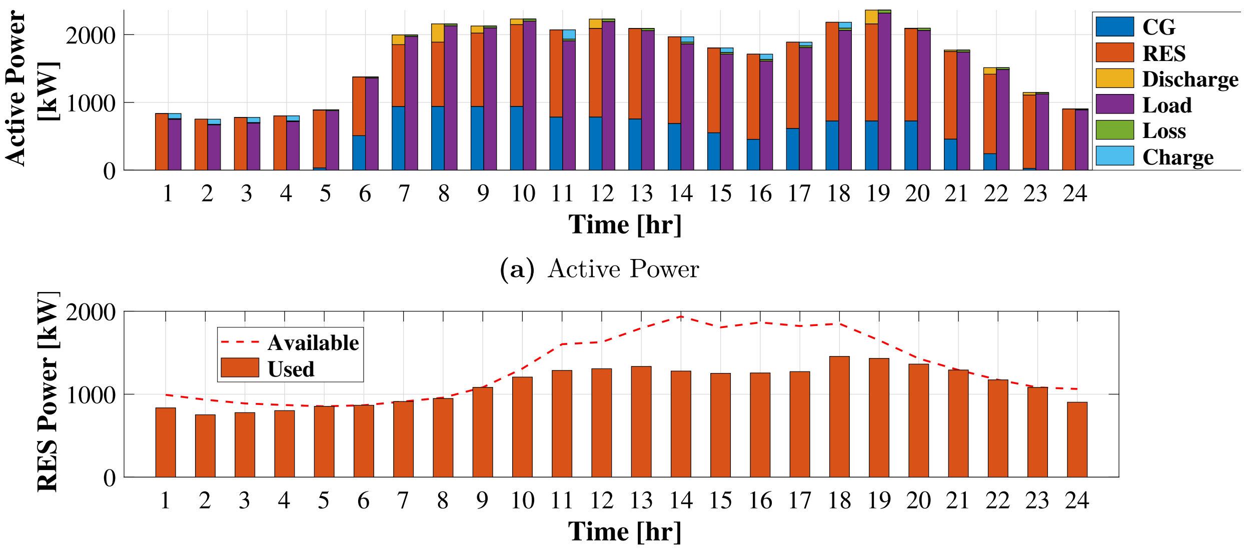

Figure 5.22: Active power balance and RES utilization for case 3 with 8-hour time frame.

This suggests that the modifications are still subject to the same drawbacks. During $t = 9$ to $t = 16$, 100% RES is being used during $t = 9$. During the third time frame, entire available RES is being used during the later hours of $t = 21,\ 22$, and 23. This causes the same problem that was discussed in the previous section. Thus, there is still scope for further RES utilization which could be achieved with a shorter droop time frame. The other results, namely, voltage, bus angles, reactive power balance, BESS usage, with the optimized droop coefficient are given in Figure E.1-E.4 and Table E.1 in Appendix E.

5.3.2 3-hr Droop Time Frame

The time horizon is divided into 8 smaller time frames of 3-hour duration each for the active power droop coefficient K_n^p. On simulating with these modifications, the cost was optimized to \$ 3726.29, a reduction of 22.80% as compared to the case with fixed droop time frame. The simulation lasted 62.13 hours and took 111 iterations.

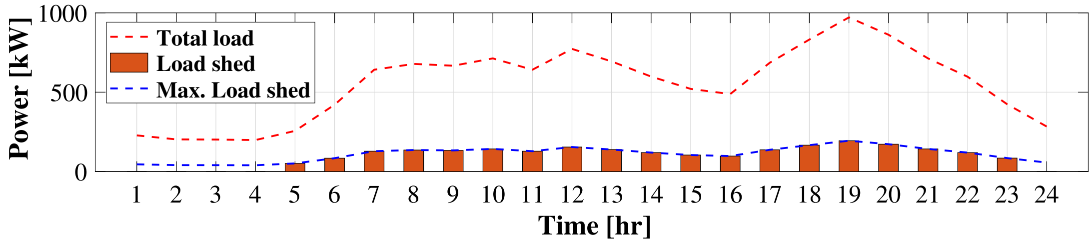

Figure 5.23: Load shedding for case 3 with 3-hour time frame.

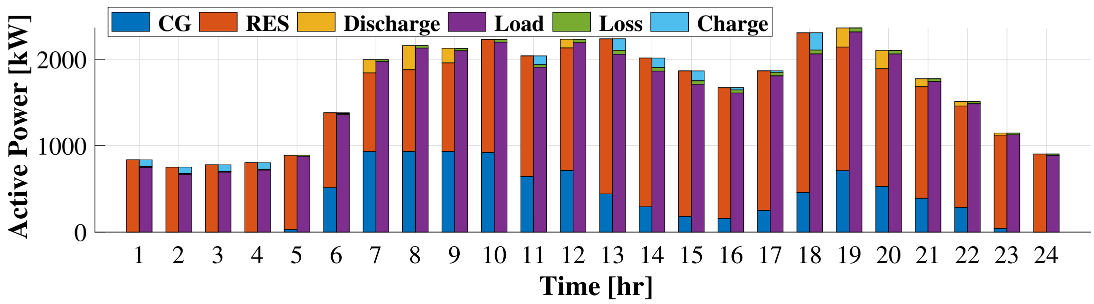

(a) Active Power

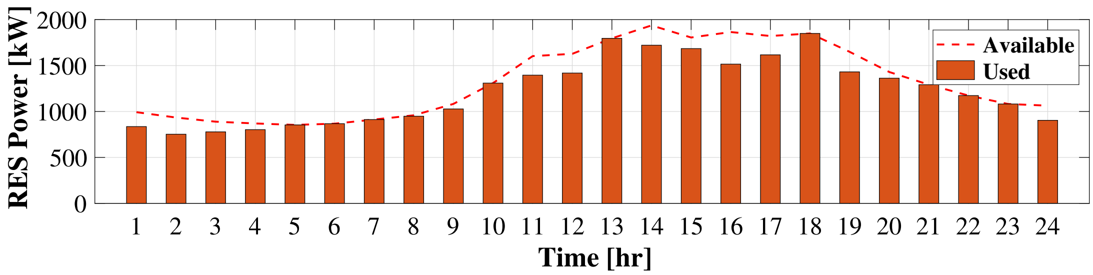

(b) RES Utilization

Figure 5.24: Active power balance and RES utilization for case 3 with 3-hour droop time frame.

Figure 5.23 shows the amount of load shed which looks exactly the same as the pattern seen in Figure 5.23 and 5.17. This suggests that the amount of load that can be shed by the system has remained the same despite the changes in droop time frame for active power droop coefficients and therefore, the contribution to cost from load shedding penalty is also constant. Thus, the decrease in cost is solely due to the decrease in CG active power contribution and consequently an increase in RES active power utilization to 93.57%. This can be clearly seen from Figure 5.24 which depicts the active power balance and RES active power utilization. The various other results for the 3-hour time frame simulation are given in Figure E.5-E.8 and Table E.2 in Appendix E.

5.3.3 1-hr Droop Time Frame

On dividing the time horizon further intro hourly time frames, the cost is optimized to $ 3409.30, a reduction of 29.36 % as compared to the case with fixed droop time frame. This simulation lasted 112.38 hours and took 262 iterations. It is also worth mentioning that this particular simulation was performed on a different system with processor AMD Ryzen 5 3600-5 Core CPU @ 3.59 GHz with 8 GB RAM. since the previous system that was being used since chapter 3 did not have sufficient computing power to run the simulation to its completion.

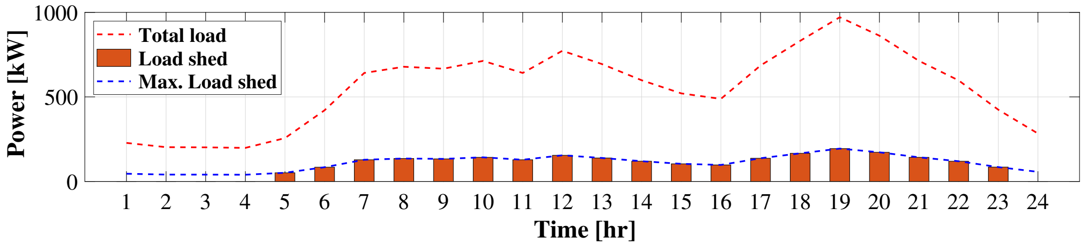

Figure 5.25: Load shedding for case 3 with 1-hour time frame.

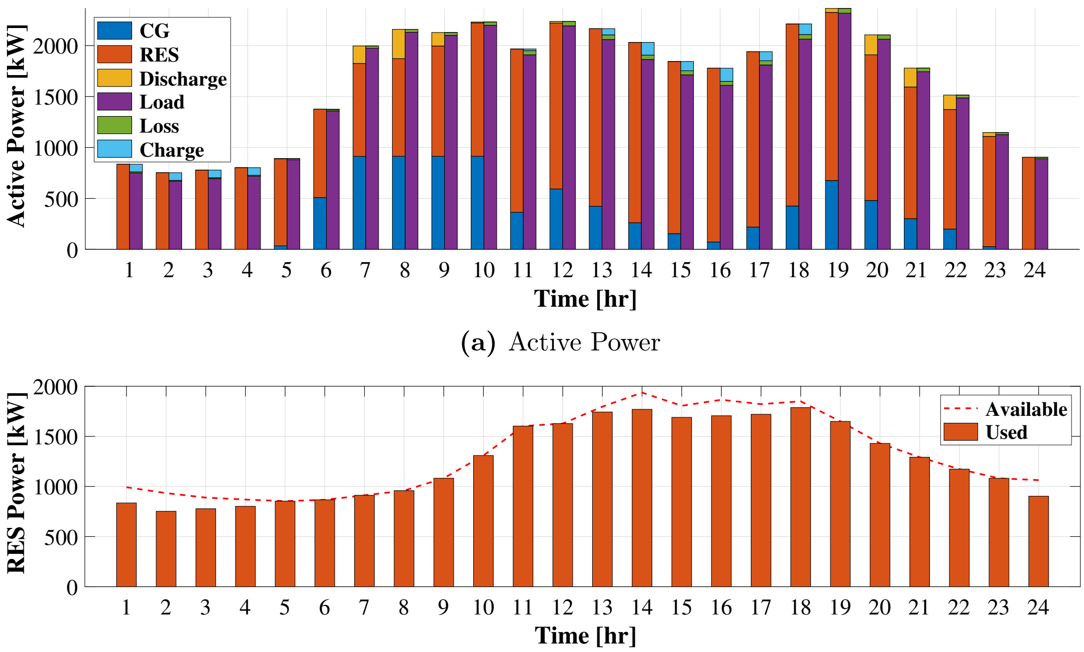

(a) Active Power

(b) RES Utilization

Figure 5.26: Active power balance and RES utilization for case 3 with 1-hour droop time frame.

As expected, the load shedding pattern remains the same in this scenario too, as seen from Figure 5.25.

Figure 5.26 however shows an anomaly. While the RES active power utilization increases to 96.72 %, it can be observed that during $t = 13$ to $t = 17$, there is a scope of increasing RES contribution towards power balance and thereby, decreasing cost. However, the optimization solver, SQP, is unable to produce this desired outcome. As mentioned in section 5.2, SQP is faster but the accuracy is compromised. Further investigation with different types of solvers and optimization algorithms is required to overcome this anomaly, which is out of the scope of this limited study.

The various other results for the 1-hour time frame simulation are given in Figure E.9-E.12 and Table E.3-E.4 in Appendix E.

5.3.4 Discussion

The various results obtained from the different droop time frames have been summarized in Table 5.4. Clearly, the decrease in droop time frame increases the active power contribution from RES and decreases cost. This, however, naturally comes with a trade off of an increase in computational complexity. Moreover, it is also noticed that the decrease in droop time frame leads to an increase in system loss, both active and reactive. This can also be attributed to line losses which increase due to the rise in RES power injection into the system. There is a noticeable voltage drop on the PQ buses as the droop time frame decreases. A larger voltage drop implies a larger current, which further implies an increase in losses in the system, given the line parameters.

Table 5.4: Summary of results for case 3: cost minimization with load shedding.

Droop Time Frame [hr]	Cost [$]	Iterations	RES Usage [%]	Time [hr]	System Loss	
					[kW]	[kVAR]
-	4826.90	12	83.76	6.13	549.95	476.27
8	4464.99	44	85.29	22.99	566.43	497.63
3	3726.29	111	93.57	62.13	666.63	544.70
1	3409.30	262	96.72	112.38	700.39	558.88

5.4 Summary

In this chapter, the proposed EOPF algorithm is validated on the modified MV CIGRE benchmark microgrid. The buses with solar are considered as PQ buses with no active and reactive power generation during the night and converted back to HCPQ buses during the day to make sure the algorithm runs correctly. After incorporating the results from the power flow study in chapter 4, two cases for cost minimization are explored, namely, RES curtailment and load shedding. In the RES curtailment case, scenarios with different voltage soft limits for the HCPQ and PV buses, and different power factors are explored. Additionally, voltage-dependent non-linear loads are also investigated. In the load shedding case, different scenarios with varying time frames for the active power droop coefficient are analysed. A shorter time frame mitigates the shortcoming of fixed droop coefficient values over the entire time horizon and further aids in minimizing the costs and allowing an increase in RES utilization.

The various results indicate an acceptable performance of the algorithm with the chosen solver. Features such as voltage soft limits and droop time frames allow for more flexibility in the system. Since the proposed EMS is for offline use only, the computational complexity of the simulations may be overlooked. Overall, the proposed EOPF algorithm is deemed good and may be used for calculating reference signals for the optimal control of a given microgrid.

6 Conclusion and Future Work

6.1 Conclusion

The ongoing energy transition has brought forth a multitude of technological and economical opportunities, to align with the environmental policies. One such example is the advancement of microgrids with DG units, specifically RES, and ESS. The potential solutions, however, bring with them their own challenges and hence, research opportunities. These include, but are not limited to, the need for a comprehensive communication network, accurate modelling of the system, and optimal control of components.

This study has proposed a tertiary level EMS to find optimal solutions for the control of AC islanded microgrids. This has been achieved by using an HC scheme. Finding reference set points to operate the DG units optimally requires an optimization process, subject to operational constraints. Whereas on the other hand, ensuring a tolerable bus voltage magnitude, power balance and system frequency require primary and secondary controls. An amalgamation of these three levels of control has lead to the proposed EMS in this study. The lower levels of controls are incorporated in the microgrid steady-state power flow using the HCPQ bus formulation, while the higher level takes care of the optimization goal and system constraints. The EMS is then validated on a benchmark MV CIGRE microgrid by simulating different cases.

In chapter 2, firstly, the state of art is described. The various concepts required to formulate the proposed EOPF algorithm are elaborated with descriptive examples. The chapter presents the significance of DER in a microgrid. Then, DSM and DR are described and the reason for choosing load shedding for this study is explained. Following that, the microgrid concept, along with its benefits and shortcomings is presented. Then in HC, primary, secondary, and tertiary controls are briefly explored with results obtained from Simulink on a test system. Later, primary and secondary controls are incorporated within power flow in MATLAB and the results are compared with the Simulink results from HC. Finally, economic dispatch is performed and various system constraints are modelled. A consolidated understanding of the various concepts in this chapter leads to the EOPF algorithm in chapter 3.

An EOPF algorithm promotes the given objective to be optimized with the inclusion of power flow to maintain optimal operating conditions in the system. The HCPQ bus power flow formulation was used in the EOPF algorithm as it regulates both bus voltage magnitude and frequency to their desired values. The proposed algorithm was used for various optimization objectives such as active power and reactive power sharing, cost minimization with BESS, and cost minimization with load shedding. From the case studies, it was observed that the inclusion of BESS reduces the system cost by discharging the stored RES power and minimizes the power usage from costly DGs. Moreover, encompassing load shedding in the objective function further decreases the cost but increases the system operation complexity. Load shedding happens when the penalty factor associated with load shed i.e. VOLL is lesser than operating cost of CG units. To further validate the proposed hierarchical scheme, a power flow analysis was performed on the modified MV CIGRE benchmark system in chapter 4.

Initially, the basic outline of a modified MV CIGRE benchmark system was discussed. Then, the system was examined by performing conventional power flow analysis with two sub-cases: 100% and 50% of maximum available generation capacity. From the simulation results, it was observed that the voltage magnitude exceeds +5% limit for buses 3-11 (connected with RES) when the generation capacity is 100%. On reducing generation capacity to 50% case, the voltage magnitude of buses 3-11 drops to +3%. For both cases, the bus angles shows minimum deviation from zero degrees. The decrease in DG capacity reduced the absorption of power by the assumed slack bus, however, a significant amount or active and reactive power was still absorbed. With these inference, buses 3-11 were selected as HCPQ buses for controlled power flow and were simulated with 10% of CG capacity while the RES generated power based on their RES profile. The droop coefficients were calculated by using droop equations.

The controlled power flow fixes the voltage magnitude on buses 3-11 to 1 p.u. for the entire time horizon. The active power was fully balanced but the problem of excessive reactive power still persisted. Therefore, to overcome the reactive power issue in the system PV bus voltage was decreased to 0.995 p.u. to reduce the excess reactive power contribution by CG, and the reference voltage for HCPQ buses was increased to 1.005 p.u. Finally, it was inferred that by changing the reference voltages for PV and HCPQ buses a proper reactive power balance could be obtained. This brings in need of certain constraints such as voltage soft limits for PV and HCPQ buses, generation capacities for CGs with minimum and maximum limits, BESS for proper utilization of RES, and suitable droop coefficients, all of which are optimized by a tertiary control satisfying the required system objective.

In chapter 5, the proposed control algorithm for EOPF was simulated for minimizing the operating cost of CG with two different cases, namely RES curtailment and load shedding. The buses with SPV were made as PQ buses with null output during the night, and converted back to HCPQ during the day phase. In the RES curtailment case, different scenarios with different voltage soft limits, different power factors and also voltage-dependent non-linear loads were simulated to analyse the system behaviour. In load shedding case, different scenarios with varying time frames for the active power droop coefficients were explored for the purpose of utilizing the RES power effectively. This lead to a reduction in the power from the CGs, thereby minimizing the overall cost. The shorter droop time frame and voltage soft limits allow for more flexibility in the system and contribute in maintaining reliable system operation.

In this limited study, an offline EMS algorithm is proposed and validated on a benchmark system. Nevertheless, further research and work is required to address the various shortcomings and limitations. Altogether, the proposed algorithm gives credence results with the chosen optimization solver. In conclusion, the proposed offline scheme may be used to model and simulate islanded AC microgrids in order to find optimal solutions for their control.

6.2 Future Work

- Multiple microgrid operation: Formulation of a hierarchical control scheme for multi-microgrid system operation.
- Different optimization solvers: The proposed control algorithm can be verified and compared using various professional optimization tools such as GAMS and different heuristic optimization algorithms.
- Experimental validation: To validate the proposed hierarchical algorithm experimentally in a laboratory on a test system.
- Trends in energy market: Development of energy management schemes with inclusion of current trends in the energy market such as Electric Vehicles (EV), P2X technologies, etc.
- DR techniques: Other DR methods, such as load shifting, may be employed to evaluate the algorithm. Load shifting allows for more demand flexibility without compromising process continuity or quality of service to the end-users. However, other demand response methods such as load shifting would convert the optimization problem to mixed integer, making the problem more complex and requiring a different solver.

A | Appendix: Simulink Model

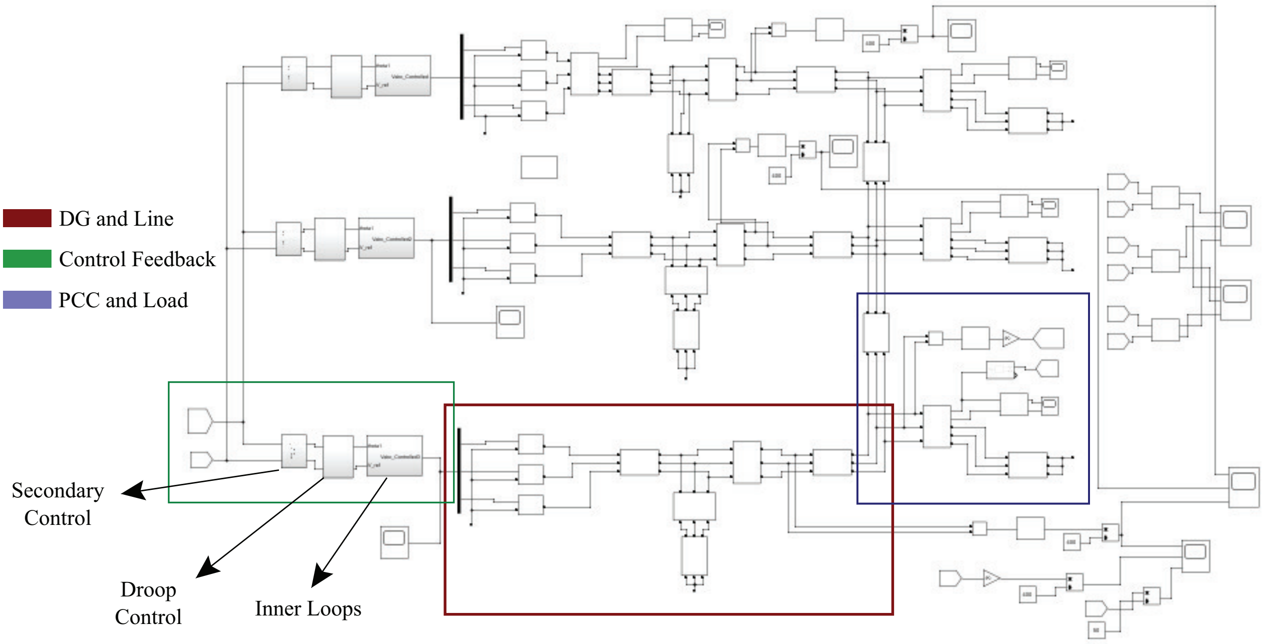

Figure A.1: Simulink model of 6-bus test system: Zoomed out.

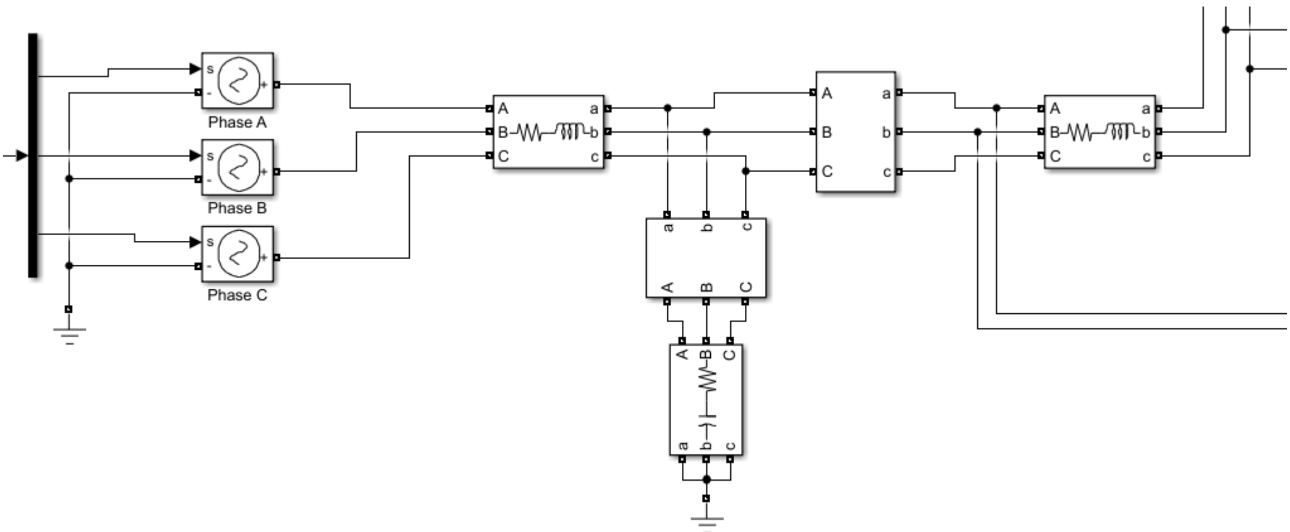

Figure A.2: Simulink model of 6-bus test system: DG and line.

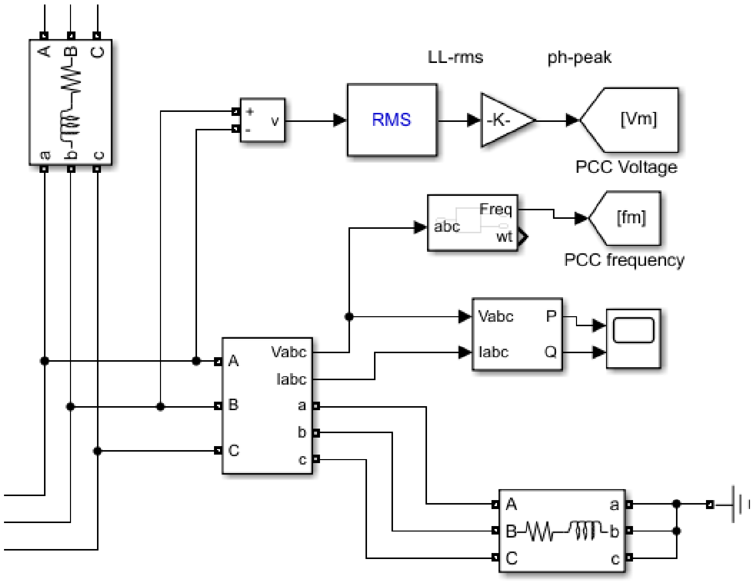

Figure A.3: Simulink model of 6-bus test system: PCC and Load.

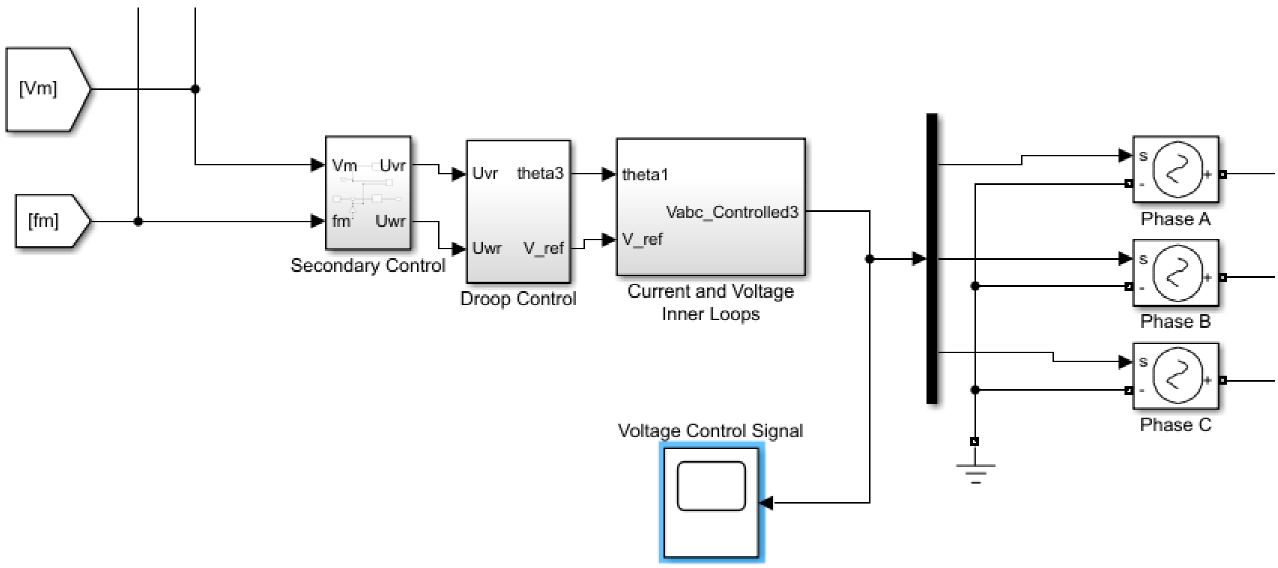

Figure A.4: Simulink model of 6-bus test system: Control Feedback.

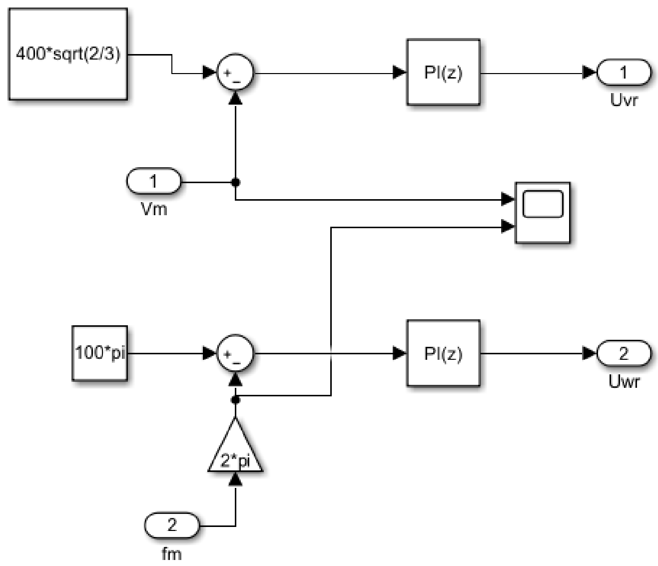

Figure A.5: Simulink model of 6-bus test system: Secondary Control.

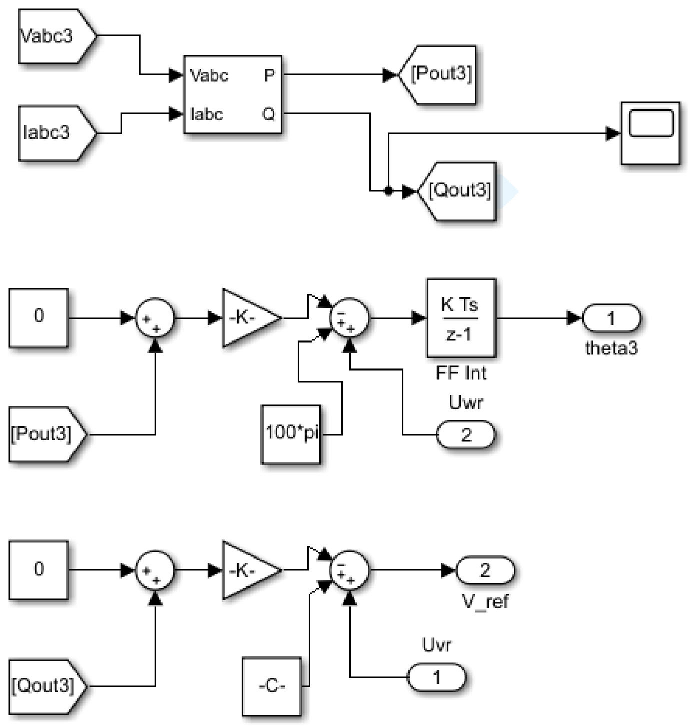

Figure A.6: Simulink model of 6-bus test system: Primary Droop Control.

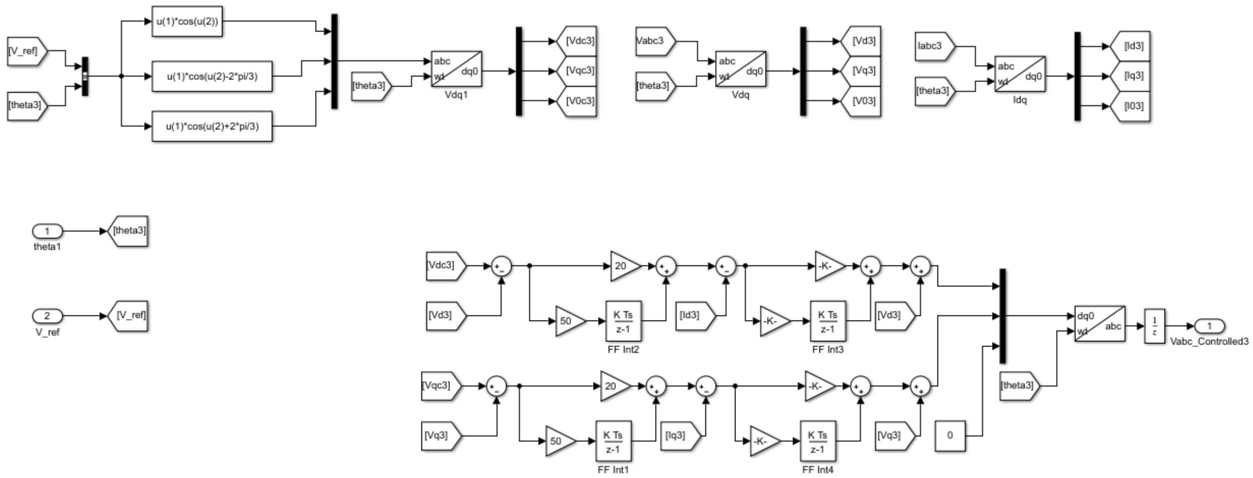

Figure A.7: Simulink model of 6-bus test system: Inner Voltage and Current Loops.

B | Appendix: CIGRE Microgrid Data

Table B.1: Line parameters [36, 35].

From Bus	To Bus	Length [km]	R [Ω/km]	X [Ω/km]
1	2	2.8	0.579	0.367
2	3	4.4	0.164	0.113
3	4	0.6	0.262	0.121
4	5	0.6	0.354	0.129
5	6	1.5	0.336	0.126
6	7	0.2	0.256	0.13
7	8	1.7	0.294	0.123
8	9	0.3	0.339	0.13
9	10	0.8	0.399	0.133
10	11	0.3	0.367	0.133
11	4	0.5	0.423	0.134
3	8	1.3	0.172	0.115
12	13	3	0.337	0.358
1	12	4.9	0.337	0.358

Table B.2: Transformer parameters [35].

From Bus	To Bus	X [p.u.]	V From [kV]	V To [kV]	Type	S_{rated} [kVA]
14	1	0.05	0.48	12.47	Δ-Y	5000

Table B.3: Load parameters at each bus [36].

Bus No.	Load type	P_{max} [p.u.]	Q_{max} [p.u.]	Power Factor
1	Household	0.15	0.031	0.9806
1	Industrial	0.05	0.01	0.9806
2	Household	0.00276	0.00069	0.9701
3	Industrial	0.00224	0.00139	0.8497
4	Household	0.00432	0.00108	0.9701
5	Household	0.00725	0.00182	0.9699
6	Household	0.0055	0.00138	0.9699
7	Industrial	0.00077	0.00048	0.8486
8	Household	0.00588	0.00147	0.9701
9	Industrial	0.00574	0.00356	0.8498
10	Household	0.00477	0.0012	0.9698
11	Household	0.00331	0.00083	0.9699
12	Household	0.15	0.03	0.9806
13	Industrial	0.05	0.0002	0.9999

Table B.4: DER capacity [35, 37].

Bus No.	**Type**	$\mathbf{P_{max}}$ **[kW]**
3	SPV	80
4	SPV	80
5	SPV	120
5	BESS	900
6	SPV	120
7	Wind	1000
7	Wind	150
7	Wind	150
7	Wind	150
8	SPV	120
9	SPV	120
9	CG	300
10	SPV	160
11	SPV	40
13	CG	300
14	CG	1400

Table B.5: Parameters for BESS for CIGRE grid [35, 37].

Parameter	**Value**	**Unit**
SOC_0	0.5	-
SOC^{min}	0.2	-
SOC^{max}	0.8	-
P_d^{min}	0	kW
P_d^{max}	900	kW
P_c^{min}	0	kW
P_c^{max}	900	kW
η_d	100	%
η_c	100	%
E	1000	kWh

Table B.6: Cost coefficients for CGs [35, 37].

CG Capacity [kW]	**a** $[\frac{\$}{kW^2}]$	**b** $[\frac{\$}{kW}]$	**c [$]**
300	0.0061	0.091	0.184
1400	0	0.2751	25.5

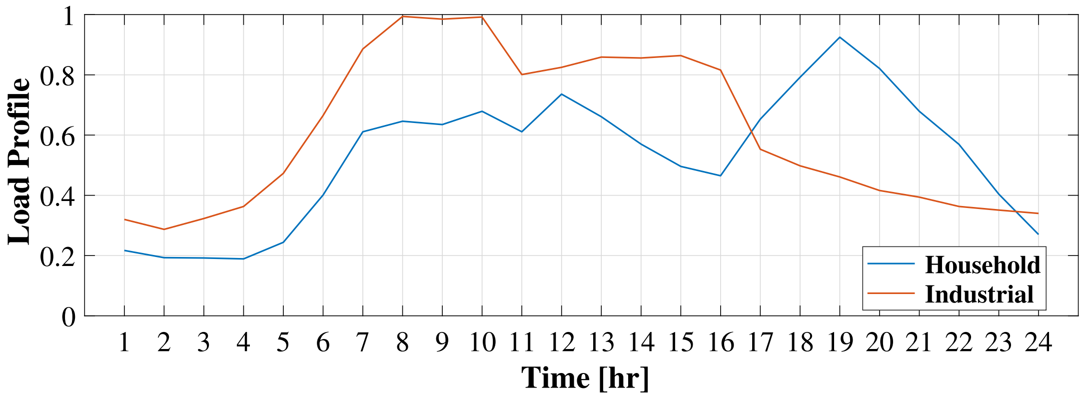

Figure B.1: Load profiles [36].

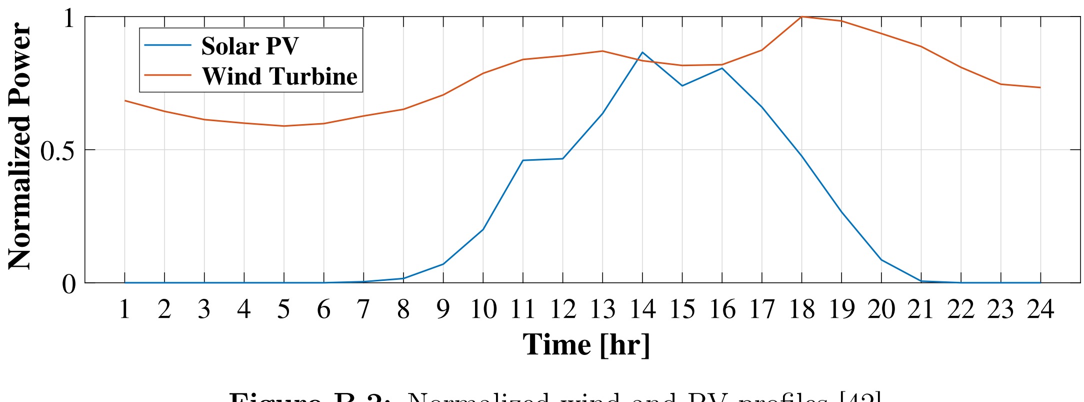

Figure B.2: Normalized wind and PV profiles [42].

C | Appendix: CIGRE Microgrid Power Flow

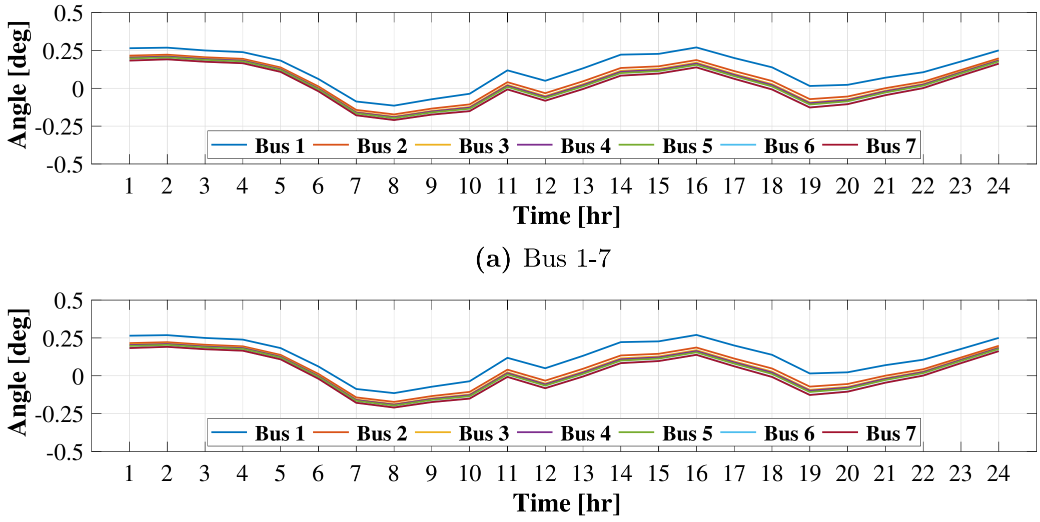

Figure C.1: Bus angles for case 0 with 50% DG capacity.

Table C.1: Droop coefficients for case 1.

Bus	**RES Capacity [kW]**	**kp** $[\frac{rad}{s\ kW}]$	**kq** $[\frac{kV}{kVAR}]$
3	80	3.9270e-5	2.0783e-2
4	80	3.9270e-5	2.0783e-2
5	120	2.6180e-5	1.3856e-2
6	120	2.6180e-5	1.3856e-2
7	1000	3.1416e-6	1.6627e-3
7	150	2.0944e-5	1.1084e-2
8	120	2.6180e-5	1.3856e-2
9	120	2.6180e-5	1.3856e-2
10	160	1.9635e-5	1.0392e-2
11	40	7.8540e-5	4.1567e-2

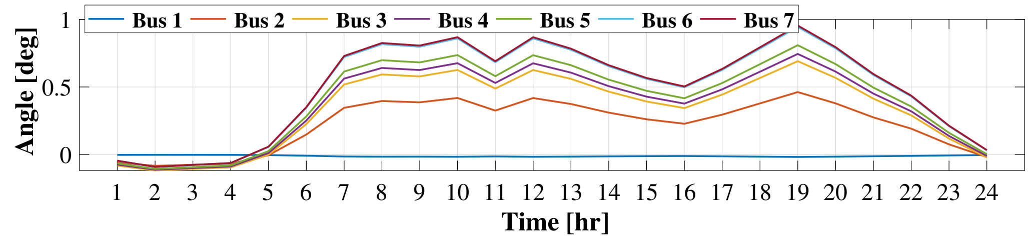

(a) Bus 1-7

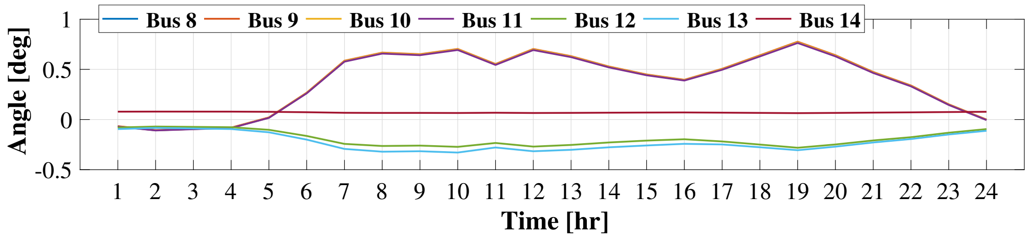

(b) Bus 8-14

Figure C.2: Bus angles for case 1 with PV bus voltage 0.995 p.u.

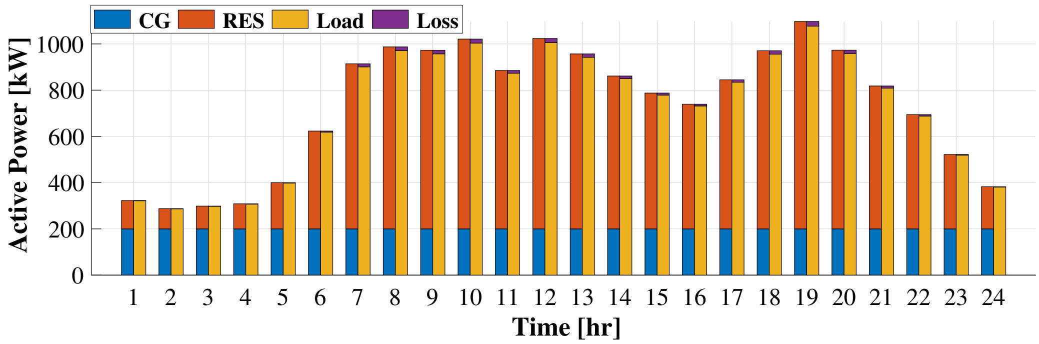

Figure C.3: Active power balance for case 1 with PV bus voltage 0.995 p.u.

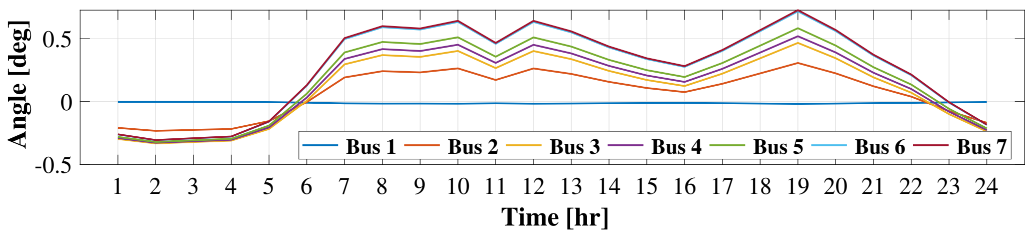

(a) Bus 1-7

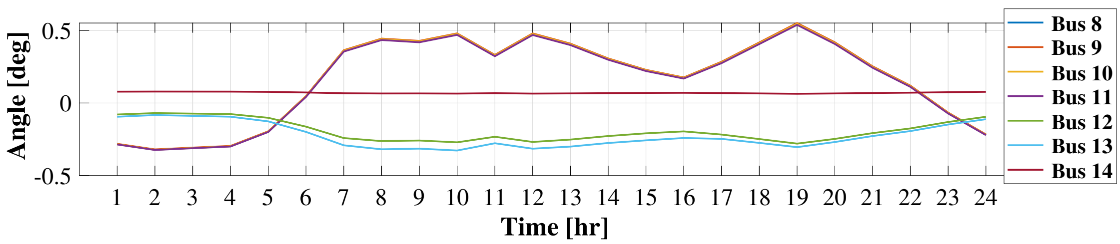

(b) Bus 8-14

Figure C.4: Bus angles for case 1 with PV bus voltage 0.995 p.u. and HCPQ bus voltage 1.005 p.u.

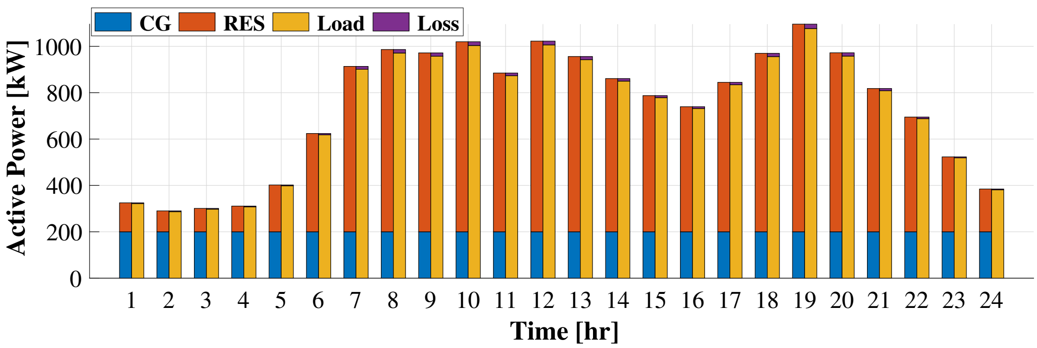

Figure C.5: Active power balance for case 1 with PV bus voltage 0.995 p.u. and HCPQ bus voltage 1.005 p.u.

D | Appendix: CIGRE Microgrid EOPF: RES Curtailment

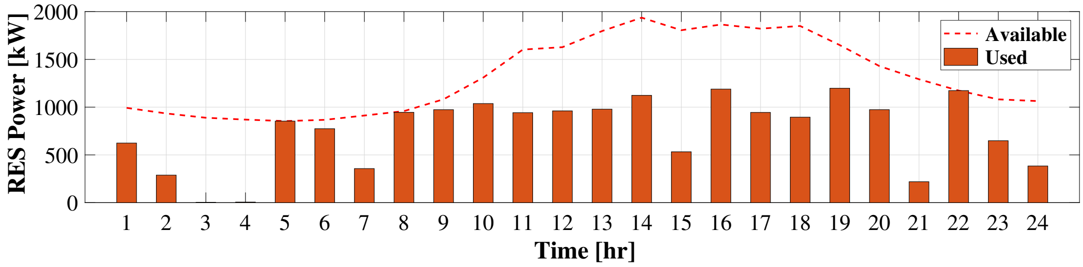

Figure D.1: RES curtailment for case 2 with 0.9 DG power factor.

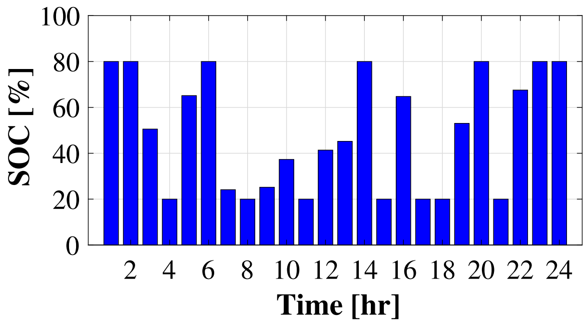

(a) SOC

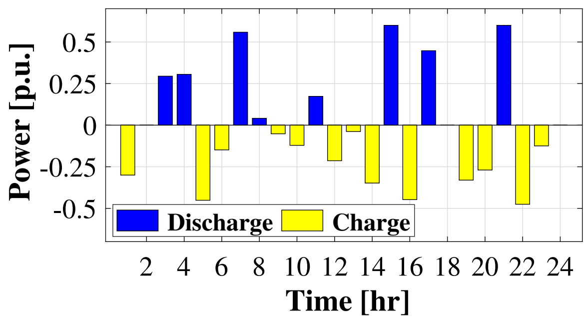

(b) BESS Power

Figure D.2: BESS usage for case 2 with 0.9 DG power factor.

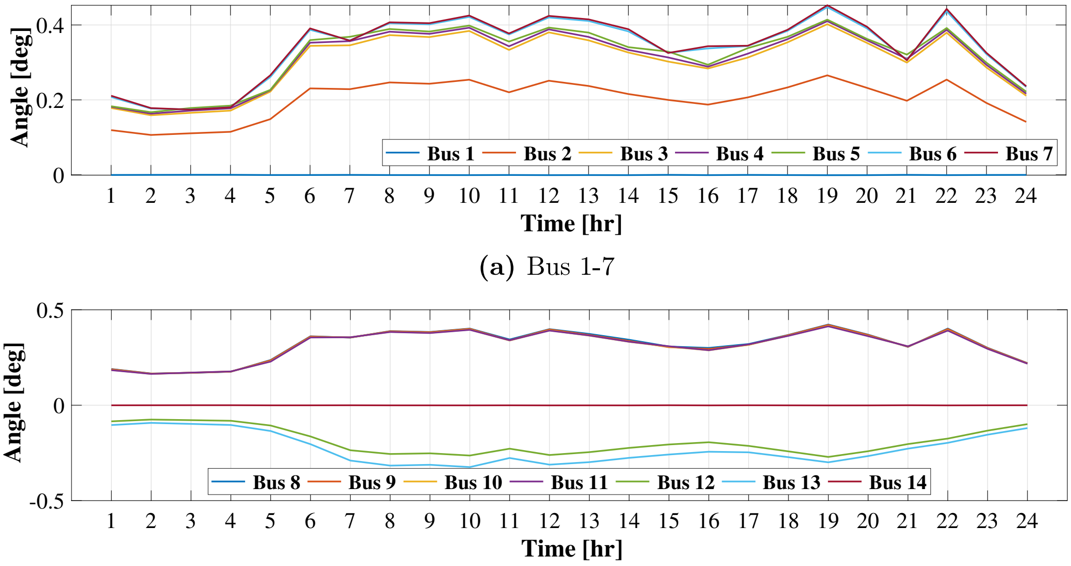

(a) Bus 1-7

(b) Bus 8-14

Figure D.3: Bus angles for case 2 with 0.9 DG power factor.

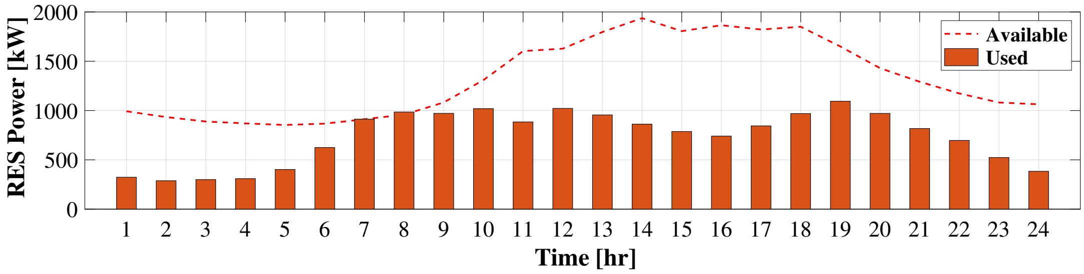

Figure D.4: RES curtailment for case 2 with non-linear loads.

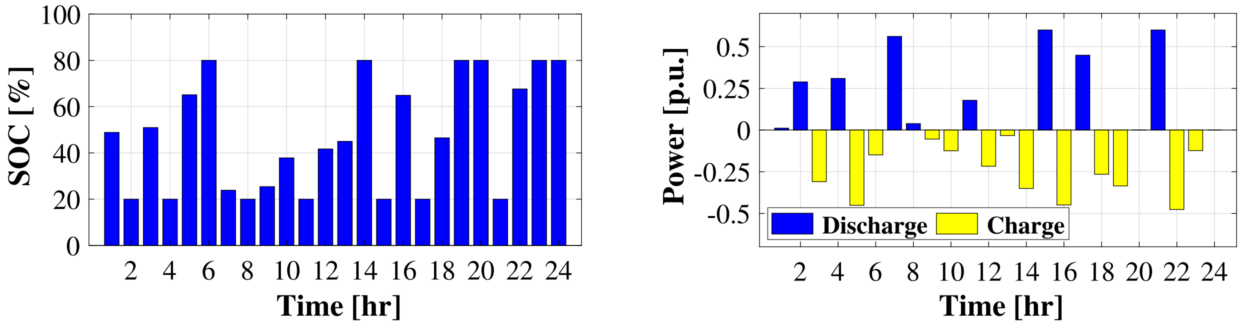

(a) SOC

(b) BESS Power

Figure D.5: BESS usage for case 2 with non-linear loads.

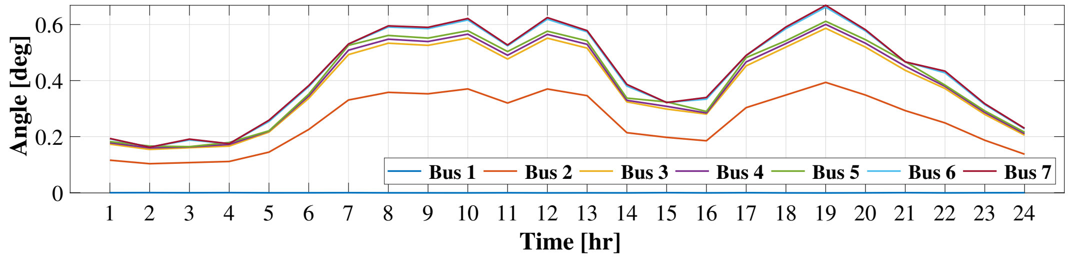

(a) Bus 1-7

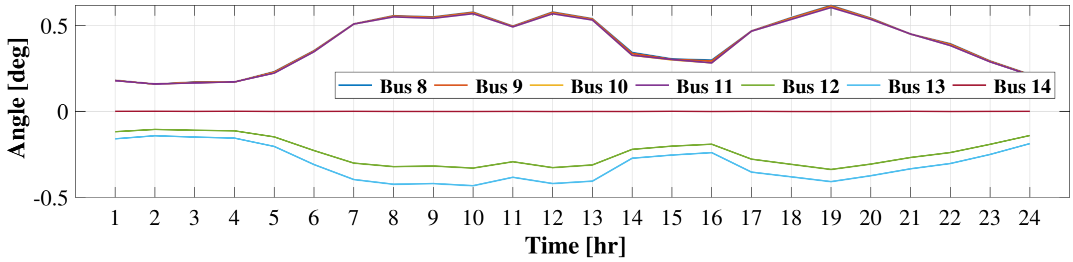

(b) Bus 8-14

Figure D.6: Bus angles for case 2 with non-linear loads.

Table D.1: Optimized droop coefficients for case 2.

	1% Voltage Limit		2% Voltage Limit	
Bus	K_n^p	K_n^q	K_n^p	K_n^q
3	5.0000e-4	4.7478e-3	5.0000e-4	5.0000e-3
4	5.0000e-4	3.7590e-3	5.0000e-4	2.0000e-6
5	4.3363e-4	1.9282e-3	5.0000e-4	5.0000e-3
6	3.3780e-5	1.5017e-3	3.7008e-5	1.7687e-3
7a	5.0622e-7	1.2593e-3	2.0000e-7	1.7687e-3
7b	5.1390e-7	1.2575e-3	2.0000e-7	2.0000e-6
8	4.6955e-4	7.0855e-6	5.0000e-4	1.0199e-3
9	4.7967e-4	1.3897e-3	5.0000e-4	2.4402e-3
10	5.0000e-4	4.9975e-3	5.0000e-4	4.4906e-3
11	5.0000e-4	5.0000e-3	5.0000e-4	4.2973e-3

	0.9 Power Factor		Non-Linear Loads	
Bus	K_n^p	K_n^q	K_n^p	K_n^q
3	5.0000e-4	5.0000e-3	5.0000e-4	1.3065e-3
4	5.0000e-4	5.0000e-3	5.0000e-4	5.0000e-3
5	5.0000e-4	2.3258e-3	5.0000e-4	5.0000e-3
6	3.7005e-5	5.0000e-3	3.6543e-5	2.0000e-6
7a	2.0000e-7	5.0000e-3	2.0000e-7	3.7302e-6
7b	2.0000e-7	2.0000e-6	2.0000e-7	2.0000e-6
8	5.0000e-4	1.3567e-3	5.0000e-4	2.0282e-3
9	5.0000e-4	8.8909e-4	5.0000e-4	5.0000e-3
10	5.0000e-4	2.0000e-6	5.0000e-4	2.0000e-6
11	5.0000e-4	5.0000e-3	5.0000e-4	3.5968e-3

E | Appendix: CIGRE Microgrid EOPF: Load Shedding

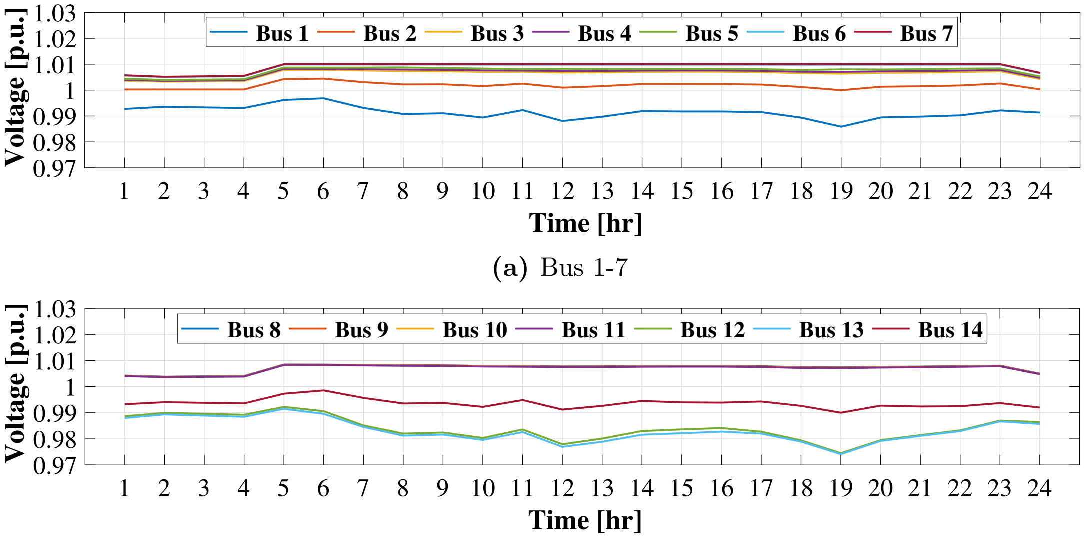

(a) Bus 1-7

(b) Bus 8-14

Figure E.1: Bus voltages for case 3 with 8-hour time frame.

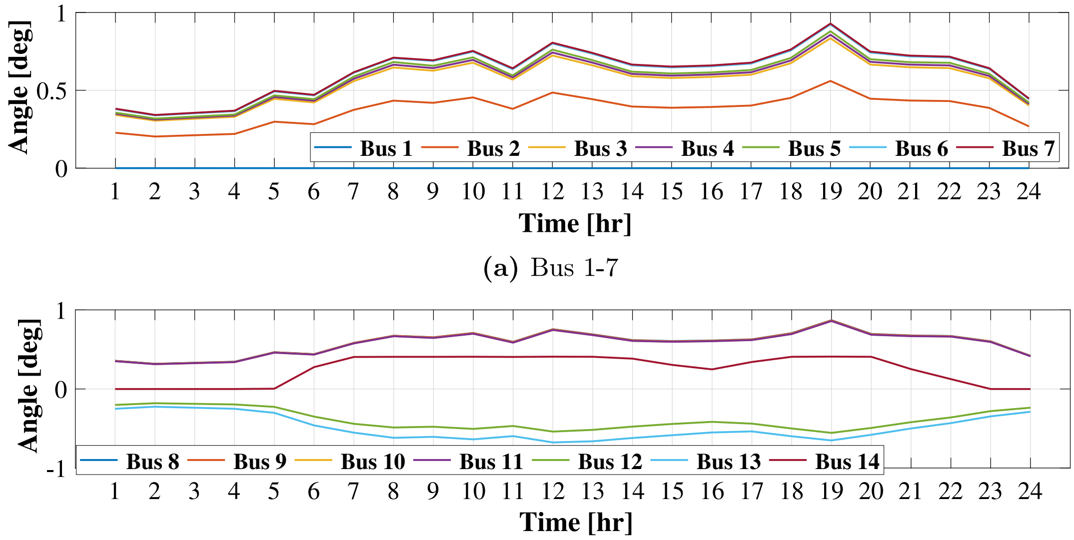

(a) Bus 1-7

(b) Bus 8-14

Figure E.2: Bus angles for case 3 with 8-hour time frame.

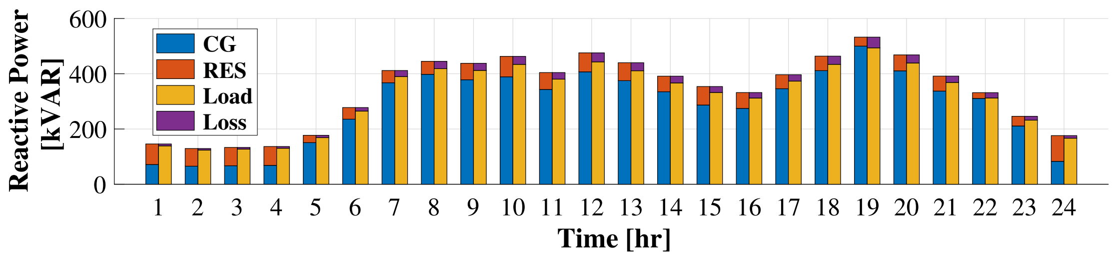

Figure E.3: Reactive power balance for case 3 with 8-hour time frame.

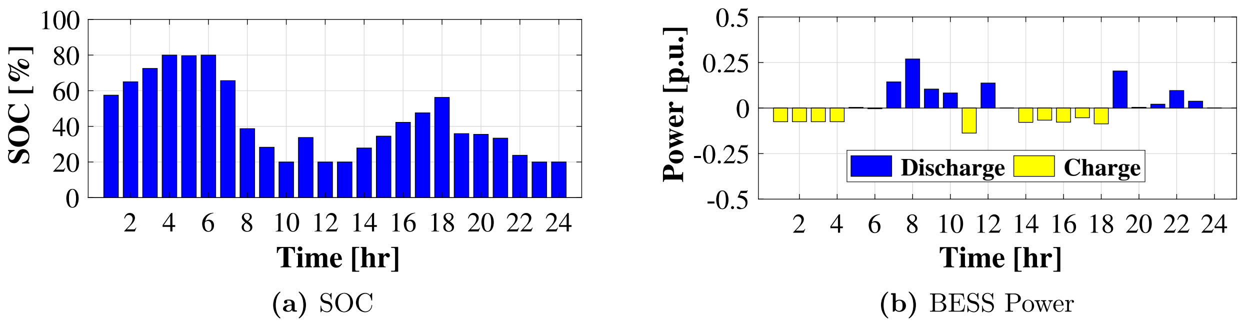

Figure E.4: BESS usage for case 3 with 8-hour time frame.

Table E.1: Optimized droop coefficients for case 3 with 8-hour droop time frame.

Bus	K_n^p			K_n^q
	t = 1 to 8	**t = 9 to 16**	**t = 17 to 24**	
3	2.5243e-4	2.4430e-5	2.2198e-4	9.9758e-5
4	2.5231e-4	2.4430e-5	2.2194e-4	9.9863e-5
5	1.8758e-4	1.6287e-5	1.7508e-4	9.9816e-5
6	1.8751e-4	1.6287e-5	1.7505e-4	9.9823e-5
7a	3.1435e-7	8.8202e-5	2.4381e-7	9.9961e-5
7b	3.5489e-7	4.0153e-7	2.9626e-7	1.0001e-4
8	1.8764e-4	1.6287e-5	1.7510e-4	1.0005e-4
9	1.8763e-4	1.6287e-5	1.7510e-4	1.0007e-4
10	1.597e-4	1.2215e-5	1.3456e-4	1.0002e-4
11	4.9182e-4	1.1097e-4	3.7746e-4	9.9987e-5

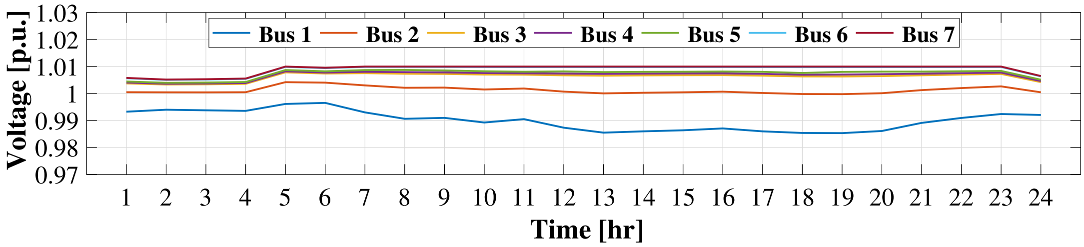

(a) Bus 1-7

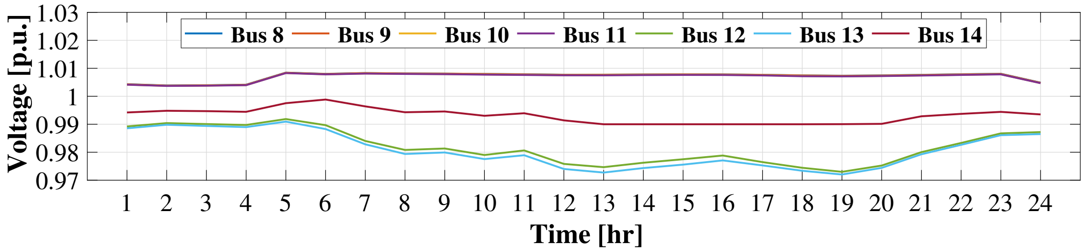

(b) Bus 8-14

Figure E.5: Bus voltages for case 3 with 3-hour time frame.

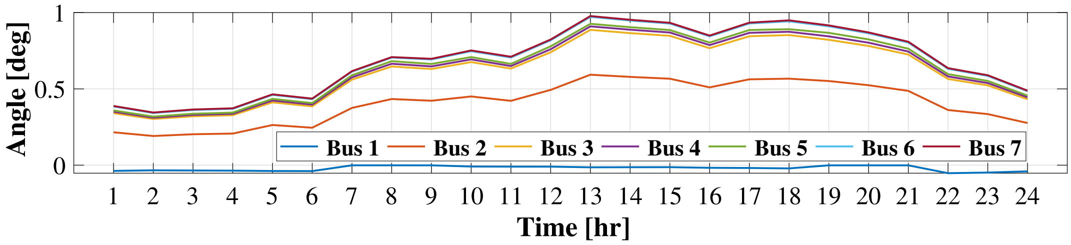

(a) Bus 1-7

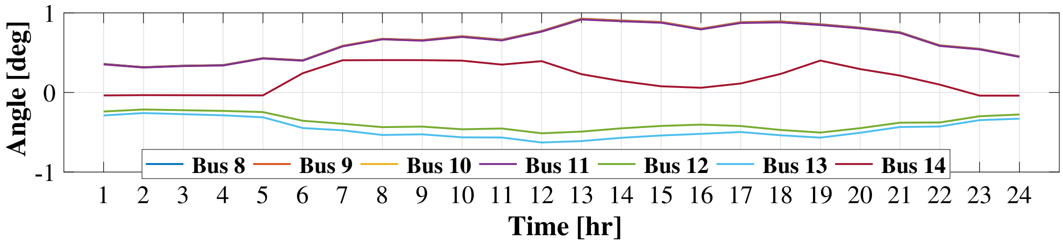

(b) Bus 8-14

Figure E.6: Bus angles for case 3 with 3-hour droop time frame.

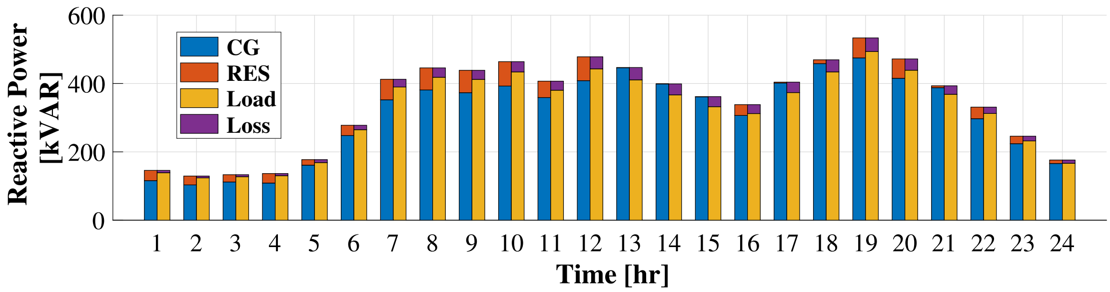

Figure E.7: Reactive power balance for case 3 with 3-hour droop time frame.

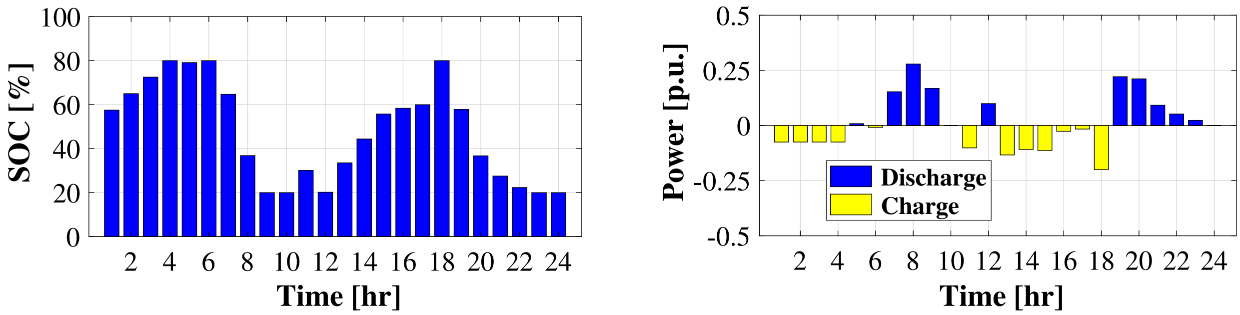

(a) SOC **(b)** BESS Power

Figure E.8: BESS usage for case 3 with 3-hour droop time frame.

Table E.2: Optimized droop coefficients for case 3 with 3-hour droop time frame.

Bus	K_n^p				K_n^q
	t = 1 to 3	**t = 4 to 6**	**t = 7 to 9**	**t = 10 to 12**	
3	-	1.2500e-5	1.9681e-4	3.8506e-5	9.9569e-5
4	-	1.2500e-5	1.9686e-4	3.8506e-5	9.9797e-5
5	-	1.2500e-5	1.3121e-4	2.5670e-5	9.9718e-5
6	-	1.2500e-5	1.3121e-4	2.5670e-5	9.9771e-5
7a	1.2500e-5	1.2507e-5	6.9319e-7	2.8182e-6	9.9943e-5
7b	1.2500e-5	1.2495e-5	2.3098e-7	2.0035e-6	1.0001e-4
8	-	1.2500e-5	1.3121e-4	2.5670e-5	1.0007e-4
9	-	1.2500e-5	1.3121e-4	2.5670e-5	1.0008e-4
10	-	1.2500e-5	9.8406e-5	1.9253e-5	9.9982e-4
11	-	1.2500e-5	4.2015e-4	7.7011e-5	1.0005e-5
	t = 13 to 15	**t = 16 to 18**	**t = 19 to 21**	**t = 22 to 24**	
3	1.9041e-5	3.8082e-5	1.6181e-4	-	
4	1.9041e-5	3.8082e-5	1.6182e-4	-	
5	1.2694e-5	2.5734e-5	1.1094e-4	-	
6	1.2694e-5	2.5734e-5	1.1097e-4	-	
7a	1.8093e-5	1.1823e-6	2.3330e-7	1.2500e-5	
7b	2.4043e-6	2.1331e-5	2.1107e-7	1.2500e-5	
8	1.2694e-5	2.5734e-5	1.1092e-4	-	
9	1.2694e-5	2.5734e-5	1.1092e-4	-	
10	9.5205e-6	1.9301e-5	7.5320e-5	-	
11	3.8082e-5	7.7203e-5	2.8984e-4	-	

Table E.3: Optimized reactive power droop coefficients for case 3 with 1-hour droop time frame.

Bus	K_n^q
3	1.0084e-04
4	9.9303e-05
5	1.0118e-04
6	9.9303e-05
7a	9.9303e-05
7b	9.9195e-05
8	1.0163e-04
9	9.9767e-05
10	9.9303e-05
11	9.9386e-05

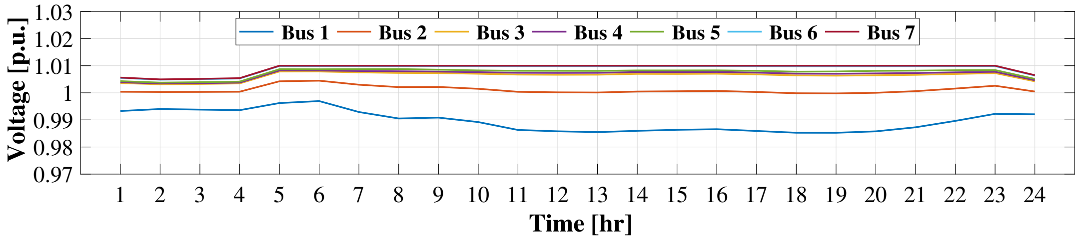

(a) Bus 1-7

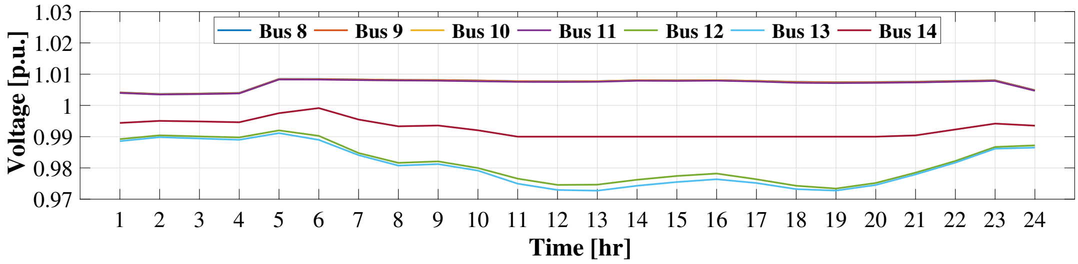

(b) Bus 8-14

Figure E.9: Bus voltages for case 3 with 1-hour time frame.

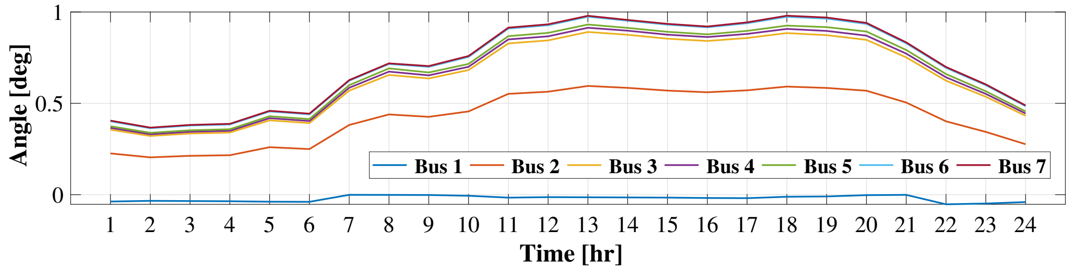

(a) Bus 1-7

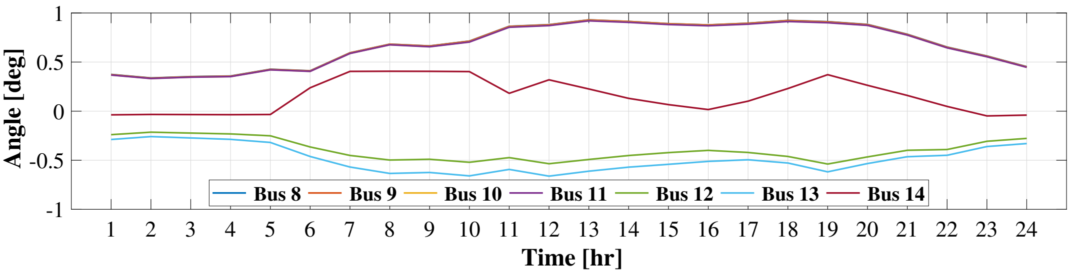

(b) Bus 8-14

Figure E.10: Bus angles for case 3 with 1-hour droop time frame.

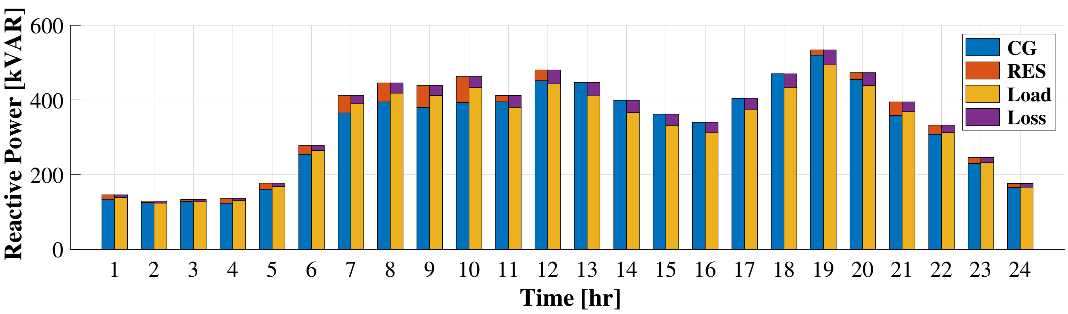

Figure E.11: Reactive power balance for case 3 with 1-hour droop time frame.

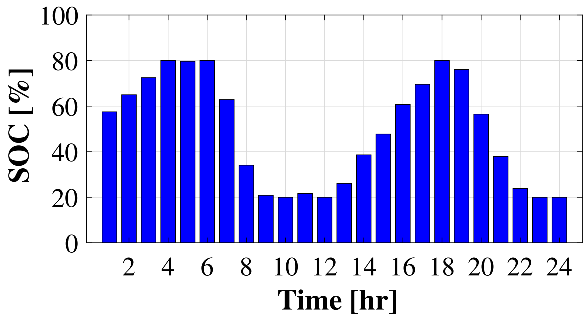

(a) SOC

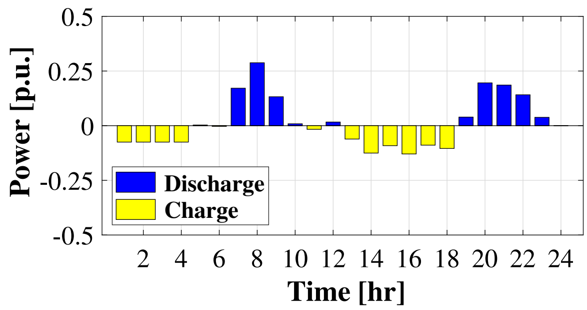

(b) BESS Power

Figure E.12: BESS usage for case 3 with 1-hour droop time frame.

Table E.4: Optimized active power droop coefficients for case 3 with 1-hour droop time frame.

Bus	**t=1**	**t=2**	**t=3**	**t=4**	**t=5**	**t=6**
3	-	-	-	-	-	-
4	-	-	-	-	-	-
5	-	-	-	-	-	-
6	-	-	-	-	-	-
7a	1.2500e-05	1.2500e-05	1.2500e-05	1.2500e-05	1.2551e-05	1.2539e-05
7b	1.2500e-05	1.2500e-05	1.2500e-05	1.2500e-05	1.2563e-05	1.2595e-05
8	-	-	-	-	-	-
9	-	-	-	-	-	-
10	-	-	-	-	-	-
11	-	-	-	-	-	-
	t=7	**t=8**	**t=9**	**t=10**	**t=11**	**t=12**
3	1.6648e-04	6.3408e-05	2.1901e-05	2.5603e-05	3.0498e-05	2.5125e-05
4	1.6648e-04	6.3408e-05	2.1901e-05	2.5603e-05	3.0498e-05	2.5125e-05
5	1.1099e-04	4.2272e-05	1.4601e-05	1.7069e-05	2.0333e-05	1.6750e-05
6	1.1099e-04	4.2272e-05	1.4601e-05	1.7069e-05	2.0333e-05	1.6750e-05
7a	4.7483e-07	5.0984e-07	5.6179e-06	5.6552e-07	2.5724e-06	1.4681e-06
7b	2.0061e-07	3.0992e-07	3.6725e-07	2.9487e-06	4.3154e-06	4.6954e-06
8	1.1099e-04	4.2272e-05	1.4599e-05	1.7068e-05	2.0333e-05	1.6750e-05
9	1.1099e-04	4.2272e-05	1.4601e-05	1.7069e-05	2.0333e-05	1.6750e-05
10	8.3240e-05	3.1704e-05	1.0950e-05	1.2801e-05	1.5249e-05	1.2562e-05
11	3.5580e-04	1.2682e-04	4.3802e-05	5.1199e-05	6.0998e-05	5.0249e-05
	t=13	**t=14**	**t=15**	**t=16**	**t=17**	**t=18**
3	1.9565e-05	1.5111e-05	1.8803e-05	1.9635e-05	2.5117e-05	2.0778e-05
4	1.9565e-05	1.5111e-05	1.8803e-05	1.9635e-05	2.5117e-05	2.0778e-05
5	1.3043e-05	1.0074e-05	1.2535e-05	1.3090e-05	1.6745e-05	1.3852e-05
6	1.3043e-05	1.0074e-05	1.2535e-05	1.3090e-05	1.6745e-05	1.3852e-05
7a	1.4334e-05	9.5514e-06	1.5859e-05	1.2405e-05	3.4261e-05	6.3677e-07
7b	2.6210e-06	3.3665e-06	3.3456e-06	4.0977e-06	3.5289e-06	1.6372e-05
8	1.3043e-05	1.0074e-05	1.2535e-05	1.3090e-05	1.6745e-05	1.3852e-05
9	1.3043e-05	1.0074e-05	1.2535e-05	1.3090e-05	1.6745e-05	1.3852e-05
10	9.7826e-06	7.5555e-06	9.4016e-06	9.8174e-06	1.2558e-05	1.0389e-05
11	3.9130e-05	3.0222e-05	3.7606e-05	3.9270e-05	5.0234e-05	4.1555e-05
	t=19	**t=20**	**t=21**	**t=22**	**t=23**	**t=24**
3	3.1520e-05	2.5298e-05	1.4360e-04	-	-	-
4	3.1520e-05	2.5298e-05	1.4360e-04	-	-	-
5	2.1014e-05	1.6865e-05	9.5734e-05	-	-	-
6	2.1015e-05	1.6865e-05	9.5948e-05	-	-	-
7a	4.9815e-07	2.2623e-06	2.6931e-07	1.2514e-05	1.2497e-05	1.2500e-05
7b	2.5263e-05	4.0766e-07	2.0055e-07	1.2525e-05	1.2507e-05	1.2500e-05
8	2.1014e-05	1.6865e-05	9.5757e-05	-	-	-
9	2.1014e-05	1.6865e-05	9.5760e-05	-	-	-
10	1.5761e-05	1.2649e-05	7.1886e-05	-	-	-
11	6.3038e-05	5.0596e-05	3.0826e-04	-	-	-

F | Appendix: MATLAB Code

F.1 Data File

```
basekVA = 1000; %system base in kVA
g = 24; % variable for time horizon

pf = 0.8; %power factor for CG reactive power calculation

% normalized RES power
Pwind=[0.6845,0.6441,0.6131,0.5997,0.5889,0.5980,0.6268,0.6517,0.7060,0.7870,0.8390,0.8527,
        0.8706,0.8343,0.8165,0.8194,0.8741,1.0,0.9836,0.9364,0.8876,0.8093,0.7459,0.7335];
PPV=[0,0,0,0,0,0,0.004,0.016,0.07,0.2,0.46,0.466,0.636,0.866,0.74,0.806,0.66,0.476,0.266,0.086,0.006,0,0,0];

% RES hourly generation profile for each bus

Generation = zeros(14,2,24);

RES_MAX =    [0;
              0;
              80;
              80;
              120;
              120;
              (1000+150+150+150);
              120;
              120;
              160;
              40;
              0;
              0;
              0];

RESprofile = [zeros(1,24);
              zeros(1,24);
              PPV;
              PPV;
              PPV;
              PPV;
              Pwind;
              PPV;
              PPV;
              PPV;
              PPV;
              zeros(1,24);
```

```
               zeros(1,24);
               zeros(1,24)];


Generation(:,1,:) = RES_MAX.*RESprofile./(basekVA);
Generation(:,2,:) = Generation(:,1,:).*(sqrt(1 - pf^2)/pf);


% for CG upper bound
gen = [300;1400;300]./basekVA./2; % bus 13, 14, 9
gen(:,2) = gen(:,1).*(sqrt(1 - pf^2)/pf);

%% BESS
E = -1000/basekVA; %BESS Capacity [kWh]
Pbess_min = +900/basekVA; %charge [kW]
Pbess_max = -900/basekVA; %discharge [kW]

soc_max = 0.8;
soc_min = 0.2;

eta = 1; % round trip eff

soc0 = 0.5; % initial SOC


%% Network parameters
% from bus, to bus, R/l, X/l, l (Length)
% R and X in ohm/km

linedata_L = [1 2 0.579 0.367 2.8;
             2 3 0.164 0.116 4.4;
             3 4 0.262 0.121 0.6;
             4 5 0.354 0.129 0.6;
             5 6 0.336 0.126 1.5;
             6 7 0.256 0.13 0.2;
             7 8 0.294 0.123 1.7;
             8 9 0.339 0.13 0.3;
             9 10 0.399 0.133 0.8;
             10 11 0.367 0.133 0.3;
             11 4 0.423 0.134 0.5;
             3 8 0.172 0.115 1.3;
             12 13 0.337 0.358 3;
             1 12 0.337 0.358 4.9];

% transformer data
% 480 V on LV side is 12.47 kV on MV side

% delta-Y type
% [from bus, to bus, X[pu], V[from], V[to], Srated[kVA]]
```

```

Xfr = [14 1 (0.05*basekVA/5000) 0.48 12.47 5000];

% base taken from Xrf data sheet
baseZ = (12.47^2)/(basekVA/1000) ;

line_data = [linedata_L(:,1:2),linedata_L(:,3).*linedata_L(:,5)./baseZ,linedata_L(:,4).*linedata_L(:,5)./baseZ];
line_data(end+1,:) = [Xfr(1) Xfr(2) 0 Xfr(3)];

%% Load
% normalized profile (%)
household=[0.217;0.193;0.192;0.189;0.244;0.401;0.611;0.646;0.635;0.679;0.611;0.736;
        0.661;0.57;0.496;0.465;0.653;0.792;0.925;0.821;0.679;0.569;0.404;0.27]';
industrial=[0.32;0.287;0.323;0.363;0.473;0.665;0.886;0.994;0.985;
0.992;0.801;0.825;0.859;0.856;0.864;0.816;0.553;0.498;0.461;0.416;
0.394;0.363;0.351;0.34]';

Phousehold = repmat(household,14,1);
Pindustrial = repmat(industrial,14,1);

%Load Base
PLmax = 3000; % kVA

% load max values [pu]
% [node, type, Pmax, Qmax]
% type: 1(household), 2(industrial)

loadmax = [1 1 0.15 0.03;
           1 2 0.05 0.01;
           2 1 0.00276 0.00069;
           3 2 0.00224 0.00139;
           4 1 0.00432 0.00108;
           5 1 0.00725 0.00182;
           6 1 0.0055 0.00138;
           7 2 0.00077 0.00048;
           8 1 0.00588 0.00147;
           9 2 0.00574 0.00356;
           10 1 0.00477 0.0012;
           11 1 0.00331 0.00083;
           12 1 0.15 0.03;
           13 2 0.05 0.0002];


% separating household and industrial load profiles

location_HH = [1 1 0 1 1 1 0 1 0 1 1 1 0 0]' ; % 1 for HH, 0 for IND at respective bus
loadmax_HH = [loadmax(1,3:4);loadmax(3:end,3:4);[0 0]].*location_HH; % max pu values
location_IND = [1; (-location_HH(2:13,1) + ones(12,1));0]; % bus location of industrial load
loadmax_IND = [loadmax(2,3:4);loadmax(3:end,3:4);[0 0]].*location_IND; % max pu value
```

```
load_HH = zeros(14,2,24);
load_IND = zeros(14,2,24);

% Load(pu) = max_load(pu)*24h_profile(normalized)*load_base(kVA)/basekVA

load_HH(:,1,:)= loadmax_HH(:,1).*Phousehold.*PLmax./basekVA;
load_HH(:,2,:)= loadmax_HH(:,2).*Phousehold.*PLmax./basekVA;
load_IND(:,1,:)= loadmax_IND(:,1).*Pindustrial.*PLmax./basekVA;
load_IND(:,2,:)= loadmax_IND(:,2).*Pindustrial.*PLmax./basekVA;

TotalLoad = (load_HH + load_IND).*LoadFactor;
% 14*2*24 size
% 14 buses, 2 for P&Q , 24 hr

% bus_data = [bus_no, type, V, d]
% PV bus is type 2, PQ bus is type 1
% HCPQ bus is type 4


bus_data = [1 1 1 0;
            2 1 1 0;
            3 4 1 0;
            4 4 1 0;
            5 4 1 0;
            6 4 1 0;
            7 4 1 0;
            8 4 1 0;
            9 4 1 0;
            10 4 1 0;
            11 4 1 0;
            12 1 1 0;
            13 1 1 0;
            14 2 1 0];

type = bus_data(:,2);
n_bus = length(type);

% initial V and d
V = bus_data(:,3);
d = bus_data(:,4); %radians


wref = 2*pi*50;
Vref = 12.47; % kV
d0 = 0;


% secondary integral constants
```

```
ki_w = 4;

uv_int = zeros(length(3:11),1);
% secondary integral voltage parameter
%initial value  for HCPQ buses


% idx_DG = find(type==2); %index of PV busess
% idx_HCPQ = 3:11; % busses to be controlled
% n_DG = sum(bus_data(:,2)==2); %number of PQ buses
% n_PQ = sum(bus_data(:,2)==1); %number of PV buses

%% Ybus calculation
[ybus, theta, ~ , ~] = ybuscalc(line_data);
```

F.2 Y-Bus

```
function [ybus, theta,Ibus,Vbus]= ybuscalc(line_data)

%line_data = [from_bus, to_bus, R, X];

from_bus = line_data(:,1);
to_bus = line_data(:,2);

no_of_bus = max(max(from_bus),max(to_bus));

% z = r +jx
z = line_data(:,3) + 1i.*line_data(:,4);
y = 1./z;

ybus = zeros(no_of_bus);
y_temp = zeros(no_of_bus);
Ibus = zeros(no_of_bus,1);
Vbus = zeros(no_of_bus,1);

for i=1:length(from_bus)
    if (from_bus(i) == 0) %diagonal
        y_temp(to_bus(i),to_bus(i)) = y(i);

         if size(line_data,2)==5
                %if that column is there in the data
            Ibus(to_bus(i)) = line_data(i,end)*y(i);
                % current in line, for bus connected to '0' bus
         end

    elseif (to_bus(i) == 0) %diagonal
        y_temp(from_bus(i),from_bus(i)) = y(i);
        if size(line_data,2)==5
            Ibus(from_bus(i)) = line_data(i,end)*y(i);
```

```
        end

    else
        y_temp(from_bus(i),to_bus(i)) = y(i);  %off-diagonal
        y_temp(to_bus(i),from_bus(i)) = y_temp(from_bus(i),to_bus(i)); %symmetrtical bus,
    end
end

for i=1:no_of_bus
    for j = 1:no_of_bus
        if i==j
            ybus(i,j) = sum(y_temp(i,:));
        else
            ybus(i,j) = -y_temp(i,j);
        end
    end
end

% separating magnitude and angle
theta = angle(ybus);
ybus = abs(ybus);

end
```

F.3 Main Function

```
clc
clear
CIGRE_benchmark_Microgrid; % data


% droop constants
% buses 3-11
% last one is for 150 kW WT on bus 7
kp = (1.25e-5)*ones(10,1);
kq = (1e-4)*ones(10,1);

del_soc = zeros(g,1); % change in SOC

% bus 13: 300 P&Q
% bus 14:1400 P
% bus 9: 300 P&Q
genDG = repmat([gen(:,1);gen(1,2);gen(3,2)],[g,1]);

Vpv = ones(g,1); % PV bus soft limits
Vres = ones(1,9*g); % HCPQ bus soft limits

x_opt = [kp;kq;del_soc;Vpv;Vres';genDG.*0.1];

```

```
lb=[1e-5/50*ones(1,10),1e-4/50*ones(1,10), Pbess_min*eta/E*ones(1,g),Vpv'*0.99,Vres.*0.99,zeros(1,5*g)];

ub=[1e-5*50*ones(1,10),1e-4*50*ones(1,10), Pbess_max*eta/E*ones(1,g),Vpv'*1.01,Vres.*1.01,genDG'];

start = tic;

options = optimoptions('fmincon','Display', 'iter-detailed','MaxFunctionEvaluations',40000, 'TolX',
    1e-6,'algorithm','sqp');

[x_opt, cost, exitflag] = fmincon(@obj_func_no_DR,x_opt,[],[],[],[],lb,ub,@limits, options);

time_sec = toc(start);
time_min = time_sec/60;
time_hr = time_sec/60/60;
```

F.4 Objective Function

```
function output = obj_func_no_DR(x_opt)

CIGRE_benchmark_Microgrid; % data

Pg = zeros(n_bus,g);
Qg = zeros(n_bus,g);

% Newton-Raphson
tol = 1e-6;
epsilon = 1e-4;

for hour = 1:g

% hourly voltages of PV and HCPQ buses
v14=x_opt(20+g+hour);
V3 = x_opt(20+2*g + hour);
V4 = x_opt(20+3*g + hour);
V5 = x_opt(20+4*g + hour);
V6 = x_opt(20+5*g + hour);
V7 = x_opt(20+6*g + hour);
V8 = x_opt(20+7*g + hour);
V9 = x_opt(20+8*g + hour);
V10 = x_opt(20+9*g + hour);
V11 = x_opt(20+10*g + hour);
Vres = [V3 V4 V5 V6 V7 V8 V9 V10 V11]';

    if PPV(hour) ==0
         x_nr = [d; V(1:6); uv_int(5); V(8:13)]; % solar buses ar PQ
         x_nr = nrpffunc(x_nr, tol,epsilon,x_opt,hour); % for one load value

         Vnr(:,hour) = [x_nr(15:20); Vres(5); x_nr(22:27);v14];
         uv_intnr(:,hour) = [zeros(4,1); x_nr(21); zeros(4,1)]; % 3-6, 7, 8-11
```

```

    else
        x_nr = [d; V(1:2); uv_int; V(12:13)];
        x_nr = nrpffunc(x_nr, tol,epsilon,x_opt,hour); % for one load value

        Vnr(:,hour) = [x_nr(15 :16); Vres; x_nr(26:27);v14];
        uv_intnr(:,hour) = x_nr(17: 25);
    end

    dnr(:,hour) = x_nr(1:14);

% Net power at a bus
[Pnr(:,hour), Qnr(1:13,hour)] = PQ_calc_HC(ybus, theta, n_bus,Vnr(:,hour),dnr(:,hour));

for i=14 % PV bus
    q=0;
    for j = 1:n_bus
        q = q - abs(Vnr(i,hour)*(ybus(i,j)*Vnr(j,hour)))*sin(theta(i,j) + dnr(j,hour) - dnr(i,hour));
    end
    Qnr(i,hour) = q;
end

%droop constants
kp = x_opt(1:10);
kq = x_opt(11:20);


if PPV(hour) ==0
    i = 7;
    Pg(i,hour) = (-ki_w*(dnr(1,hour)-d0)/basekVA)/kp(i-2);
    Qg(i,hour) = (Vres(5) - Vnr(i,hour) + uv_intnr(i-2,hour))*Vref/kq(i-2)/basekVA;
else
    for i = 3:11
        Pg(i,hour) = (-ki_w*(dnr(1,hour)-d0)/basekVA)/kp(i-2);
        Qg(i,hour) = (Vres(i-2) - Vnr(i,hour) + uv_intnr(i-2,hour))*Vref/kq(i-2)/basekVA;
    end
end

    % uv_int(1) is a parameter for bus 3

    % 3 other WTs on bus 7
    Pg7_1000(hour) = Pg(7,hour);
    Pg7_150(hour) = (-ki_w*(dnr(1,hour)-d0)/basekVA)/kp(10);
    Pg(7,hour) = Pg7_1000(hour) + 3*Pg7_150(hour);
    Qg(7,hour) = Qg(7,hour) + 3*(Vres(5) - Vnr(7,hour) + uv_intnr(5,hour))*Vref/kq(10)/basekVA;



    % P and Q for CGs
```

```
    % CG order: P300(13), P1400(14), P300(9), Q300(13), Q300(9)

     temp=x_opt(end+1-(5*g):end);
    % every 5th corresponds to the same CG

    Pg(13,hour) = temp(5*hour - 4);
    Pg(14,hour)= temp(5*hour - 3);
    Pg9_300(hour,1) = temp(5*hour-2);

    Qg(13,hour) = temp(5*hour-1);
    Qg9_300(hour,1) = temp(5*hour);

    Pg(9,hour) = Pg(9,hour) + Pg9_300(hour);
    Qg(9,hour) = Qg(9,hour) + Qg9_300(hour);

    % BESS
    P_bess(1,hour) = E/eta*x_opt(20 + hour);

end

%% SOC calculate
soc(1) = x_opt(20 + 1) + soc0;
if g >1
    for hour = 2:g
        soc(hour)  = x_opt(20 + hour) + soc(hour-1);
    end
end

%% BESS
Pg(5,:) = Pg(5,:) + P_bess;

%% Hourly Balance
hourlyCG = [(sum(Pg(13:14,:),1)'+ (Pg9_300(:))), (sum(Qg(13,:),1)' + (Qnr(14,:)') + (Qg9_300(:)))].*basekVA;
hourlyRES = [(sum(Pg(3:11,:),1)' - (Pg9_300(:))), (sum(Qg(3:11,:),1)'- (Qg9_300(:)))].*basekVA;
hourlyLOAD = [squeeze(sum(TotalLoad(:,1,1:g),1)), squeeze(sum(TotalLoad(:,2,1:g),1))].*basekVA;
hourlyLOSS = [(sum(Pnr,1)'), (sum(Qnr,1)')].*basekVA ;

%% Calculate objective (cost) function

% Cost
% Pdg is CG power output: 5*24
% Bus 13(300 W), 14(1400 W), 9(300 W)

Pdg = [Pg(13,:); Pg(14,:); Pg9_300'].*basekVA;

% Pres is RES curtailed power: 9*24
% Bus 3,4,5(without BESS),6,7(4 WTs),8,9,10,11

% curtailed = available - used
```

```
Pres = -basekVA.*  [Pg(3,:)-squeeze(Generation(3,1,1:g))';
                    Pg(4,:)-squeeze(Generation(4,1,1:g))';
                    (Pg(5,:)-P_bess)-squeeze(Generation(5,1,1:g))';
                    Pg(6,:)-squeeze(Generation(6,1,1:g))';
                    Pg(7,:)-squeeze(Generation(7,1,1:g))';
                    Pg(8,:)-squeeze(Generation(8,1,1:g))';
                    (Pg(9,:)- Pg9_300')-squeeze(Generation(9,1,1:g))';
                    Pg(10,:)-squeeze(Generation(10,1,1:g))';
                    Pg(11,:)-squeeze(Generation(11,1,1:g))' ];


Cost = costfunc(Pdg,Pres,g);


%% Total System Parameters

DG_GEN = [(sum(Pg(13:14,:),'all')' + sum(Pg9_300(:))),
     (sum(Qg(13,:),'all')'+sum(Qnr(14,:),'all')+sum(Qg9_300(:)))].*basekVA; % CG generation
DG_RES = [(sum(Pg(3:11,:),'all')'-sum(Pg9_300(:))), (sum(Qg(3:11,:),'all')'-sum(Qg9_300(:)))].*basekVA;
DG = DG_GEN + DG_RES; % RES generation (including BESS)
Demand = [sum(TotalLoad(:,1,1:g),'all'), sum(TotalLoad(:,2,1:g),'all')].*basekVA;

Loss = [(sum(Pnr,'all')'), (sum(Qnr,'all')')].*basekVA ;

output = Cost;
end
```

F.5 Generalized Numerical Newton-Raphson

```
function x = nrpffunc(x, tol,epsilon,x_opt,hour)
    J = zeros(length(x)); %Jacobian
    itr = 0;

    df = [11 1]; %large initial value to go into the loop
    % df is power mis-match vector

    while ((sum(abs(df))>tol))
    df = power_HC(x,x_opt,hour); % objective function for NR
        for i=1:length(x) %column of J
            x0 = zeros(length(x),1);

            for j = 1:length(x)
                        % which x to differentiate with respect to
                if i==j
                    x0(j,1) = x(j,1) + epsilon;
                        %partial differentiation element for column i
                else
                    x0(j,1) = x(j,1);
```

```
                end
            end

            df0 = power_HC(x0,x_opt,hour);
                % df with effect of epsilon

            J(:,i) = (df0-df)/epsilon;
                % df_with_epsilon - df_without_epsilon
        end

        x_prev = x;

        %update
        x = x_prev - J\df;
        itr = itr +1 ;
        df =  power_HC(x,x_opt,hour);

    end
end
```

F.6 Power Mis-Match Vector Calculation

```
function df = power_HC(x_nr,x_opt,hour)

     CIGRE_benchmark_Microgrid; % data

     % voltage for respective buses for particular hour
        v14=x_opt(20+g+hour);
V3 = x_opt(20+2*g + hour);
V4 = x_opt(20+3*g + hour);
V5 = x_opt(20+4*g + hour);
V6 = x_opt(20+5*g + hour);
V7 = x_opt(20+6*g + hour);
V8 = x_opt(20+7*g + hour);
V9 = x_opt(20+8*g + hour);
V10 = x_opt(20+9*g + hour);
V11 = x_opt(20+10*g + hour);

    Vres = [V3 V4 V5 V6 V7 V8 V9 V10 V11]';

    d = x_nr(1:14); % bus angle


    if PPV(hour) ==0 %night
         % solar buses are PQ
        V = [x_nr(15 :20); Vres(5); x_nr(22:27);v14];
        uv_int = x_nr(21);
    else
        V = [x_nr(15 :16); Vres; x_nr(26:27);v14];
```

```
        uv_int = x_nr(17: 25);
    end

        %droop coefficients
     kp = x_opt(1:10);
     kq = x_opt(11:20);


        %calculated powers
    [P_calc, Q_calc] = PQ_calc_HC(ybus, theta, n_bus,V,d);
    F_calc = [P_calc; Q_calc];


    % bus 1,2,12,13 are PQ buses
    Pg = zeros(n_bus,1);
    Qg = zeros(n_bus-1,1);

    % bus 3-11 are HCPQ buses
    % bus 14 is PV bus

    % HCPQ buses
    if PPV(hour) == 0 % solar buses at night
        i = 7; % WT 1000 kW
        Pg(i) = (-ki_w*(d(1)-d0)/basekVA)./kp(i-2);
        Qg(i) = (Vres(i-2) - V(i) + uv_int).*Vref./kq(i-2)./basekVA;

    % 3 other WTs on bus 7
    Pg(7) = Pg(7) + 3*(-ki_w*(d(1)-d0)/basekVA)/kp(10);
    Qg(7) = Qg(7) + 3*(Vres(i-2) - V(7) + uv_int).*Vref./kq(10)./basekVA;
    else % solar buses during day
        for i = 3:11
            Pg(i) = (-ki_w*(d(1)-d0)/basekVA)./kp(i-2);
            Qg(i) = (Vres(i-2) - V(i) + uv_int(i-2)).*Vref./kq(i-2)./basekVA;
        end
            % 3 other WTs on bus 7
    Pg(7) = Pg(7) + 3*(-ki_w*(d(1)-d0)/basekVA)/kp(10);
    Qg(7) = Qg(7) + 3*(Vres(5) - V(7) + uv_int(5)).*Vref./kq(10)./basekVA;
    end


    % BESS on bus 5
    P_bess = E/eta*x_opt(20 + hour);
    Pg(5) = Pg(5) + P_bess;


    % P and Q for CGs
    % CG order: P300(13), P1400(14), P300(9), Q300(13), Q300(9)

     temp=x_opt(end+1-(5*g):end);
```

```
    % every 5th corresponds to the same CG

    Pg(13) = temp(5*hour - 4);
    Pg(14)= temp(5*hour - 3);
    Pg9_300 = temp(5*hour-2);

    Qg(13) = temp(5*hour-1);
    Qg9_300 = temp(5*hour);

    Pg(9) = Pg(9) + Pg9_300;
    Qg(9) = Qg(9) + Qg9_300;


    % Load
    Pd = TotalLoad(:,1,hour);
    Qd = TotalLoad(1:13,2,hour);

    % Scheduled or reference powers
    Pref = Pg - Pd; % 14 rows
    Qref = Qg - Qd; % 13 rows [bus 14 is PV so not included]
    % ref = gen - load

    F_ref = [Pref; Qref];

    % power mis-match matrix
    df =  F_ref - F_calc;
end
```

F.7 Calculated Power

```
function [Pcalc, Qcalc] = PQ_calc_HC(ybus, theta, n_bus,V,d)

% PQ: 1,2,12,13
% HCPQ: 3-11
% PV: 14

% P_calc
for i=1:n_bus
    p =0;
    for j = 1:n_bus
        p = p + abs(V(i)*ybus(i,j)*V(j))*cos(theta(i,j) + d(j) - d(i));
    end
    Pcalc(i,1) = p;
end

% Q_calc
% PV buses not included
for i=1:(n_bus-1)
    q=0;
```

```
    for j = 1:n_bus
        q = q - abs(V(i)*(ybus(i,j)*V(j)))*sin(theta(i,j) + d(j) - d(i));
    end
    Qcalc(i,1) = q;
end

end
```

F.8 Cost Equation

```
function cost = costfunc(Pdg,Pres,g)


% Pdg is CG active power output: 5*24
% Pres is RES curtailed (unused) power: 10*24

% CG cost coefficients [Capacity, a, b, c]

cost_coeff = [300 0.0061 0.091 0.184;
              1400 0 0.2571 25.5;
              300 0.0061 0.091 0.184;];



a = cost_coeff(:,2);
b = cost_coeff(:,3);
c = cost_coeff(:,4);

a = repmat(a, 1, g);
b = repmat(b, 1, g);
c = repmat(c, 1, g);


% Cost from CG
CG = sum(a.*(Pdg.^2) + (b.*Pdg) + c, 'all');


% RES penalty factor
C_res = 10;

% Cost from RES
RES = sum(C_res.*Pres,'all');

% Total cost
cost = (CG + RES);

end
```

F.9 Non-Linear Constraint

```
function [c, ceq] = limits(x_opt)

CIGRE_benchmark_Microgrid; % data

ceq = []; % equality: ceq = 0; not used
c = []; % inequality: c<=0

P_min =[];
P_max =[];
Q_min =[];
Q_max =[];


Pg = zeros(n_bus,g);
Qg = zeros(n_bus,g);

% NR
tol = 1e-6;
epsilon = 1e-4;
for hour = 1:g
v14=x_opt(20+g+hour);

V3 = x_opt(20+2*g + hour);
V4 = x_opt(20+3*g + hour);
V5 = x_opt(20+4*g + hour);
V6 = x_opt(20+5*g + hour);
V7 = x_opt(20+6*g + hour);
V8 = x_opt(20+7*g + hour);
V9 = x_opt(20+8*g + hour);
V10 = x_opt(20+9*g + hour);
V11 = x_opt(20+10*g + hour);
Vres = [V3 V4 V5 V6 V7 V8 V9 V10 V11]';
    if PPV(hour) ==0
         x_nr = [d; V(1:6); uv_int(5); V(8:13)]; % solar buses ar PQ
         x_nr = nrpffunc(x_nr, tol,epsilon,x_opt,hour); % for one load value

         Vnr(:,hour) = [x_nr(15:20); Vres(5); x_nr(22:27);v14];
         uv_intnr(:,hour) = [zeros(4,1); x_nr(21); zeros(4,1)]; % 3-6, 7, 8-11

    else
        x_nr = [d; V(1:2); uv_int; V(12:13)];
        x_nr = nrpffunc(x_nr, tol,epsilon,x_opt,hour); % for one load value

        Vnr(:,hour) = [x_nr(15 :16); Vres; x_nr(26:27);v14];
        uv_intnr(:,hour) = x_nr(17: 25);
    end

```

```
    dnr(:,hour) = x_nr(1:14);

    kp = x_opt(1:10);
    kq = x_opt(11:20);

    if PPV(hour) ==0
        i = 7;
        Pg(i,hour) = (-ki_w*(dnr(1,hour)-d0)/basekVA)/kp(i-2);
        Qg(i,hour) = (Vres(5) - Vnr(i,hour) + uv_intnr(i-2,hour))*Vref/kq(i-2)/basekVA;
    else
        for i = 3:11
            Pg(i,hour) = (-ki_w*(dnr(1,hour)-d0)/basekVA)/kp(i-2);
            Qg(i,hour) = (Vres(i-2) - Vnr(i,hour) + uv_intnr(i-2,hour))*Vref/kq(i-2)/basekVA;
        end
    end

    P7_1000(hour) = Pg(7,hour);
    P7_150(hour) = (-ki_w*(dnr(1,hour)-d0)/basekVA)/kp(10);
    Pg(7,hour) = P7_1000(hour) + 3*P7_150(hour);
    Qg(7,hour) = Qg(7,hour) + 3*(Vres(5) - Vnr(7,hour) + uv_intnr(5,hour))*Vref/kq(10)/basekVA;

% RES max and min
    P_max = [P_max; (Pg(3:11,hour)-Generation(3:11,1,hour))];
    Q_max = [Q_max; (Qg(3:11,hour)-Generation(3:11,2,hour))];
    P_min = [P_min; (zeros(9,1) - Pg(3:11,hour))];
    Q_min = [Q_min; (zeros(9,1) - Qg(3:11,hour))];



    for i=14 % PV bus
    q=0;
    for j = 1:n_bus
        q = q - abs(Vnr(i,hour)*(ybus(i,j)*Vnr(j,hour)))*sin(theta(i,j) + dnr(j,hour) - dnr(i,hour));
    end
    Qnr(i-13,hour) = q;
    end

%PV bus
   Q_max = [Q_max; (Qnr(:,hour)-sum(gen(2,2)))];
   Q_min = [Q_min; (zeros(1,1) - Qnr(:,hour))];




end

%% SOC calculation

soc(1) = x_opt(20 + 1) + soc0;
```

```
if g >1
    for hour = 2:g
        soc(hour)  = x_opt(20 + hour) + soc(hour-1);
    end
end

%%


c  = [P_max; P_min; Q_max; Q_min; (soc' - soc_max.*ones(g,1)); (soc_min.*ones(g,1) - soc')];


end
```

Bibliography

[1] European Commission. *Horizon 2020*. English. Luxembourg: Publications Office, 2020. ISBN: 9276215190. URL: https://op.europa.eu/publication/manifestation_identifier/PUB_KI0420469ENN.

[2] "European Green Deal Call: EU 1 billion investment to boost the green and digital transition". English. In: *European Union News* (2020).

[3] Energinet Electricity System Operator. *SYSTEM PERSPECTIVES OF THE 70 % TARGET AND LARGE SCALE OFFSHORE WIND: Executive Summary and Main Conclusions*. English. Tech. rep. Energinet, 2020, pp. 189–200.

[4] Daniel E. Olivares et al. "Trends in Microgrid Control". In: *IEEE transactions on smart grid* 5.4 (2014), pp. 1905–1919.

[5] Peter D Lund et al. "Review of energy system flexibility measures to enable high levels of variable renewable electricity". In: *Renewable and Sustainable Energy Reviews* 45 (2015), pp. 785–807.

[6] Lexuan Meng et al. "Microgrid supervisory controllers and energy management systems: A literature review". In: *Renewable & sustainable energy reviews* 60 (2016), pp. 1263–1273.

[7] Omid Palizban, Kimmo Kauhaniemi, and Josep M. Guerrero. "Microgrids in active network management—Part I: Hierarchical control, energy storage, virtual power plants, and market participation". In: *Renewable & sustainable energy reviews* 36 (2014), pp. 428–439.

[8] Luka Strezoskiand Izabela Stefani and Branislav Brbaklic. "Active Management of Distribution Systems with High Penetration of Distributed Energy Resources". In: *IEEE EUROCON 2019 - 18th International Conference on Smart Technologies* (2019).

[9] Richard J. Bravo et al. "Distributed Energy Resources Challenges for Utilities". In: *2015 IEEE 42nd Photovoltaic Specialist Conference (PVSC)* (14-19 June 2015).

[10] James T. Reilly. "From microgrids to aggregators of distributed energy resources. The microgrid controller and distributed energy management systems". In: *The Electricity Journal* (June 2019).

[11] B. Davito, H. Tai, and R. Uhlaner. "The smart grid and the promise of demand-side management". In: (2010).

[12] P. Palensky and D. Dietrich. "Demand Side Management: Demand Response, Intelligent Energy Systems, and Smart Loads". In: *IEEE Transactions on Industrial Informatics* 7.3 (2011), pp. 381–388. DOI: 10.1109/TII.2011.2158841.

[13] Greyard Tembo. "Overview of the Microgrid Concept and its Hierarchical Control Architecture". In: *International Journal of Engineering Research & Technology* 5.3 (March 2016).

[14] Dinesh Pattabiraman, R. H. Lasseter, and T. M. Jahns. "Comparison of Grid Following and Grid Forming Control for a High Inverter Penetration Power System". In: *IEEE Power & Energy Society General Meeting* (2018).

[15] J. Rocabert et al. "Control of Power Converters in AC Microgrids". In: *IEEE Transactions on Power Electronics* 27.11 (2012), pp. 4734–4749.

[16] J.M. Guerrero et al. "A wireless controller to enhance dynamic performance of parallel inverters in distributed generation systems". In: *IEEE Transactions on Power Electronics* 19.5 (2004), pp. 1205–1213.

[17] J. M. Guerrero et al. "Hierarchical control of droop-controlled ac and dc Microgrids: A general approach toward standardization". In: *IEEE Transactions on Industrial Electronics* 58.1 (2011), pp. 158–172.

[18] Hossein Shayeghi et al. "A survey on microgrid energy management considering flexible energy sources". In: *Energies* 12.11 (2019), p. 2156.

[19] Aftab Ahmad Khan et al. "A compendium of optimization objectives, constraints, tools and algorithms for energy management in microgrids". In: *Renewable & sustainable energy reviews* 58 (2016), pp. 1664–1683.

[20] Hadi Saadat. *Power System Analysis*. 3rd. PSA-Publishing, 2010.

[21] William D. Stevenson Jr. *Elements of Power System analysis*. 4th. McGraw-Hill, 2015.

[22] Chendan Li et al. "Power Flow Analysis for Low-Voltage AC and DC Microgrids Considering Droop Control and Virtual Impedance". In: *IEEE transactions on Smart Grid* 8.6 (2017), pp. 2754–2764. URL: https://ieeexplore.ieee.org/document/7442160.

[23] Morad M. A. Abdelaziz et al. "A Novel and Generalized Three-Phase Power Flow Algorithm for Islanded Microgrids Using a Newton Trust Region Method". In: *IEEE Transactions on Power Systems* 28.1 (2013), pp. 190–201. URL: https://ieeexplore.ieee.org/document/6203626.

[24] Gibran D. A. Tinajero. "Modeling, Analysis and Control of AC Microgrids in Steady-State". English. PhD thesis. 2015.

[25] Chendan Li et al. "Power flow analysis algorithm for islanded LV microgrids including distributed generator units with droop control and virtual impedance loop". In: IEEE, Mar 2014. URL: `https://ieeexplore.ieee.org/document/6803760`.

[26] FN Al Farsi et al. "Economic dispatch in power systems". In: *2015 IEEE 8th GCC Conference & Exhibition*. IEEE. 2015, pp. 1–6.

[27] Alireza Soroudi. *Power system optimization modeling in GAMS*. Vol. 78. Springer, 2017.

[28] Stephen Frank, Ingrida Steponavice, and Steffen Rebennack. "Optimal power flow: a bibliographic survey I". In: *Energy Systems* 3.3 (2012), pp. 221–258.

[29] Tine L Vandoorn et al. "Microgrids: Hierarchical control and an overview of the control and reserve management strategies". In: *IEEE industrial electronics magazine* 7.4 (2013), pp. 42–55.

[30] S. Chowdhury, S.P. Chowdhury, and P. Crossley. "Microgrids and active distribution networks (IRE Series)". In: *The Institution of Engineering and Technology* (2009).

[31] Eleonora Riva Sanseverino et al. "Optimal power flow in three-phase islanded microgrids with inverter interfaced units". In: *Electric Power Systems Research* 123 (2015), pp. 48–56.

[32] Gibran Agundis-Tinajero et al. "Extended-optimal-power-flow-based hierarchical control for islanded AC microgrids". In: *IEEE Transactions on Power Electronics* 34.1 (2018), pp. 840–848.

[33] J. M. Guerrero et al. "Control Strategy for Flexible Microgrid Based on Parallel Line-Interactive UPS Systems". In: *IEEE Transactions on Industrial Electronics* 56.3 (2009), pp. 726–736. DOI: `10.1109/TIE.2008.2009274`.

[34] J. Wang et al. "Active and reactive power support of MV distribution systems using battery energy storage". In: *2017 IEEE International Conference on Industrial Technology (ICIT)*. 2017, pp. 382–387.

[35] Daniel E. Olivares, Claudio A. Canizares, and Mehrdad Kazerani. "A Centralized Energy Management System for Isolated Microgrids". In: *IEEE transactions on smart grid* 5.4 (2014), pp. 1864–1875.

[36] K. Rudion et al. "Design of benchmark of medium voltage distribution network for investigation of DG integration". In: *2006 IEEE Power Engineering Society General Meeting*. 2006.

[37] Najmeh Bazmohammadi et al. "A hierarchical energy management strategy for interconnected microgrids considering uncertainty". In: *International Journal of Electrical Power & Energy Systems* 109 (2019), pp. 597–608.

[38] IEC Standard Voltages. "IEC 60038". In: *Edition* 7 (2002), pp. 2009–06.

[39] H. Markiewicz and A. Klajn. "Voltage Disturbances Standard EN 50160 - Voltage Characteristics in Public Distribution Systems". In: Copper Development Association, 2008.

[40] Sherif M Ismael et al. "State-of-the-art of hosting capacity in modern power systems with distributed generation". In: *Renewable energy* 130 (2019), pp. 1002–1020.

[41] Ahmet Mete Vural. "Interior point-based slack-bus free-power flow solution for balanced islanded microgrids". In: *International Transactions on Electrical Energy Systems* 26.5 (2016), pp. 968–992.

[42] Najmeh Bazmohammadi et al. "An Efficient Decision-Making Approach for Optimal Energy Management of Microgrids". In: *2019 IEEE Milan PowerTech*. 2019, pp. 1–6. DOI: 10.1109/PTC.2019.8810667.